

**DESIGN AND ANALYSIS OF ANTENNA-ON-
CHIP AND ANTENNA-IN-PACKAGE FOR 60-GHZ
WIRELESS COMMUNICATIONS**

BAO XIAOYUE

(B. ENG., HARBIN INSTITUTE OF TECHNOLOGY)

**A THESIS SUBMITTED FOR THE DEGREE OF
DOCTOR OF PHILOSOPHY**

NATIONAL UNIVERSITY OF SINGAPORE

2013

DECLARATION

I hereby declare that the thesis only contains my original research work which has been written all by me in the entirety. Where other sources of information have been used, they have been acknowledged.

This thesis has also not been submitted for any degree in any other university previously.

BAO XIAOYUE

JULY 2013

ACKNOWLEDGEMENT

First and foremost, I would like to express my deepest gratitude to my supervisor, Assoc. Prof. Guo Yong-Xin for his in-depth guidance, constant supports and kindness during the four years period of my Ph.D study. Without his advice and encouragement, this work would never be possible.

I would also like to express my sincerest gratitude to other faculty staffs in the NUS Microwave and RF group: Prof. Yeo Tat-Soon, Prof. Yeo Swee-Ping, Assoc. Prof. Chen Xu-Dong, Dr Qiu Cheng-Wei, and Dr Hui Hon-Tat for their attention and advice on my research. Dr Xiong Yong-Zhong, Dr Hu San-Ming, and Dr Jin Cheng, my former and current collaborators in Institute of Microelectronics (IME), provided me with the opportunity to work on the CMOS on-chip antenna designs. I deeply appreciate their scientific support and collaboration throughout my research. In addition, I owe a huge debt of gratitude to my current collaborator, Assoc. Prof. Cheng Yu-Jian in the University of Electronic Science and Technology of China (UESTC), for his wise suggestions, valuable guidance and inspiration.

Special thanks should go to my friends in NUS: Mr Liu Chang-Rong, Mr Long Yun-Shen, Mr Sun Hu-Cheng, Mr Wan Chao, Miss Ren Rui, Miss

Wang Jin, Miss Xu Li-Jie, Dr Duan Zhu, Dr Ge Jing-Yan, Dr Liu Hui-Zhe, Dr Pan Li, Dr Wang Lei, Dr Wu Yu-Ming, Dr Ye Xiu-Zhu, and Dr Zhong Zheng, who shared with me a fruitful life in NUS for the past four years. I would also like to thank the supporting staffs in NUS Microwave group: Mr Sing Cheng-Hiong, Madam Guo Lin and Madam Lee Siew-Choo for their professional technical supports in antenna measurements.

Importantly, I would like to thank my beloved parents for their love and great support all through these years. Thank goes to my father Bao Xing-Zhong, who sparked my initial interest in this fantastic world of engineering research. Thanks go to my mother Yao Zhong-Yi for her timely comfort as my most loyal friend. Your selfless love and caring support got me through the hardest times and fulfilled my life.

LIST OF PUBLICATIONS

Journal Papers

1. X.Y. Bao, Y.X. Guo, Y.Z. Xiong, 60-GHz AMC-Based Circularly Polarized On-Chip Antenna Using Standard 0.18- μm CMOS Technology, *IEEE Transactions on Antennas and Propagation*, vol. 60, no.5, pp. 2234-2241, May 2012;
2. Y.J. Cheng, X.Y. Bao, Y.X. Guo, LTCC-Based Substrate Integrated Image Guide and Its Transition to Coplanar Waveguide, accepted by *IEEE Microwave and Wireless Components Letters*, vol. 23, no.9, pp 450-452, Sept 2013;
3. X.Y. Bao, Y.X. Guo, Two 60-GHz LTCC Circularly Polarized T-Probe fed Antenna Arrays with a modified Soft-surface Structure, to be submitted to *IEEE Transactions on Antennas and Propagation*;
4. Y.J. Cheng, X.Y. Bao, Y.X. Guo, 60-GHz LTCC Miniaturized Substrate Integrated Multibeam Array Antenna with Multiple Polarizations, accepted by *IEEE Transactions on Antennas and Propagation*, early access;
5. C.R. Liu, Y.X. Guo, X.Y. Bao, S.Q. Xiao, 60-GHz LTCC Integrated Circularly Polarized Helical Antenna Array, *IEEE Transactions on Antennas and Propagation*, vol. 60, no.3, pp. 1329-1335, Mar 2012;

6. Y.J. Cheng, Y.X. Guo, X.Y. Bao, Millimeter-Wave LTCC Periodic Leaky Wave Antenna Based on substrate integrated image waveguide Technology, accepted by *IEEE Transactions on Antennas and Propagation*;

Conference Papers

7. X.Y. Bao, Y.X. Guo, A 60-GHz AMC-Based Circularly Polarized On-Chip Antenna using 0.18 μm CMOS Technology, *IEEE International Symposium on Antenna and Propagation*, Spokane, Washington, USA, July 3-8, 2011;
8. X.Y. Bao, Y.X. Guo, S.M. Hu, A 60-GHz Differential On-Chip Yagi Antenna Using 0.18- μm CMOS Technology, *IEEE Asia-Pacific Conference on Antennas and Propagation*, Singapore, Aug 26-28, 2012.

CONTENTS

DECLARATION	i
ACKNOWLEDGEMENT	ii
LIST OF PUBLICATIONS	iv
CONTENTS	vi
SUMMARY	x
LIST OF TABLES	xii
LIST OF FIGURES.....	xiii
LIST OF ACRONYMS.....	xviii
Chapter 1: Introduction	1
1.1 Background of 60-GHz Wireless Communications	1
1.2 Antennas-on-Chip	5
1.2.1 Literature Review	5
1.2.2 State-of-the-Art on-Chip Antennas	7
1.2.3 Ways to Improve the Antennas-on-Chip.....	8

1.3	Antennas-in-Package	10
1.3.1	Literature Review	10
1.3.2	State-of-the-Art in-Package Antenna Arrays	12
1.4	Thesis Outline	14
1.5	Some Original Contributions	15
Chapter 2:	AMC-Based on-chip Antenna Design	17
2.1	Artificial Magnetic Conductor Structure	17
2.1.1	Literature Review	17
2.1.2	Employment of AMC in Antenna Designs	18
2.1.3	Some Classic AMC Structures	19
2.2	Analysis of a Novel AMC Structure	21
2.2.1	Unit Structure	21
2.2.2	Parameter Study	23
2.3	AMC-Based Circularly Polarized on-Chip Loop Antenna Using CMOS Technology	25
2.3.1	Circularly Polarized Loop Antenna Design	25
2.3.2	Integration of Modified AMC plane	29
2.3.3	Measurement and Analysis	31
2.4	Summary	39
Chapter 3:	Circularly Polarized Antennas-in-Package with Modified Soft-Surface Structure	40
3.1	Literature Review	40
3.2	Circularly Polarized T-probe Fed Antennas	41
3.2.1	Circularly Polarized T-probe Stubbed Patch Antenna	41
3.2.2	Circularly Polarized T-probe Slot Patch Antenna	46
3.3	Soft-Surface Structure	50
3.3.1	Literature Review	50
3.3.2	Structure of Modified Soft-Surface	51

3.3.3	Soft-Surface Structure around Antenna Element.....	52
3.3.4	Reduction of Mutual Coupling.....	55
3.4	Circularly Polarized T-probe Patch Antenna Arrays with Soft-Surface in LTCC.....	56
3.4.1	Antenna Array and Transition.....	56
3.4.2	Integration of Soft-Surface Structure.....	58
3.4.3	Measurement and Results.....	63
3.5	Circularly Polarized T-probe Slot Antenna Array with Soft-Surface in LTCC.....	68
3.5.1	Antenna Array with Soft-Surface Structure.....	68
3.5.2	Measurement and Results.....	68
3.6	Summary.....	72
Chapter 4:	Multibeam Antenna Arrays with Multiple Polarizations ...	73
4.1	Introduction.....	73
4.2	Folded Butler Matrix.....	76
4.2.1	Interconnection between Layers and Self Compensation	76
4.2.2	Design Procedure of Butler Matrix.....	78
4.3	Dual Linearly Polarized Substrate Integrated Multibeam Antenna Array.....	84
4.3.1	45° Linearly Polarized Antenna Element.....	84
4.3.2	Antenna Array.....	86
4.3.3	Measurement and Analysis.....	88
4.4	Dual Circularly Polarized Substrate Integrated Multibeam Antenna Array.....	93
4.4.1	Dual Circularly Polarized Antenna Array.....	93
4.4.2	Measurement and Analysis.....	95
4.5	Summary.....	98
Chapter 5:	Conclusions and Future Works.....	99

5.1	Conclusions.....	99
5.2	Recommendations for Future Work.....	100
	BIBLIOGRAPHY	102

SUMMARY

This thesis presents several novel designs of antenna-on-chip and antenna-in-package suitable for millimeter-wave radio frequency wireless communications. The aim of designing those antennas and antenna arrays with excellent performance can be accomplished with the employment of novel artificial periodic structure and the modified soft-surface structure.

Our proposed efficient antenna-on-chip is achieved by combining it with an artificial periodic structure, which can make the lossy silicon substrate equivalently act as a magnetic conductor. This artificial magnetic conductor (AMC) plane replaces the normal perfect electric conductor (PEC) plane and can reflect the incident wave in phase for a low profile antenna, resulting in enhancement of antenna gain performance. In this thesis, a 60-GHz circularly polarized antenna-on-chip employing a modified AMC structure to increase the gain, has been designed, and fabricated using the conventional 0.18- μm CMOS process. From the performance of the antenna, we can see great improvement in the gain and radiation patterns, which confirms the function of the AMC structure.

Along with the above solution for the chip-level antennas, we have also introduced a novel soft-surface structure into the designing of the package-

level antenna arrays using LTCC technology, which faces the problem of surface wave loss. The proposed structure consisting of vias and metal stripes has been embedded around the radiating patch elements to suppress the surface waves and thus improve the antenna performance significantly. We propose two such 4×4 antenna array designs in this thesis.

In addition, two miniaturized substrate integrated multibeam antenna arrays with multiple polarizations are also explored through the development of one dual linear polarization multibeam antenna array and one dual circular polarization multibeam antenna array. By carefully embedding the complicated substrate integrated waveguide feeding network underneath the antenna array, the entire design size can be only the same as the radiating aperture.

LIST OF TABLES

Table 1-1 State-of-art of mm-Wave Antennas-on-Chip Antennas	7
Table 1-2 State-of-art of 60-GHz LTCC Antenna Arrays	13
Table 2-1 Configuration Dimensions of on-Chip Antenna.....	27
Table 2-2 Comparison with Previously Reported 60-GHz CMOS Antenna Designs.....	37
Table 3-1 Comparison of 60 GHz CP Antenna Arrays	41
Table 3-2 Configuration Dimensions of T-probe Patch antenna	43
Table 3-3 Configuration Dimensions of T-probe Slot Antenna	46
Table 4-1 Comparison with Different SIW Multibeam Antennas.....	98

LIST OF FIGURES

Figure 1-1	60 GHz frequency band rules in different countries [38]	2
Figure 1-2	WPAN application [16].....	2
Figure 1-3	Illustration of System-on-Chip [39].....	5
Figure 1-4	CMOS technology structure.....	6
Figure 1-5	Radiation of on-chip antenna in CMOS technology [39]	6
Figure 1-6	TSV-based configurations for system-in-package [45]	9
Figure 1-7	Two basic configurations of the in-package antenna [39]	11
Figure 1-8	System-in-Package in LTCC technology [44]	11
Figure 2-1	Comparison of PEC and AMC Planes [72].....	19
Figure 2-2	Unit cells of several AMCs, from [73].....	20
Figure 2-3	Geometry of proposed novel AMC cell structure	21
Figure 2-4	The HFSS simulation model for an AMC cell: (a) The geometry and the wave-port excitation. (b) Perfect-E and (c) perfect-H symmetry planes.	22
Figure 2-5	Simulated reflection phase of wave incident on AMC structure	23
Figure 2-6	Reflection phase of AMCs with different d	24
Figure 2-7	Reflection phase of AMCs with different W_a	24
Figure 2-8	Reflection phase of AMCs with different L_b	25
Figure 2-9	Geometry of the CP on-chip antenna	27
Figure 2-10	Simulated axial ratio of single loop and double loop CP antennas	28
Figure 2-11	Simulated gain performance of single loop and double loop CP antennas	28
Figure 2-12	Axial ratio performance comparison of antennas integrated with different modified AMC planes.....	29
Figure 2-13	Comparison of antenna with PEC layer and modified AMC layer	30
Figure 2-14	3D explored view of the proposed antenna with the modified AMC plane	30
Figure 2-15	Antenna test set up: (a) pattern measurement and (b) polarization study. AUT: antenna under test	32

Figure 2-16	Photograph of the proposed CP on-chip antenna: (a) attached on a conductor carrier for easy measurement and (b) zoom in under a microscope.....	33
Figure 2-17	Measured and simulated performance of the proposed antenna: (a) return loss, (b) gain, (c) axial ratio	35
Figure 2-18	Measured and simulated XOZ-plane and YOZ-plane radiation patterns at (a) 57 GHz, (b) 60 GHz, (c) 64 GHz	36
Figure 3-1	Geometry of stubbed patch antenna: (a) top view; (b) side view	42
Figure 3-2	Simulated return loss of stubbed patch antenna.....	44
Figure 3-3	Simulated gain performance of stubbed patch antenna.....	44
Figure 3-4	Simulated axial ratio of stubbed patch antenna.....	45
Figure 3-5	3-D radiation pattern at 60 GHz.....	45
Figure 3-6	Geometry of stubbed patch antenna: (a) top view; (b) side view	47
Figure 3-7	Simulated gain performance of slot patch antenna	48
Figure 3-8	Simulated return loss of slot patch antenna.....	48
Figure 3-9	Simulated axial ratio of slot patch antenna	49
Figure 3-10	3-D radiation pattern at 60 GHz.....	49
Figure 3-11	Geometry for patch antenna with a modified soft-surface structure:	52
Figure 3-12	3-D radiation pattern at 60 GHz.....	53
Figure 3-13	Comparison of the gain performances with different inner lengths of the soft-surface	54
Figure 3-14	Comparison of axial ratio performances with different inner lengths of the soft-surface.....	54
Figure 3-15	Array configuration of two adjacent stubbed patch antennas	55
Figure 3-16	Array configuration of two adjacent stubbed patch antennas with soft-surface structure	55
Figure 3-17	Comparison of the mutual coupling with and without soft-surface structure	56
Figure 3-18	Geometry of the 4×4 T-probe stubbed patch antenna array.....	57
Figure 3-19	Structure of the GCPW structure	57
Figure 3-20	Simulated S parameters of GCPW	58
Figure 3-21	Geometry of antenna array with modified soft-surface structure	59

Figure 3-22 Gain comparison of proposed antenna array with and without the modified soft-surface structure	60
Figure 3-23 Electric field distributions on the top surface of the substrate of the patch antenna array with (a) and without (b) the soft-surface	62
Figure 3-24 Antenna test setup	63
Figure 3-25 Simulated and measured return loss of proposed antenna array ..	64
Figure 3-26 Simulated and measured axial ratio of proposed antenna array ..	66
Figure 3-27 Simulated and measured gain of proposed antenna array	66
Figure 3-28 Measured and simulated radiation patterns at (a) 57GHz, (b) 60GHz, (c) 64GHz.....	67
Figure 3-29 Geometry of patch antenna array with the modified soft-surface structure	68
Figure 3-30 Simulated and measured return loss of proposed antenna array ..	69
Figure 3-31 Simulated and measured axial ratio of proposed antenna array ..	70
Figure 3-32 Simulated and measured gain of proposed antenna array	70
Figure 3-33 Measured and simulated radiation patterns at (a) 57GHz, (b) 60GHz, (c) 64GHz.....	71
Figure 4-1 Photograph of the beam-steering antenna in package [100]	73
Figure 4-2 Configuration of the proposed interconnection between layers: (a) without phase compensation, (b) with phase compensation, and (c) top view.	77
Figure 4-3 Phase characteristics of the proposed interconnection between layers.....	77
Figure 4-4 Configuration of the proposed integrated multibeam array antenna and the CPW feed structure.	78
Figure 4-5 Sketch of the integrated multibeam antenna	79
Figure 4-6 Sketch of the folded Butler matrix: (a) 2-D; (b) 3-D.	80
Figure 4-7 Configuration of the E-plane coupler incorporating a 45° phaser:	81
Figure 4-8 Simulated results of the E-plane coupler incorporating a 45° phaser	82

Figure 4-9	Configuration of two overlapped H-plane couplers incorporating layer- to-layer transitions: (a) 3-D configuration, and (b) top view.	83
Figure 4-10	Magnitude Characteristic of two overlapped H-plane couplers incorporating layer-to-layer transitions	83
Figure 4-11	Phase characteristics of two overlapped H-plane couplers incorporating layer-to-layer transitions	84
Figure 4-12	Configuration of the proposed 45° linear polarization antenna: (a) 3-D configuration, and (b) top view	85
Figure 4-13	Mutual couplings between elements versus their distance at different operating frequencies	85
Figure 4-14	Configuration of the proposed cavity antenna array: (a) 1×4 45° LP array, (b) 4×4 45° LP array, and (c) 4×4 CP array.	86
Figure 4-15	Simulated reflection coefficient of the proposed 4-element linear antenna array.....	87
Figure 4-16	Simulated yoz-plane patterns of the proposed 4×4 45° LP array antenna (The phase for ports 1~4: case 1: 0°, 45°, 90°, and 135°; case 2: 0°, 135°, 270°, and 405°).....	87
Figure 4-17	Photograph of the fabricated dual linear-polarization substrate integrated multibeam array antenna.	88
Figure 4-18	Reflection coefficients of the fabricated dual linear-polarization substrate integrated multibeam array antenna excited by ports 1~4.	89
Figure 4-19	Isolation coefficients of the fabricated dual linear-polarization substrate integrated multibeam array antenna excited by port 1.	89
Figure 4-20	Isolation coefficients of the fabricated dual linear-polarization substrate integrated multibeam array antenna excited by port 2.	90
Figure 4-21	Far field measurement setup	90
Figure 4-22	Simulated and measured radiation patterns of the fabricated dual linear-polarization multibeam array antenna at different frequency excited at port 1.	91
Figure 4-23	Simulated and measured radiation patterns of the fabricated dual linear-polarization multibeam array antenna at different frequency excited at port 2	92

Figure 4-24 Simulated yoz-plane patterns of the proposed 4×4 CP array antenna (The phase for ports 1~4: case 1: 0°, 45°, 270°, and 315°; case 2: 0°, -45°, 90°, and 45°).....	93
Figure 4-25 Photograph of the fabricated dual circular-polarization substrate integrated multibeam array antenna	95
Figure 4-26 Simulated and measured radiation patterns of the fabricated dual circular-polarization multibeam array antenna at different frequencies excited at port 3.....	97

LIST OF ACRONYMS

AMC	Artificial Magnetic Conductor
AUT	Antenna under Test
BELO	Back End of Line
BFN	Beam Forming Network
CMOS	Complementary Metal Oxide Semiconductor
CPW	Coplanar Waveguide
DNM	Double Negative Material
EBG	Electromagnetic Band-Gap
FSS	Frequency Selective Surface
GCPW	Grounded Coplanar Waveguide
HIS	High Impedance Surface
LTCC	Low Temperature Cofired Ceramic
mm-Wave	Millimeter-Wave
PCB	Printed Circuit Board
SIW	Substrate Integrated Waveguide
TSV	Through Silicon Via
UC-EBG	Uniplanar-Compact Electromagnetic Band-Gap
UC-EPG	Uniplanar-Compact Photonic Band-Gap
VNA	Vector Network Analyzer
WPAN	Wireless Personal Area Networks

Chapter 1: Introduction

1.1 Background of 60-GHz Wireless Communications

Wireless communication technology has evolved substantially these years and this flourishing trend is surely expected to continue. Nowadays, inspired by the rapid proliferation of high definition video centric broadband applications, there is rapid development of gigabit wireless communication systems working at millimeter-wave (mm-Wave) frequencies. The mm-Wave frequency spectrum is defined to be 30 to 300 GHz, which corresponds to wavelengths from 10 to 1 mm. Within this wide range of spectrum, the bandwidth 57~66 GHz is unlicensed. This thesis will specifically focus on the 60-GHz wireless communication systems.

The history of mm-Wave technology began with the Indian physicist J. C. Bose, who in 1895 demonstrated wireless signaling at 60-GHz frequency with several microwave components including horn antennas [1]. In 1947, the American physicist J. H. Van Vleck observed that the oxygen molecule absorbs electromagnetic energy more significantly at 60-GHz than at other frequencies [2]. From the 1960s onward, explorations into this area for military and space applications have been conducted for almost 20 years [3]-[4]. In 2000, Japan first presented 60-GHz regulations for this unlicensed spectrum from 59 to 66 GHz, where the maximum transmit power is 10 dBm, with a maximum antenna gain of 47 dBi and maximum bandwidth of 2.5 GHz [5]. Following that, the US announced a spectrum of 7 GHz from 57 to 64 GHz for unlicensed use in 2004 [6]. The Canada was harmonized with this spectrum [7]. However, a narrower bandwidth of 3.5 GHz was defined in Australia [8] and a wider bandwidth of 9 GHz was stipulated in Europe [9]. Fig. 1-1 illustrates these different regulations.

Owing to the high atmospheric absorption of the radio waves, the 60 GHz frequency band is only suitable for low power and short range communications. In fact, the propagation loss can be exploited to prevent eavesdropping, reduce interference and increase frequency reuse. As shown in

Fig. 1-2, a typical application of this is in wireless personal area networks (WPAN), where all the network nodes are contained in a single room and the communications range is typically within 10 meters. Interesting applications such as uncompressed high definition video streaming, mobile distributed computing, wireless gaming, Internet access, and fast large file transfer, are envisioned and detailed in the 802.15.3c usage model document [10]. This has attracted both large consumer electronics and small start-up companies to explore this space. To what extent and in what capacity these applications utilized will be determined by the ability of research companies.

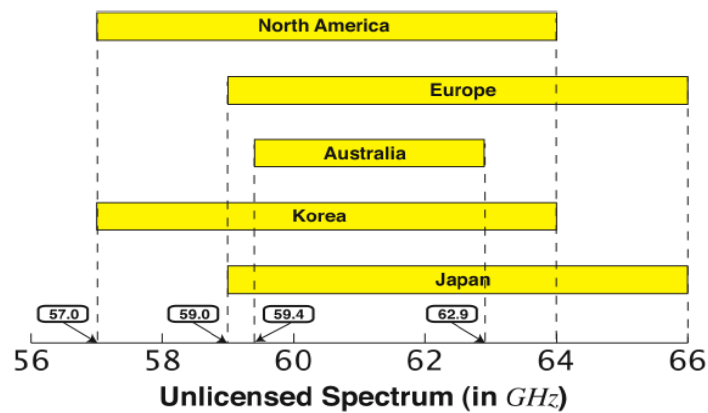


Figure 1-1 60 GHz frequency band rules in different countries [38]

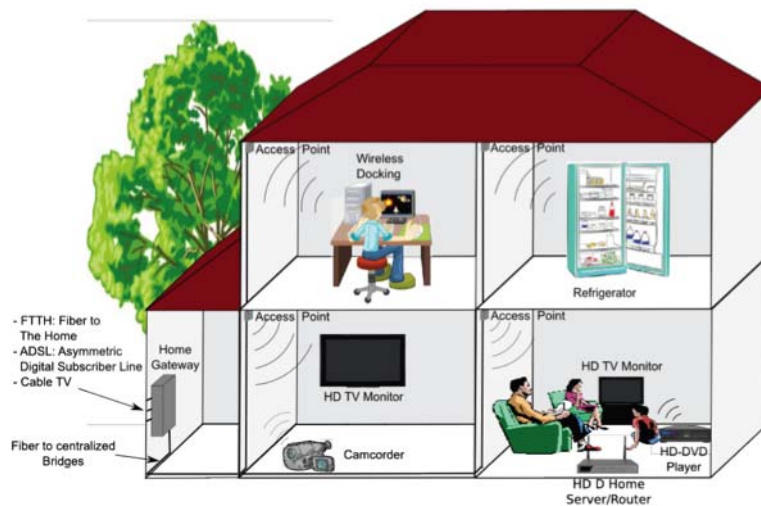


Figure 1-2 WPAN application [16]

Currently, there are three leading groups working on the standards of 60 GHz wireless communications systems. The first is the IEEE 802.15.3 Task Group formed in March 2005, which aims to standardize 60-GHz radios. To encompass available but inconsistent unlicensed frequencies, the standard divides nearly 9 GHz of spectrum from 57.24–65.88 GHz into four 2.16-GHz channels. The mmWave WPAN will allow high coexistence with all other microwave systems in the 802.15 family of WPANs. It will support greater than 1 Gbps applications such as high speed internet access, video on demand and home theatre. Very high data rates in excess of 2 Gbps will be provided for simultaneous time critical applications such as real time multiple HDTV video streaming and wireless data bus for cable replacement.

The second group working on 60 GHz wireless communications systems is the WirelessHD consortium, which is led by almost all major technology and consumer electronics companies including NEC, Toshiba, Panasonic, Sony, LG, Intel, SiBeam and Broadcom, etc. WirelessHD is aimed at defining a next generation wireless digital interface specification for consumer electronics and PC products. Specifically, it will enable wireless connectivity for streaming high-definition audio, video and data between source devices and displays. A typical application of WirelessHD is to connect a 1080p HD television with an HD set-top box, Blue-ray disc, or HD camcorder. WirelessHD is effectively a wireless replacement for a high-definition multimedia interface cable. In its first generation implementation, it is expected that high-speed rates up to 4 Gbps will be achieved, but its core technology is capable of theoretical data rates as high as 25 Gbps.

Besides the above two groups that are working on communication standards, the Wireless Gigabit Alliance (WiGig) is a newly formed organization promoting the adoption of multi-gigabit speed wireless communications technology operating over the unlicensed 60 GHz frequency band. The creation of WiGig (IEEE 802.11 ad) was announced on May 7, 2009. The WiGig specification allows devices to communicate without wires at multi-gigabit speeds. It enables high performance wireless data, display and audio applications that supplement the capabilities of today's wireless LAN

devices. WiGig tri-band enabled devices, which operate in the 2.4, 5 and 60 GHz bands, will deliver data transfer rates up to 7 Gbit/s, about as fast as an 8 antenna 802.11ac transmission, and nearly 50 times faster than the highest 802.11n rate, while maintaining compatibility with existing Wi-Fi devices. However, the promised 7 Gbit/s rate makes use of the 60 GHz band which cannot go through walls; it is a line-of-sight technology. When roaming away from the main room the protocol will switch to make use of the other lower bands at a much lower rate, but which propagate through walls. WiGig competes with WirelessHD in some applications. WirelessHD transmits in the same 60 GHz band used by WiGig.

Though very promising the corresponding applications are, the 60-GHz wireless communications encounter several challenges in implementation, which can be broadly classified into four categories: characterization of propagation channels, antenna technology, transceiver integration, and digital signal processing [11]. The antenna technology affects radio propagation channels, transceiver designs, and choices of digital modulation schemes. As a result, it hinders the establishment of a 60 GHz link and its reliability. To achieve a distance of 8–10 meters and to suit the consumer electronics market, the antennas must have moderately high gain, be of low cost and be compact. They should be compatible for integration to complementary metal oxide semiconductor (CMOS) transceivers. Antennas and antenna arrays for highly integrated radios operating at 60-GHz or above have received great attention [12]-[15], especially the antenna-on-chip and antenna-in-package solutions [16]-[37]. This is not only because the antenna form factor at 60-GHz is in the order of millimeters or less, which opens up new integration options on a chip or in a package, but also offers obvious advantages in terms of cost, compactness, reliability, and reproducibility for both chip-level antenna and package-level antenna solutions. In sections 1.2 and 1.3, newly proposed antennas-on-chip and antennas-in-package for highly integrated 60-GHz radios will be addressed and analyzed.

1.2 Antennas-on-Chip

1.2.1 Literature Review

Traditionally, wireless systems have been developed by integrating distinct functionality modules, either in a horizontal or a vertical fashion. This method offers the option of using the best technology for each component. For example, digital circuits are best suited for CMOS technology; power amplifiers may use III–V compound semiconductor technology; and antennas function efficiently on low-loss printed circuit boards (PCBs) such as FR-4, and Duroid. However, integrating these different technologies becomes difficult, especially at higher frequencies, as the interconnection is lossy and the specialized processes such as flip-chip bonding increases the costs. As shown in Fig 1-3, assisted by the advances in silicon technologies such as CMOS, the on-chip antenna approach has triggered great interest, as it allows on-chip integration of digital baseband and a complete RF front-end [39].

However, there are two challenges for on-chip antennas: low antenna gain resulting from losses in low-resistivity silicon substrates, layout constraints due to metallization density rules and difficulties of on-wafer characterization.

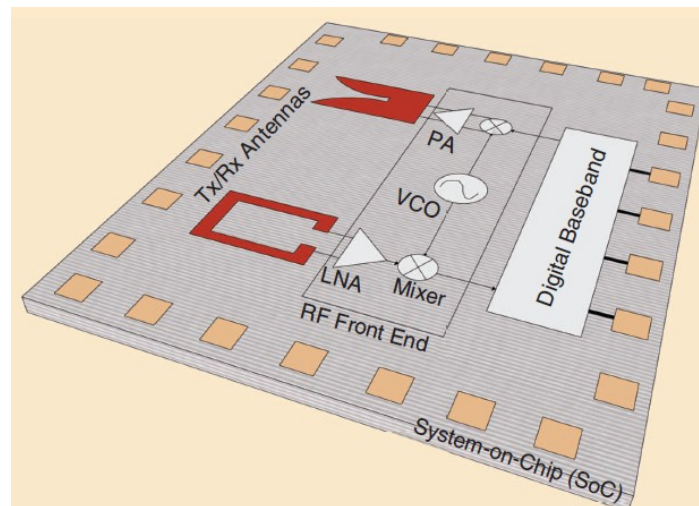


Figure 1-3 Illustration of System-on-Chip [39]

The current semiconductor technologies are not equipped to support high-efficient antennas-on-chip. This is because the semiconducting substrates typically have a low resistivity of $10 \Omega\text{-cm}$, which is beneficial for ICs (as it

avoids latch-up) but disastrous for on-chip antenna design. For instance, a typical $0.18\mu\text{m}$ silicon based CMOS metal stack, shown in Fig. 1-4, consists of six metal layers placed on top of a $300\mu\text{m}$ thick substrate.

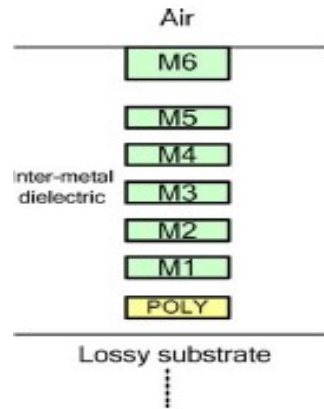


Figure 1-4 CMOS technology structure

The antenna, which converts RF power from the circuits to electromagnetic (EM) radiation, finds a low-resistive path through the substrate and thus incurs gain degradation. Moreover, the high dielectric constant ($\epsilon=11.9$) of silicon substrate in $0.18\mu\text{m}$ standard CMOS technology, which causes most of the power to be confined in the substrate instead of being radiated into free space, further degrades the radiation efficiency. Fig. 1-5 illustrates the mechanism of EM radiation from on-chip antenna using silicon based technology ($\epsilon=11.7$).

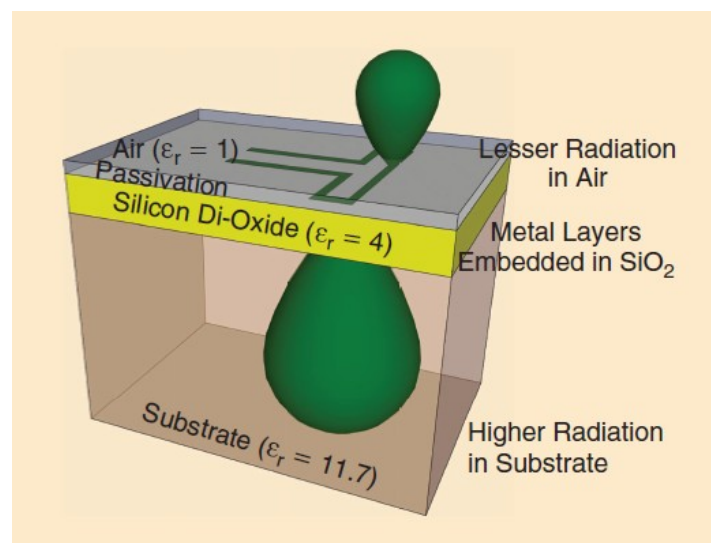


Figure 1-5 Radiation of on-chip antenna in CMOS technology [39]

1.2.2 State-of-the-Art on-Chip Antennas

Having discussed the advantages and challenges of chip-level antennas, hereafter we provide an overview of the state-of-the-art in antennas-on-chip using various semiconductor technologies. A majority of these antennas in the last few years have been implemented in bulk silicon-based technologies such as CMOS and SiGe. This is because the CMOS technology has become the mainstream choice for IC designs. CMOS also supports a high level of integration, offers improved process options and lower costs for mass production. Furthermore, in comparison to two or three metal layers offered in GaAs, six to nine metal layers are available in the CMOS processes, adding flexibility for antennas-on-chip.

Table 1-1 State-of-art of mm-Wave Antennas-on-Chip Antennas

Architecture & Reference	Process Technology	Chip Area (mm×mm)	Gain @ Frequency
Quasi-Yagi [20]	Post-back-end-of-line	0.2×2	-12.5 dBi @ 65 GHz
Invert-F [20]	Post-back-end-of-line	0.4×1.3	-19 dBi @ 61 GHz
Triangular Monopole Antenna [41]	0.18-um CMOS	1×0.81	-9.4 dBi @ 60 GHz
Yagi Antenna with CPW Feed [40]	0.18-um CMOS	1.1×0.95	-10.6 dBi @ 60 GHz
Yagi, Dipole, Rhombic, Loop Antennas [42]	0.18-um CMOS	1.2×0.05, 1.2×0.03, 5×5, 5×5	-3.5 dBi, -7.3 dBi, -1.2 dBi, -3.4 dBi @ 60 GHz
Cavity-Backed Slot Antenna [46]	CMOS	0.6×1.2	-2 dBi @ 140 GHz
Microstrip Patch [47]	SiGe BiCMOS	0.97×0.69	0.7 dBi @ 94 GHz

Table 1-1 lists some of the state-of-the-art mm-Wave antennas-on-chip based on CMOS and SiGe technology. The behavior of these antennas is characterized by low gain and poor radiation. Y. P. Zhang, *et al.*, have implemented both inverted-F and quasi-Yagi antennas on a standard low resistivity substrate (10 Ω·cm) [20]. These antennas were implemented with a specialized BEOL technology to overcome the challenges caused by the

substrate. In their fabrication, proton implantation in the substrate was used to increase resistivity, reduce substrate losses, and improve performance. Using the Zeland IE3D simulation tool, the authors found that this inverted-F antenna achieved a radiation efficiency of 3.5%, which is unfortunately typical in much of the literature to date. The quasi-Yagi in [20] was found to exhibit a maximum gain of -12.5 dBi at 65GHz, while the simulated efficiency was 5.6%. The return loss and maximum gain were measured with a probe station and network analyzer.

In 2008, researchers from National Cheng Kung University created a coplanar waveguide (CPW) feed structure and an on-chip 3-element Yagi antenna in standard 0.18 μm CMOS technology [40]. The authors used Ansoft HFSS to simulate the antenna structure and obtain a radiation efficiency of approximately 10%. These authors also implemented a triangular monopole antenna in the same 0.18 μm CMOS technology [41]. The simulated radiation efficiency of this antenna was approximately 12%. The maximum value of the gain was calculated from S-parameters to be -9.4 dBi at 60 GHz. In 2009, Theodore S. Rappaport and his students at the University of Texas at Austin presented several on-chip antenna structures that may be fabricated with standard CMOS technology for use at millimeter wave frequencies, including dipole, Yagi, rhombic, and loop antennas [42]. They found the key relationships between the dipole and the Yagi element spacing and found that the antenna performance is maximized when the antennas are placed at the edge of the die. At the corner of the chip, the dipole and the 2-element Yagi had maximum gains of -6.7 dBi and -3.5 dBi, respectively.

It is clear from past work that the design and implementation of antennas-on-chip is neither easy nor efficient. Gain and radiation efficiencies are very poor.

1.2.3 Ways to Improve the Antennas-on-Chip

First of all, efficiency and gain of antennas-on-chip can be improved by using high resistivity substrates such as Through Silicon Via (TSV). TSV technology is employed in 3-D integrated circuits, consisting of stacking

silicon wafers or dies, and the vias interconnecting these wafers. As the most advanced technology, TSV does not only have the fabrication character of multilayer and via structure, which greatly reduces the size and the interconnection mismatch of integrated system, but also achieves excellent fabrication accuracy suitable for mm-Wave applications. The configuration of an integrated system using TSV has been presented in Fig 1-6.

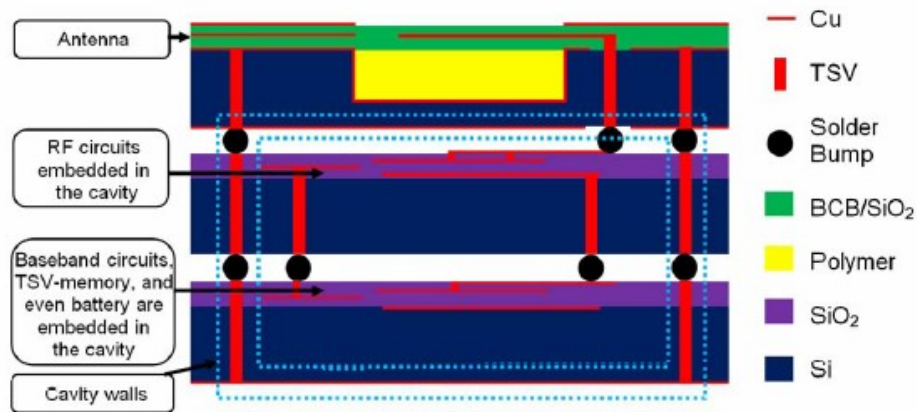


Figure 1-6 TSV-based configurations for system-in-package [45]

So far, this process, however, is not the mainstream in chip fabrication as the bulk CMOS is, because of the complexity and extremely expensive cost. In addition, the micromachining technique and the proton implantation process have also been proposed to reduce silicon substrate loss and improve the radiation efficiency of antennas-on-chip [43].

Micromachining techniques use either wet or dry backside etching to selectively remove parts of the bulk silicon substrate. In the wet etching process, a silicon wafer is typically submerged in a chemical liquid to create cavities and membranes in the substrate. However, the etching is restricted by the crystal planes in the substrate, thus leaving the etched cavities with slanted walls. In the dry etching process, a single wafer is put in an evacuated chamber where plasma is generated to etch the silicon substrate. A disadvantage of dry etching is its high cost because of the expensive equipment used and time required. To solve this contradictory requirement of high and low substrate resistivity for single-chip mm-Wave radios, a proton implantation process has been developed to increase the resistivity of silicon substrates from $10 \Omega \cdot \text{cm}$ to $10^6 \Omega \cdot \text{cm}$ underneath selected devices [43].

Generally speaking, all the above solutions dealing with the fabrication improvement reduce the level of system integration and increase the cost. Instead of increasing fabrication difficulty, the method of employing artificial magnetic conductor (AMC) has been sought to achieve the same performance in standard bulk silicon. A ground plane at the bottom of the silicon substrate induces oppositely charged image current that destructively interferes with the antenna currents. The AMC isolates the ground plane by inducing image currents in its own surface, constructively interfering with the antenna currents and boosting the antenna efficiency. Taking advantage of the multiple metal layers in today's silicon technologies, AMCs can be implemented without any cost or post-processing penalties. Specific AMC-based on-chip antenna will be designed and analyzed in chapter 2 with more details.

1.3 Antennas-in-Package

1.3.1 Literature Review

The integration solution of combining an antenna (or antenna array) with a highly integrated radio die into a standard surface embedded in package device is a recent and important innovation in the miniaturization of wireless systems. Among these integrated systems, the antennas-in-package have been considered to be a very promising solution for the highly integrated mm-Wave wireless systems. Fig 1-7 shows two basic configurations of the package-level antenna solution to highly integrated mm-Wave wireless systems. The first configuration contains two cavities, one of which holds the integrated radio die, while the other filled by air is employed for antenna radiation. The second in-package solution uses multilayer structure in the way of vertical stacking.

Fabrication technologies suitable for realizing in-package systems with antennas in highly integrated 60-GHz radios are limited within the choices of high resistivity silicon, Teflon, ceramics, and polymers. Among them, low temperature cofired ceramic (LTCC) technology is an excellent candidate because of its advantages of multilayer configuration, flexible metallization, and low fabrication tolerance [36], [48]-[50]. Compared with conventional multilayer PCB technology, it is easier to use LTCC technology in the

realization of blind vias and across-layer connection by vias. There exist several LTCC processes in the mainstream market nowadays. Ferro A6 is the most popular LTCC material for 60-GHz applications, which can be characterized over frequencies up to 110 GHz. Over the wideband of 60 GHz to 94 GHz, the Ferro A6 presents a dielectric constant of 5.9 ± 0.2 and loss tangent of 0.002. Based on the stable material characteristics and novel structural properties employed, LTCC technology has been successfully used by researchers to design functional packages and antennas for applications in the 60-GHz band. Fig 1-8 shows one specific example of a LTCC multilayer integration system containing various modules inside a compact area.

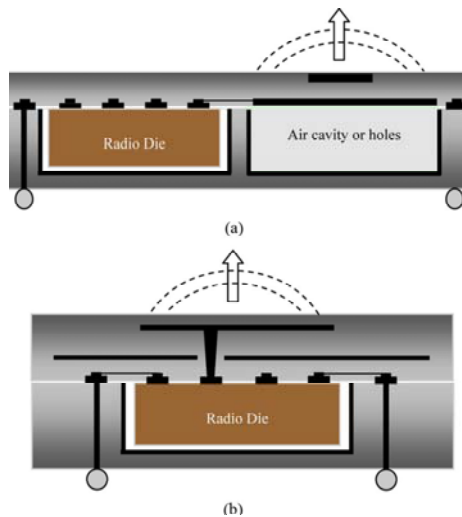


Figure 1-7 Two basic configurations of the in-package antenna [39]

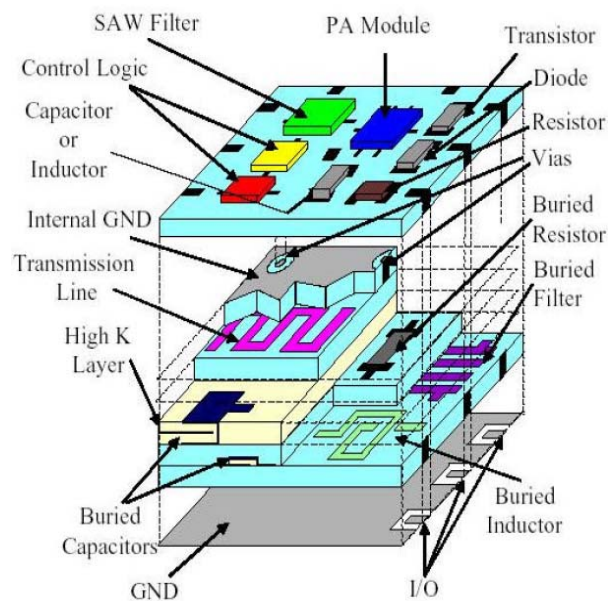


Figure 1-8 System-in-Package in LTCC technology [44]

Due to the low transmission power, large propagation loss, and high data rate of the mm-Wave wireless systems, the package-level antennas or antenna arrays are required to obtain high gain and broad bandwidth. Commonly, a bandwidth of at least 15% and a minimum gain of 15 dBi should be accomplished. The high-gain antenna array designs will reduce the multipath effect, and as a result simplify the 60-GHz wireless systems. A single antenna element can hardly meet the gain requirement, so it is necessary to extend antennas to antenna arrays. Hereafter in this thesis, the part of package-level arrays will be illustrated and analyzed in details.

1.3.2 State-of-the-Art in-Package Antenna Arrays

Various choices of array elements such as patch, dipole, slot, and others have been used in 60-GHz in-package applications. The advantages and disadvantages of these array elements are well known. A patch antenna, either aperture-coupled or probe fed, is commonly employed because the radiating patch can be optimized independently regardless of the feeding mechanism. Different from the patch antenna, the popularity of the slot antenna element comes from the mature research of substrate integrated waveguide (SIW). Among the various kinds of feeding mechanism, such as microstrip line, stripline, SIW and so on, the microstrip line is more convenient in the interconnection with the radio die, while SIW has lower transmission loss. In [48], the SIW feed network is used in aperture fed cavity antenna array, achieving a bandwidth of 17.1%.

The challenge in designing LTCC antenna arrays is how to enhance gain performance because the high permittivity of the LTCC substrate inherently brings in great surface wave. Table 1-2 lists some previously published 60-GHz antenna arrays based on LTCC technology, where different methods of suppressing the surface wave loss are studied. First of all, processing a cavity inside the substrate will reduce the effective dielectric constant and thus suppress the surface-wave [49]. Secondly, by removing part of the substrate around the radiating patch antennas in [52], open air cavities have been created to reduce the surface wave. However, these two kinds of structures

require complicated process in fabrication, resulting in high cost and probability of deformation.

Table 1-2 State-of-art of 60-GHz LTCC Antenna Arrays

architecture of Antenna Array	Scale of Array	Impedance Bandwidth	Peak Gain
Grid Antenna Array [36]	$13.5 \times 8 \times 1.265 \text{ mm}^3$	14.3%	14.5 dBi
Patch Antenna Array with UC-EBG [51]	$18.5 \times 18.5 \text{ mm}^2$ 4×4 units	5.4%	18 dBi
Patch Antenna Array with Open Air Cavities [52]	4×4 units	13%	16.5 dBi
Patch Antenna Array with Embedded-cavities [49]	$18.6 \times 18.6 \text{ mm}^2$ 4×4 units	9.5%	18.2 dBi
Patch Antenna Array with Soft-surface [53]	$14.4 \times 14.4 \text{ mm}^2$ 4×4 units	29%	17.5 dBi
SIW Fed Cavity Antenna Array [48]	$47 \times 31 \times 2 \text{ mm}^3$ 8×8 units	17.1%	22.1 dBi

Instead of changing the fabrication process, artificial structures can be used to reduce the surface wave and mutual coupling between antennas. For example in [51], a uniplanar-compact electromagnetic band-gap (UC-EBG) structure is placed around the patch antennas to increase the gain performance effectively. However, this addition of UC-EBG structure not only enlarges the total array size but also narrows the bandwidth. Another method of using the artificially soft-surface structure to improve antenna performance is illustrated in [53]. The soft-surface structure will not increase the overall area or the cost, through the use of multilayer LTCC technology. More details and analysis will be provided in chapter 3, where two circularly polarized antenna arrays with soft-surface have been designed.

As discussed above, the majority of 60-GHz array antennas are fixed-beam broadside. In practical wireless applications, steerable antenna arrays can benefit the selection of the best signal path. Multibeam array antennas can be used to form switched-beam array antennas with a switch circuit in front of the

fixed beam-forming network such as a Rotman lens or a Butler matrix. Chapter 4 will demonstrate the procedures in designing multibeam array antennas.

1.4 Thesis Outline

In consideration of the demanding operating requirements for 60-GHz antennas and the challenges in our current research, we shall focus on the design and analysis of novel antenna-on-chip and antenna-in-package suitable for practical wireless applications. More specifically, we aim at designing high gain antennas and antenna arrays by employing novel artificial structures, together with novel multibeam antenna arrays. The structure of this thesis is organized as follows:

Chapter 2 first explores the theory of AMC structures and then presents one novel AMC structure, which has wider bandwidth in reflecting incident wave. At the same time, the design of a 60-GHz on-chip loop antenna on silicon substrate is discussed. The proposed design has an enhanced circular polarization bandwidth because of a parasitic inner loop. By combining this modified AMC plane, a high gain antenna-on-chip is obtained and can be fabricated in CMOS technology.

Apart from the above solution for the chip-level antenna, chapter 3 introduces a novel soft-surface structure in the designing of package-level antenna arrays in LTCC technology, in order to solve the surface wave loss problem. The proposed structure consisting of vias and metal stripes has been embedded around the radiating patch elements to suppress the surface waves and thus improve the antenna performance significantly. After analyzing the function of soft-surface structure, we present two 4×4 circularly polarized antenna arrays with novel soft-surface structure in LTCC technology.

In chapter 4, miniaturized substrate integrated multibeam antenna arrays with multiple polarizations are demonstrated through the development of one dual linearly polarized and one dual circularly polarized substrate integrated multibeam antenna arrays. By carefully embedding the complicated SIW

feeding network underneath the antenna array, the whole design size can be only the same as the radiating aperture.

Last but not least, a conclusion of the thesis, as well as the limitations of current work, is presented in chapter 5. Some practical suggestions about the future work will also be discussed.

1.5 Some Original Contributions

In this thesis, the following original contributions have been made:

- 1) A novel AMC structure has been proposed, which achieves wider bandwidth compared with previous structures. Theoretical analysis and parameter study have been provided in detail as well. This AMC plane is capable of enhancing the antenna-on-chip performance by producing constructively in-phase reflections with the incident wave at the specified operating frequency band.
- 2) A CP antenna has been designed at 60-GHz in CMOS technology. Prior to this, most of the 60-GHz on-chip antennas were linearly polarized. Along with the character for wideband circular polarization, this AMC based antenna-on-chip also achieves better gain performances than previous conventional chip-level antennas.
- 3) Two kinds of T-probe fed antennas have been designed for 60-GHz wireless communication systems in LTCC technology, both of which are wideband circularly polarized antennas. The first patch antenna realizes the circular polarization character by adding a stub at the corner of the patch, while the second slot antenna achieves this by cutting two corners off and inserting one 45° located slot in the middle of the patch.
- 4) A modified soft-surface structure has been proposed to improve the circularly polarized antenna array performance. Corresponding analysis about the surface wave suppression and mutual coupling reduction are illustrated. Two 4×4 CP antenna arrays combining the formerly

discussed T-probe antenna with soft-surface structure have been designed in LTCC technology, which are currently in fabrication process.

- 5) Previously, beam forming network and radiator array are placed side by side in 2-D plane to make up a multibeam array. In order to reduce the whole size, a folded Butler matrix in 3-D using LTCC multilayer technology has been proposed. The total size of the multibeam array only equals to that of the radiating aperture, meaning the feeding Butler matrix is completely hidden underneath the radiators. This innovative structure results in a remarkable miniaturization.
- 6) This thesis also realizes the possibility of combining the multiple-beam and multiple-polarization character together in one same antenna array. Two miniaturized substrate integrated multibeam antenna arrays with multiple polarizations have been presented, one of which is a dual linearly polarized array and the other is a dual circularly polarized array. Each multibeam antenna has four switchable beams with different pointing directions. Each beam direction has two orthogonal linearly polarized or circularly polarized modes, therefore allowing for polarization diversity.

Chapter 2: AMC-Based on-chip Antenna Design

2.1 Artificial Magnetic Conductor Structure

2.1.1 Literature Review

Periodic structures which act as artificial metamaterials have become a promising research area in recent years. They are able to behave like known materials, as well as qualitatively respond in ways which are not known to occur in nature. These periodic structures, such as electromagnetic bandgap (EBG), Artificial Magnetic Conductor (AMC), Double Negative Material (DNM), Frequency Selective Surface (FSS), High Impedance Surface (HIS) and so on can benefit many microwave related applications.

In 1999, Sievenpiper *et al.* first presented a mushroom EBG structure, which turned out to be very useful in commercial applications [54]-[57]. This mushroom EBG structure consists of an FSS plane, a ground plane and vias connecting each FSS units to the ground. The shape of the FSS unit could be either square or hexagonal depending on the specific situation. Its bandgap character comes from each periodic unit's equivalent behavior as a resonant LC circuit. The spacing between the edges of the elements controls the capacitance, and the magnetic flux created between the patches and the ground plane defines the inductance.

First introduced by T. Itoh *et al.*, [58]-[61], the uniplanar compact photonic bandgap (UC-PBG) structure can also realize similar characters, which have been utilized for antennas, and microwave circuits applications. The UC-PBG structures again consist of a ground plane and a plane of periodically located conducting elements. Different with the mushroom surface, the UC-PBG structures realize the bandgap properties with more complex element shapes instead of vias.

The AMC structure, also considered as HIS or Perfect Magnetic Conductor (PMC), provides a high impedance surface causing reflection phase changes

from 180° to -180° as the frequency increases. The analysis of AMC structures will be discussed in details next section.

Because of their unique microwave character, these artificial periodic materials have been introduced in antenna systems to enhance performance, especially in improving the radiation pattern, enhancing bandwidth and reducing size. Antennas composed of single negative materials that resonantly couple to the external radiation was proposed by Isaacs et al. [62]. Qureshi et al. also proposed a metamaterial ring antenna with efficiency of 54% [63]. Mosallaei and Sarabandi introduced the concept of magneto–dielectrics design, which was effective in patch antenna miniaturization [64]. Bilotti further presented the design of miniaturized metamaterial patch antenna with negative permeability loading [65]. More recently, the concept of metamaterial-based antenna, first proposed by Ziolkowski and Erentok [66]–[69], proved to be an excellent approach to reduce the antenna size while maintaining satisfactory antenna performance.

2.1.2 Employment of AMC in Antenna Designs

To show the advantage of this property, an example is the electric linear wire antenna near a PEC reflector: its separation must be a quarter-wavelength for optimum radiation due to the reverse image currents which reduce the radiation efficiency. For PMC, on the other hand, the dipole can be placed immediately above the reflector, which reduces its profile to about $\lambda/20$ without affecting its performance. This is due to the fact that the reflection coefficient of the PEC surface is $\Gamma = -1$, but that of the PMC is $\Gamma = +1$. Moreover, the reflection phase of AMC is $R = +1$ at a certain frequency, which resembles an ideal PMC that does not exist in nature. A PEC causes a phase reversal, while an AMC does not. To illustrate the fundamental principle, Fig.2-1 compares the AMC ground plane with the traditional PEC ground plane in wire and microstrip antenna designs [70]–[71]. As it is known, the image current introduced by a PMC is in parallel and in phase with its source, which is located horizontally above it. This fact is usually used to describe the improvement in the antenna performance when AMCs or HISSs are employed.








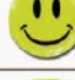
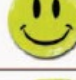



Options	Efficiency	Low Profile	Antennas
			Monopole
			N/A
			Microstrip antennas
			New frontier: Wire-EBG

Figure 2-1 Comparison of PEC and AMC Planes [72]

2.1.3 Some Classic AMC Structures

Several different AMC unit cells with various structures are presented in Fig. 2-2. A patch-type AMC unit cell, shown in Fig. 2-2(a), as well as its modified version loaded by slots, shown in Fig. 2-2(c), has the same reflection phase response. However, extending the middle arms to touch the unit cell boundaries, i.e., connecting the adjacent unit cells as shown in Fig. 2-2(d), completely changes the reflection phase characteristics. This metallization has been introduced in [58] as one of the uni-planar EBGs (UC-EBGs). At this frequency range, the metallization, shown in Fig. 2-2(d) is no longer an AMC. This implies that the existing capacitance between the adjacent unit cells play a key role in reducing the resonance frequency and consequently compact unit cell design.

The metallization, shown in Fig. 2-2(c), has the well known Jerusalem cross shape. In Fig. 2-2(f), only two middle arms, which connect the four sides, are removed. Interestingly, the reflection phases of both of these metallization are very close. This indicates that the middle cross-shape conductors play an insignificant role compared to the side conductors.

The other class of metallization studied in this work is the ring-type AMC unit cells. Some variations of this kind of metallization are shown in Fig. 2-2(b), (g), (h), (i) and (j). The loading of the middle of the ring-type unit cells does not have any significant effect on the reflection phases. On the other hand, when the outer ring is loaded by small gaps, for example the one shown in Fig.

2-2(k), reflection phase response drastically changed. At this frequency, the metallization in Fig. 2-2(k) no longer represents an AMC unit cell, since the reflection phase is between 125 and 150. Therefore, the outer ring determines the first resonant frequency in this type of metallization.

Moreover, the characteristics of AMC are greatly dependent on the gaps between conducting parts of the two adjacent unit cells. As a result, the design of AMCs relies very much on the precision limitation by the etching fabrications. It is desirable to have more compact unit cells when advanced fabrication technology is employed. The smaller the gap, the more compact the unit cell will become.

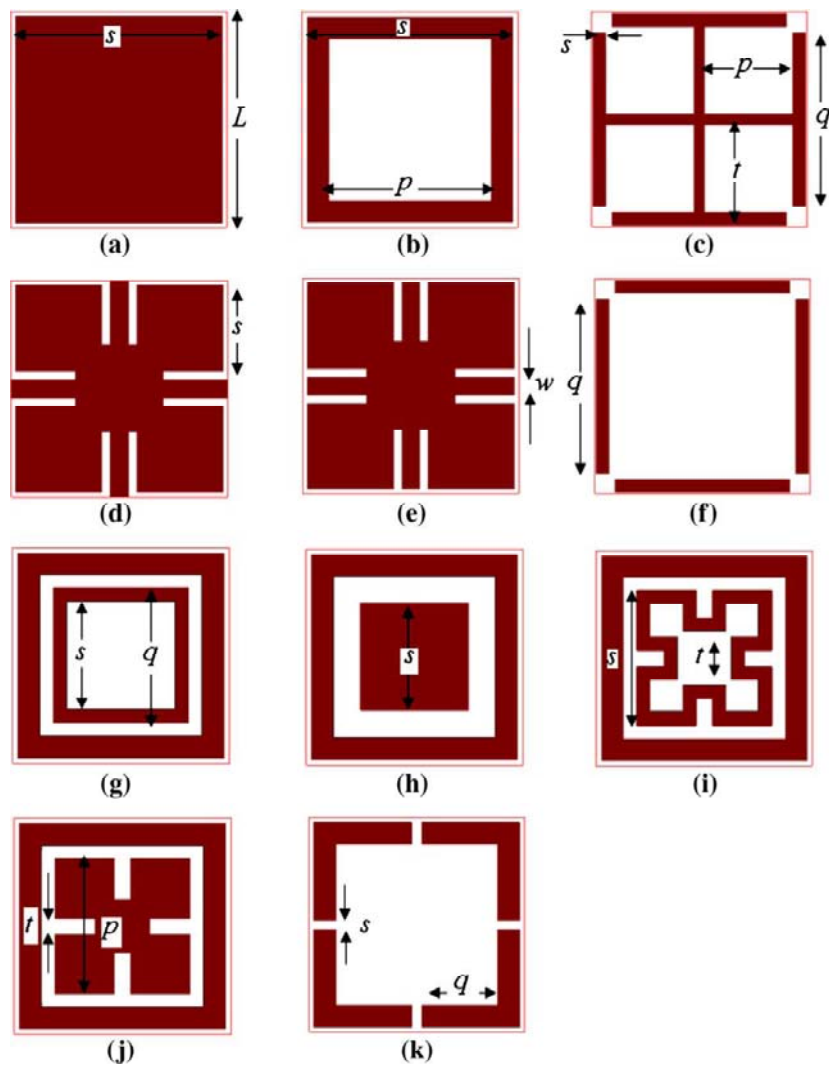


Figure 2-2 Unit cells of several AMCs, from [73]

2.2 Analysis of a Novel AMC Structure

2.2.1 Unit Structure

In this section, a novel AMC structure has been designed, simulated and fabricated onto an on-chip antenna using standard 0.18 μm CMOS technology. The property of the AMC structure will be presented in detail.

In standard six-metal-layer 0.18 μm CMOS technology, the maximum metal strip size on M1 is 30 μm by width and 500 μm by length, while the slant metal strips must be in 45° degree and the minimum fabricated size must larger than 5 μm . In order to meet these fabrication guidelines, we present a novel planar AMC structure. Fig.2-3 shows the top view of an AMC unit cell. The substrate is lossy silicon with permittivity = 11.9, loss tangent = 0.02, bulk conductivity = 10s/m, and thickness= 300 μm . By changing L_a , L_b and W_a , the operating center frequency can be adjusted to the desired frequency. The structure is finally optimized to be $L_a = 0.145$ mm, $L_b = 0.14$ mm, $L_c = 0.15$ mm, $W_a = 0.024$ mm, and $W_b = 0.006$ mm, in order that the reflection phase is zero at 60-GHz and the bandwidth of AMC is wide.

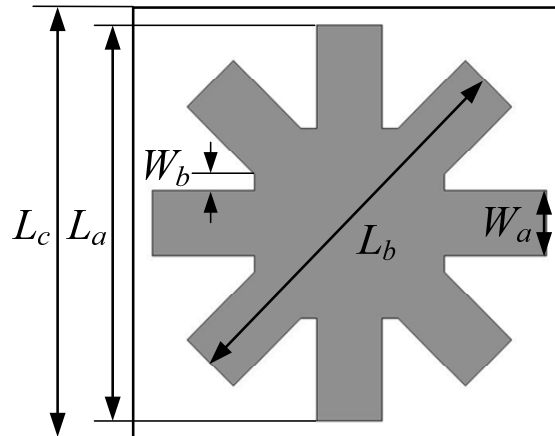


Figure 2-3 Geometry of proposed novel AMC cell structure

To accurately characterize the reflection phase of the incident wave on the AMC, the FEM-based 3-D full-wave EM solver, Ansoft HFSS, is used for the design simulation. The HFSS model to compute the reflection phase characteristics of the proposed AMC structure is shown in Fig.2-4. This model

is based on simulating scattering parameters of a single port air filled waveguide with two PECs and two PMCs walls. The propagating plane wave is polarized parallel to the PMC walls and normal to the PEC walls. The waveguide is then terminated to a single unit cell of the proposed AMC structure and the reflection phase is obtained by calculating the scattering parameter at the input of this single port waveguide. Compared with other conventional methods, this simple model is faster and more accurate.

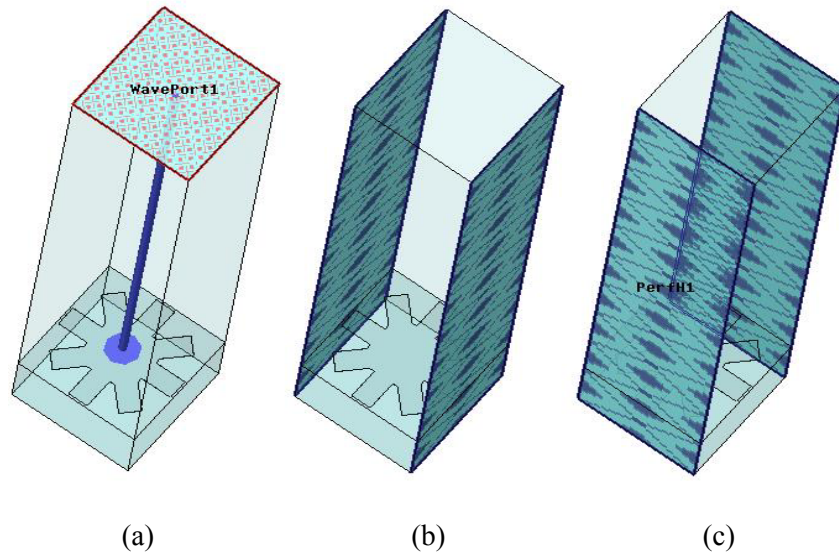


Figure 2-4 The HFSS simulation model for an AMC cell: (a) The geometry and the wave-port excitation. (b) Perfect-E and (c) perfect-H symmetry planes.

In AMC designs, the phase curve of the reflected field of a plane wave which is incident on an AMC surface is a very important characteristic. Obtaining this phase curve helps the designer to realize the AMC condition at or near a desired frequency, where the phase of the reflected wave should be close to 0° . Fig.2-5. shows the simulated reflection phase. The proposed AMC surface exhibits a reflection phase of 0° at 60 GHz. The frequency bandwidth of the HFSS optimized AMC is between 52.5 GHz and 67 GHz, at which the reflection phase is within $+90^\circ$ and -90° . Compared with previous AMC for 60-GHz radio, this bandwidth of 24% is larger. For the unlicensed 7 GHz working bandwidth, from 57 GHz to 64 GHz, the reflection phase is within $+54.5^\circ$ and -66.4° . The enhancement in bandwidth will be illustrated in the following section through parameter study.

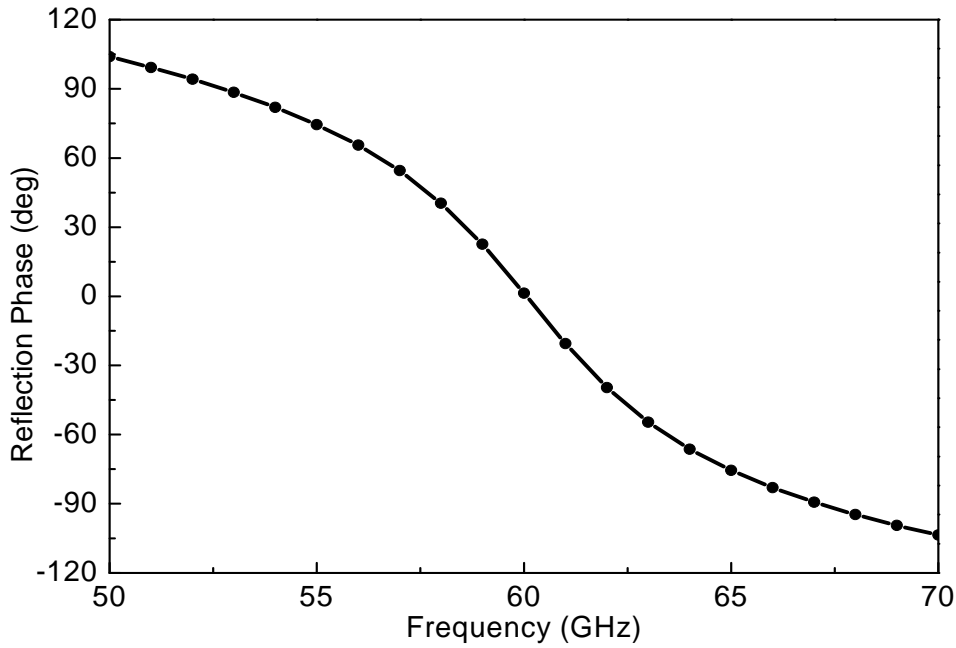


Figure 2-5 Simulated reflection phase of wave incident on AMC structure

2.2.2 Parameter Study

Among all the relevant parameters, the width d ($d=L_c-L_a$) between two adjacent AMC units and the width of metal strip W_a are the most crucial parameters in fixing an AMC structure, which affects the capacitance in the equivalent circuit and further determines the operation frequency of the proposed AMC structure. Simulated reflection phase of AMCs with different d and W_a are plotted in Fig.2-6 and Fig.2-7 respectively. With increasing width d between adjacent AMC units or increasing width W_a of metal strip of AMC unit, the AMC operation frequency would both decrease.

The adding of two diagonal metal strips brings some extra freedom, which would affect the slope of curves and thus affect the bandwidth of the AMC. By this way, the bandwidth of AMC can be adjusted and optimized. Fig.2-8 shows that the reflection phase bandwidths of AMC with L_b of 0.13 mm, 0.115 mm and 0.145 mm are 20%, 22.5% and 25% respectively.

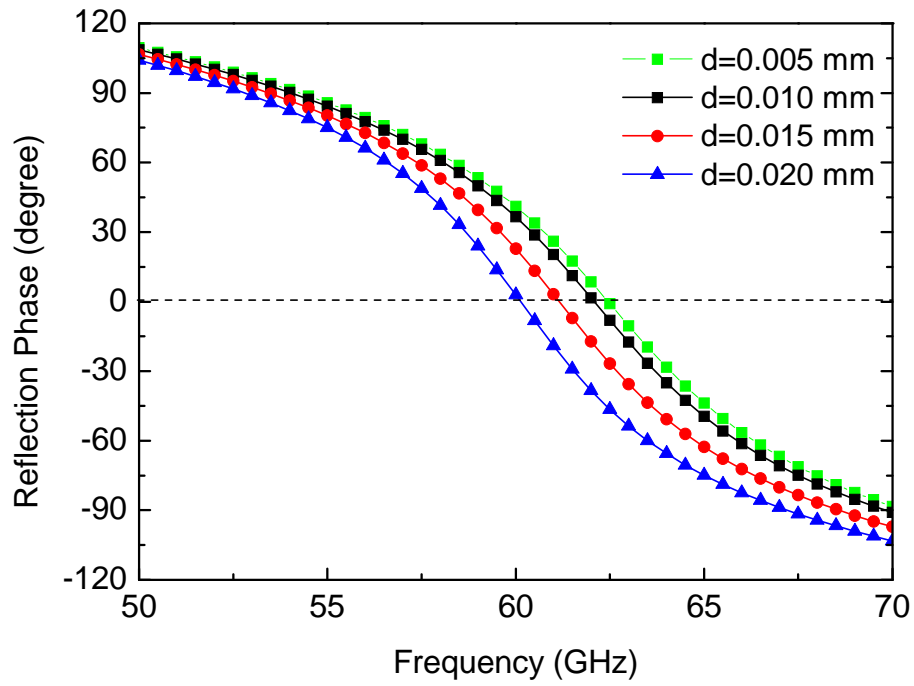


Figure 2-6 Reflection phase of AMCs with different d

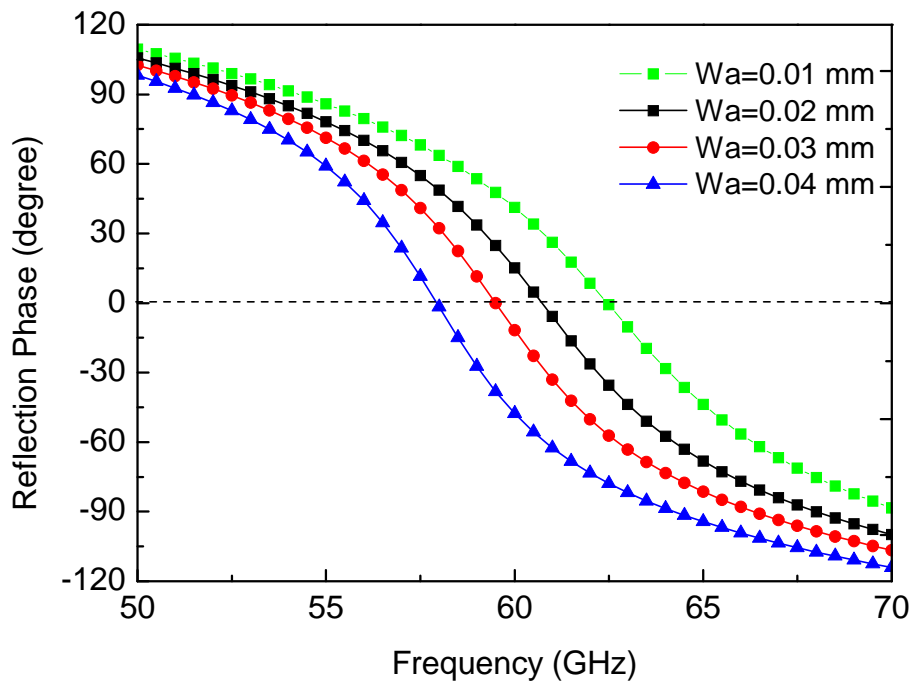


Figure 2-7 Reflection phase of AMCs with different Wa

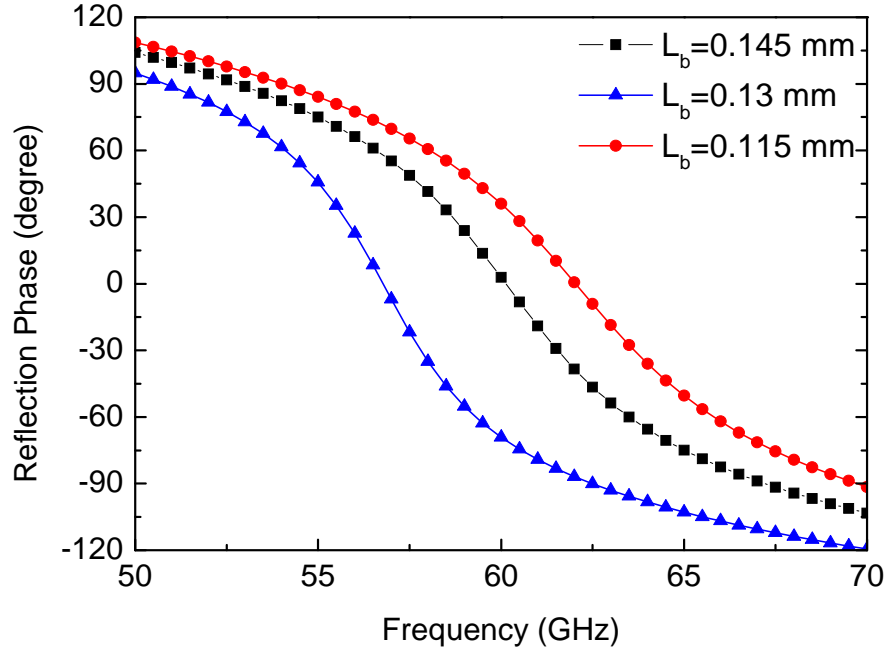


Figure 2-8 Reflection phase of AMCs with different L_b

2.3 AMC-Based Circularly Polarized on-Chip Loop Antenna Using CMOS Technology

2.3.1 Circularly Polarized Loop Antenna Design

In view of wireless access applications, the circularly polarized (CP) property is very desirable for 60-GHz antennas. For the commonly used linearly polarized (LP) antenna, we have to rotate the transmitting and receiving antenna properly for polarization matching, particularly in the case of the line-of-sight radio links. Using the CP antenna this problem can be mitigated while also allowing for reduction in interference from multi-path reflections. Some researchers have introduced 60-GHz CP antennas using LTCC technology and PCB fabrication process [74]-[77]. Though there is also a huge demand of CP antenna using CMOS technology for integrated chip applications, there are no CP antenna designs among the previous 60-GHz antennas using commercial CMOS technology. In this paper, we employ a circular open-loop antenna for the circular polarization property. An open-loop antenna has been studied for CP operation and a parasitic element was introduced for bandwidth enhancement in [78]. However, a coaxial feed

cannot be used because there is no vertical via for the conventional silicon process. As a result, we combined the CP loop antenna with coplanar waveguide (CPW) feed and integrated it with modified AMC plane for further CMOS fabrication and performance improvement.

Loop antennas are usually used as linearly polarized antennas. Research has found that a loop antenna can radiate circularly polarized waves if a gap is cut on the loop. The reason why this CP radiation can be produced is that the traveling wave current distribution gets excited along the open loop. Unfortunately the bandwidth of the CP loop antenna is much less than that achieved by spiral antennas. It is found that the axial ratio (AR) bandwidth of a CP loop antenna can be significantly increased by adding another loop inside the original loop [78]. The addition of this parasitic element can produce one more resonance that leads to a considerable enhancement for the AR bandwidth. Since the additional parasitic element is placed inside the original loop and there is no direct electrical connection to its surrounding, there is no significant increase in size and complexity of the antenna structure.

As shown in Fig. 2-9, the CP antenna consists of two open wire loops placed above the lossy silicon substrate, whose height is 300 μm . The outer loop, fed at $\Phi=0$ by a CPW feed, acts as a driven loop, while the inner loop acts as a parasitic element. A small gap is cut on each loop in order to radiate a CP wave. By adjusting the size of the parasitic loop and the positions of the two gaps, an optimal performance for the on-axis (in the z direction) axial ratio can be achieved. A CPW feed is employed here so that it can be easily connected to the ground-signal-ground (GSG) probe station for measurement. The width of the feed (l2) and distance (l3) between the feed and grounded rectangular pads are optimized to be 60 μm and 35 μm for 50 Ω matching, respectively. The configuration parameters are summarized in Table 2-1.

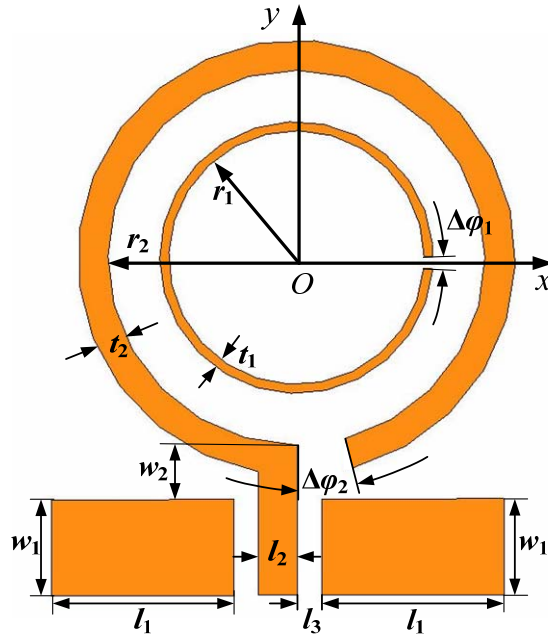


Figure 2-9 Geometry of the CP on-chip antenna

Table 2-1 Configuration Dimensions of on-Chip Antenna

Symbol	Value	Unit
r1	0.21	mm
r2	0.315	mm
t1	0.015	mm
t2	0.04	mm
$\Delta\phi_1$	5	degree
$\Delta\phi_2$	15	degree
w1	0.16	mm
w2	0.04	mm
l1	0.3	mm
l2	0.064	mm
l3	0.04	mm

Fig. 2-10 and Fig. 2-11 show the axial ratio and gain performance of the CP antennas with and without the parasitic inner loop, respectively. It is confirmed that adding a parasitic loop can introduce one more AR resonance. The axial ratio bandwidth has been increased from 10.8% to 23.5%, while the gain has been decreased by approximately 1.5 dBi for the coupling loss between two loops.

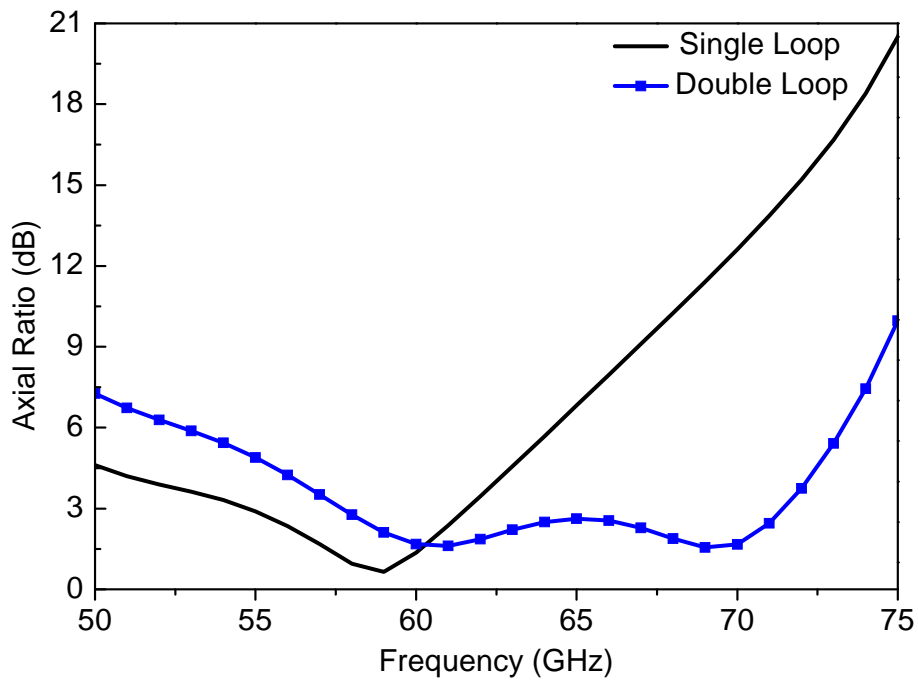


Figure 2-10 Simulated axial ratio of single loop and double loop CP antennas

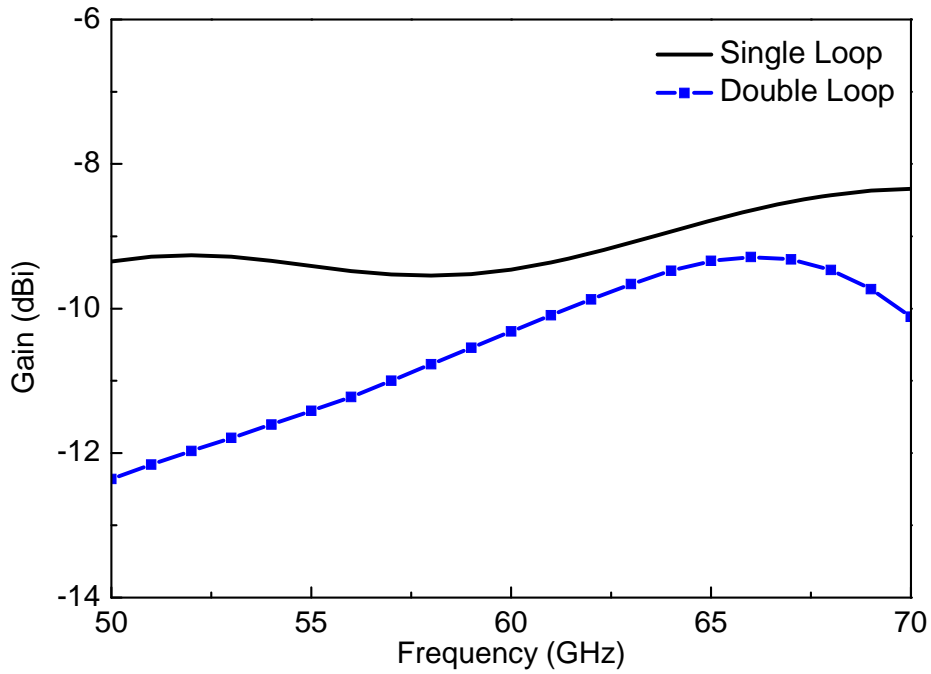


Figure 2-11 Simulated gain performance of single loop and double loop CP antennas

2.3.2 Integration of Modified AMC plane

Once the AMC structure is fixed, and the characteristics of the proposed CP antenna are investigated, the antenna is placed on the 12×12 units AMC plane and simulated as a compound antenna. Due to the fabrication limit, distance between the antenna on M6 layer and the AMC plane on M1 layer is only $4.5 \mu\text{m}$, even less than $\lambda/1000$. Therefore, the mutual coupling between the antenna and the AMC plane is extremely strong and affects antenna performances greatly. In order to reduce this mutual coupling, the 12×12 units AMC plane is modified by gradually removing the unit elements from the center region of the AMC plane underneath the loop antenna. Fig. 2-12 shows the axial ratio performance of the antenna combined with 4×4 AMC units removed blank plane, 6×7 AMC units removed blank plane and full AMC plane, respectively. On the other side, the AMC plane can make the reflected wave in phase with the incident wave, and therefore increase the gain performance. So we have to keep at least three column AMC units at most of the area. Taking the area limit of the fabrication, the reflection function of AMC plane, and axial ratio variation due to AMC plane, we optimized to achieve a trade-off of the modified AMC plane.

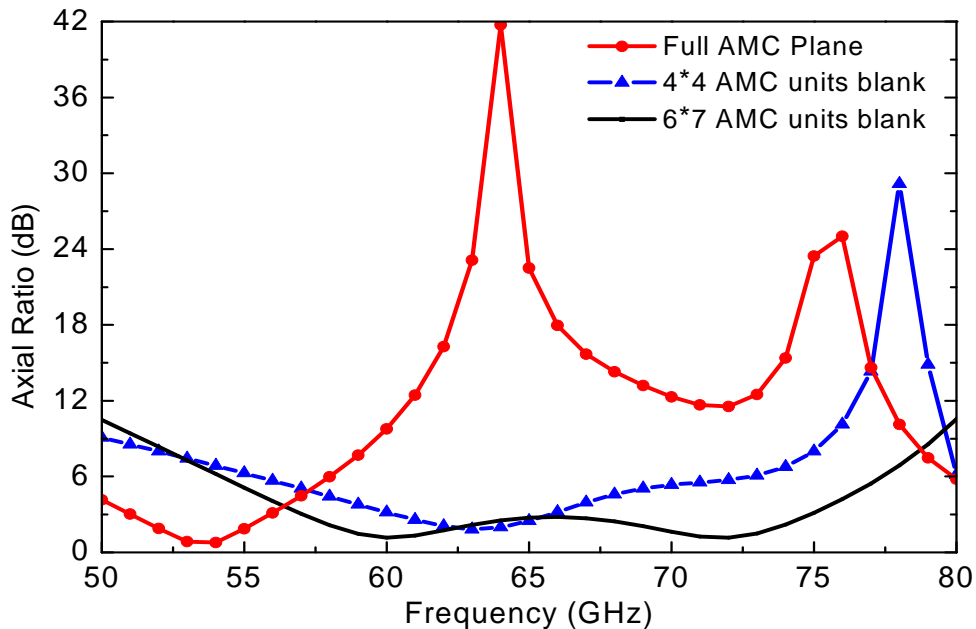


Figure 2-12 Axial ratio performance comparison of antennas integrated with different modified AMC planes

To further illustrate the function of the AMC in behaving like a PMC surface and then enhancing the antenna gain, we simulated the antenna with the solid PEC reflector with a rectangular opening in the middle region similar to the modified AMC layer. The results in Fig.2-13 proved that the gain of antenna with PEC reflector is much lower than that of antenna with modified AMC layer. Lastly, the antenna with the final modified AMC plane is demonstrated in Fig. 2-14.

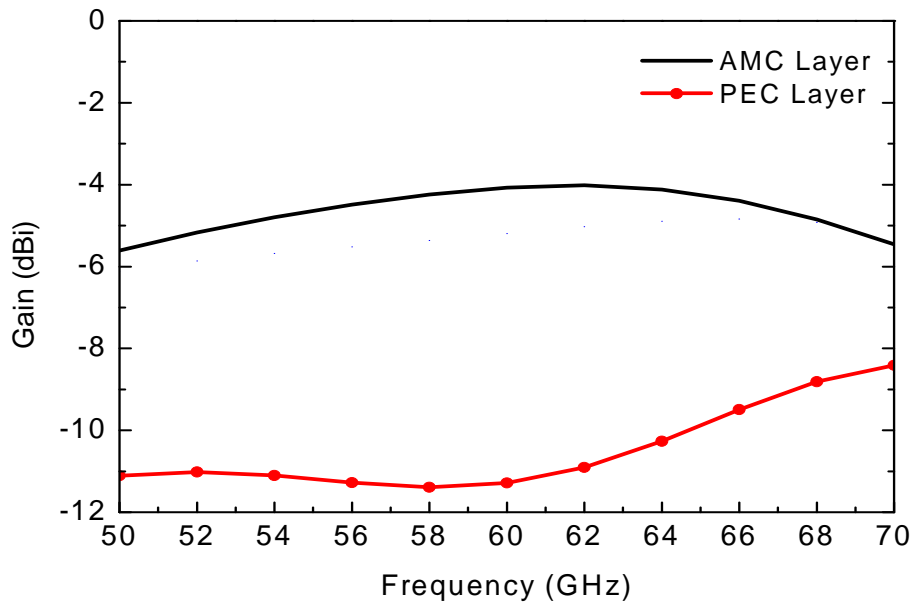


Figure 2-13 Comparison of antenna with PEC layer and modified AMC layer

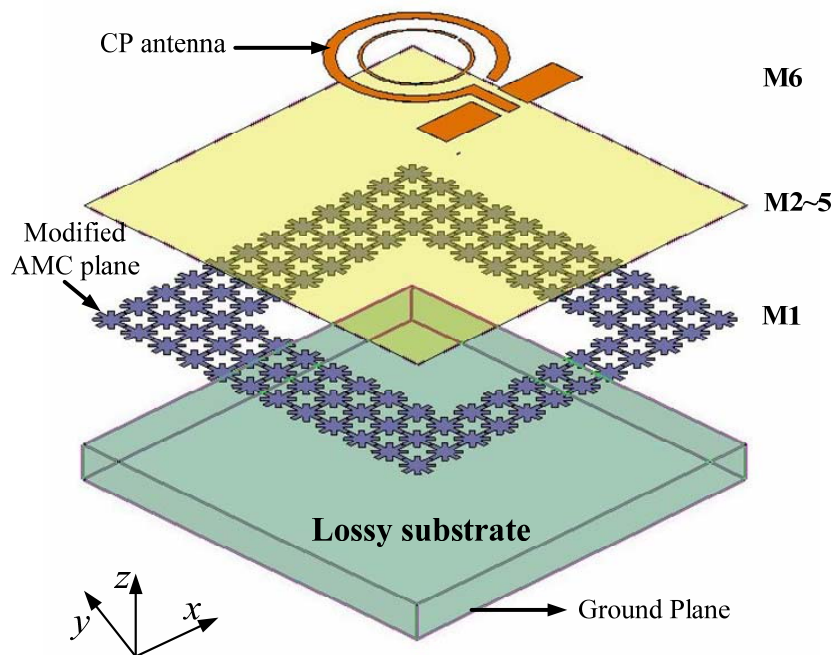


Figure 2-14 3D explored view of the proposed antenna with the modified AMC plane

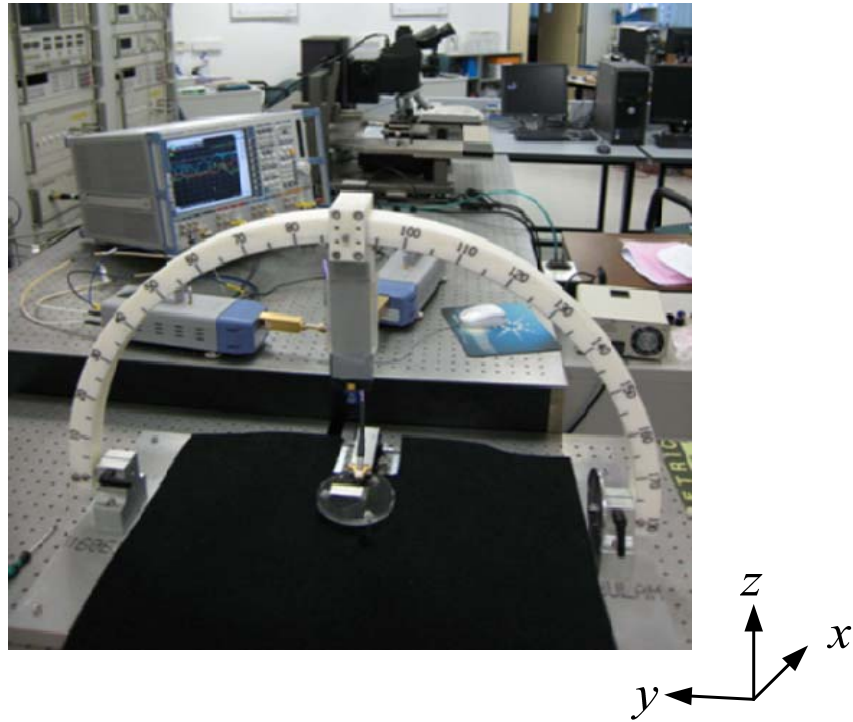
2.3.3 Measurement and Analysis

For the conventional PCB antennas, the radiation pattern and gain characteristics have been measured inside an anechoic chamber by employing transmit and receive towers. However, this method of measurement would become more difficult when applied to the mm-Wave antennas-on-chip. The reasons for this are as following:

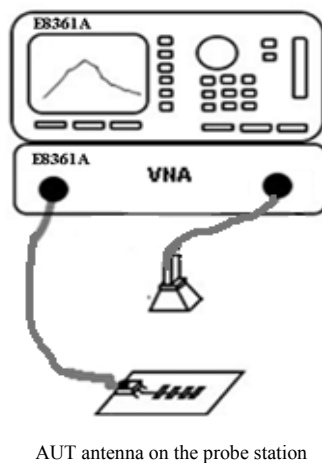
- 1) Different from the conventional coaxial or SMA feed setup, small wafer probes have been used to feed the on-chip antennas, with tips landing on bond pads. These probe tips are so fragile that they can break very easily whenever there is any tiny movement of the connected antenna. Extra transmission lines should be used to connect the physical feeding point on the antenna.
- 2) The measurement results may be affected, because the antenna under test (AUT) environment has been interfered by the adding of the probe-arm which steadily holds and connects the probes to the VNA. Besides that, the metallic probe station will behave like an extra ground plane of the antenna and thus bring in tolerance into the measurement results, too.
- 3) In order to connect those probes precisely onto the feeding points of the on-chip antenna, we have to use a microscope.

Our antenna was measured by Rohde & Schwarz vector network analyzer (VNA) ZVA75 up to 75 GHz. A GSG RF probe with a pitch of 100 μm was touched on the grounded coplanar waveguide (GCPW) line of the antenna for measurement. The antenna patterns were measured with the set up shown in Fig.2-15 (a). With the proper probe touching, the tested antenna senses the radiation in the boresight direction from a WR-15 standard pyramidal horn antenna. The horn antenna has an aperture size of $13 \times 10 \text{ mm}^2$ and a gain of 15 dBi. The far field region limit of the horn antenna can be calculated as $2D^2/\lambda = 10.8 \text{ cm}$, where D is the largest dimension of the horn and λ is the free space

wavelength. The distance between the horn aperture and the antenna under the test is set around 15 cm. Fig.2-16 exhibits a photograph of the fabricated prototype of this AMC-based CP antenna-on-chip using the CMOS technology, including one picture for the case attached on a conductor carrier for easy on-wafer measurement and one under a microscope.

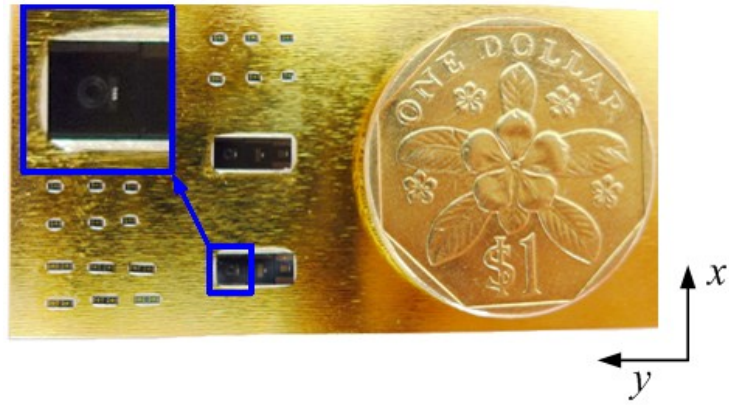


(a)

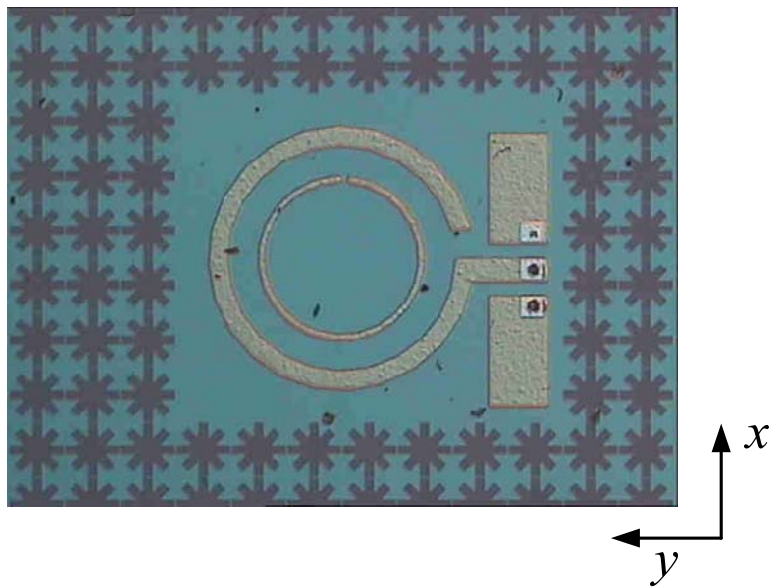


(b)

Figure 2-15 Antenna test set up: (a) pattern measurement and (b) polarization study. AUT: antenna under test



(a)

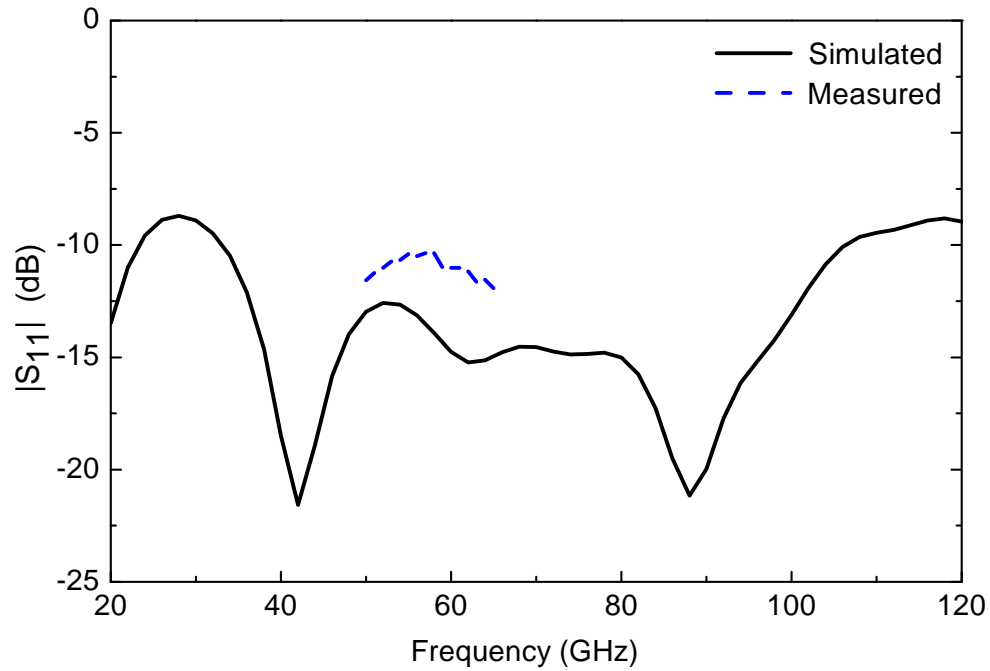


(b)

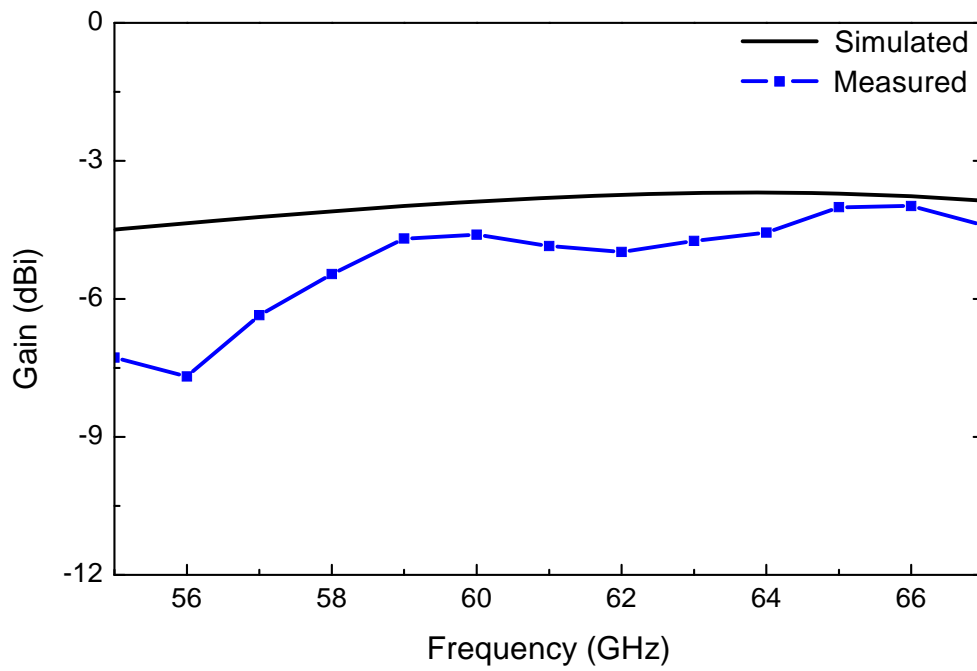
Figure 2-16 Photograph of the proposed CP on-chip antenna: (a) attached on a conductor carrier for easy measurement and (b) zoom in under a microscope

Fig.2-17 shows the simulated and measured results for the antenna. Fig.2-17 (a) shows that this proposed antenna can offer a wide impedance matching bandwidth from 34 GHz to 105 GHz for $|S_{11}|$ is less than -10 dB from the simulation. The measurement results from 55 to 65 GHz agreed with the simulation. From Fig. 2-17 (a), it is observed that the measured $|S_{11}|$ is approximately 2 dB worse than that from simulation, which could be caused by the measurement setup and the deviation of the silicon substrate characteristics setting in the simulation from its actual values. Fig. 2-17 (b)

shows simulated and measured peak gain values are at -3.7 dBi at 60 GHz and -4.4 dBi at 62 GHz, respectively. Fig. 2-17 (c) shows that the simulated axial ratio (AR < 3) bandwidth is approximately 30 %, from 56 GHz to 74 GHz. Gain and AR measurements agreed with the simulation for the frequency range from 57 GHz to 67 GHz.



(a)



(b)

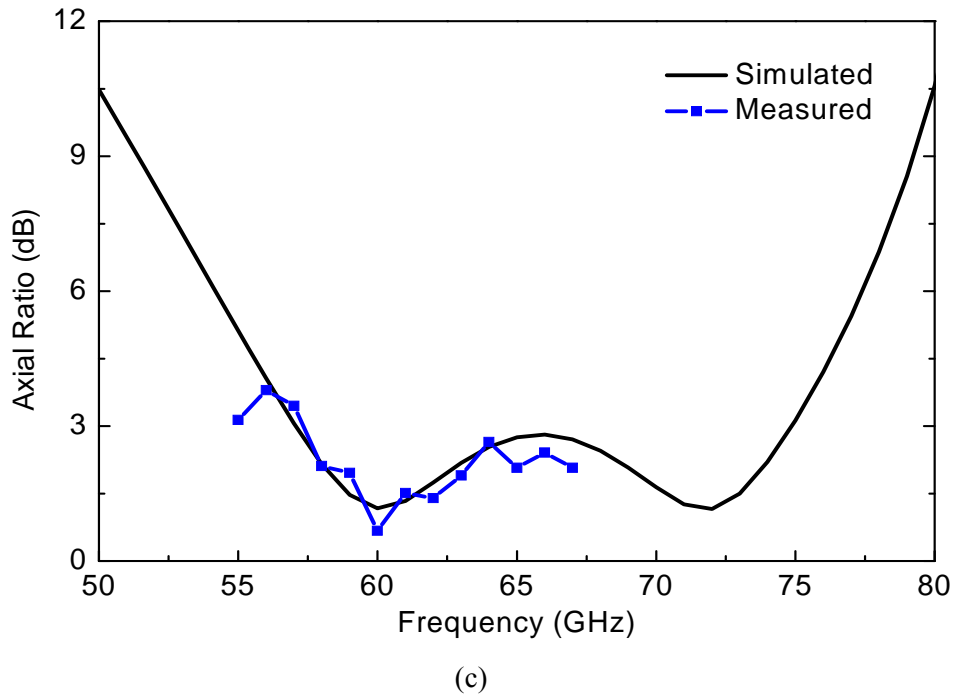
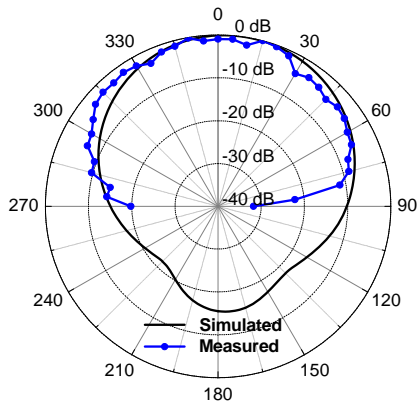
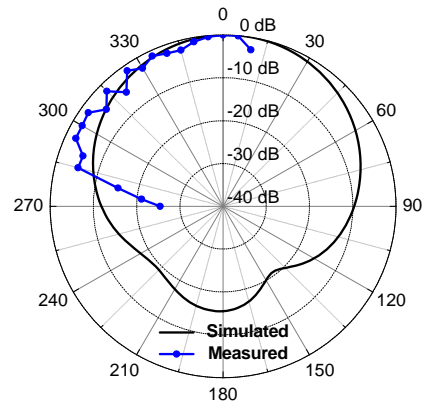


Figure 2-17 Measured and simulated performance of the proposed antenna: (a) return loss, (b) gain, (c) axial ratio

Finally, the antenna far-field radiation pattern is measured. The horn antenna is placed on top of the AUT. The apertures of the two antennas are both parallel to the xy -plane. The tests are then conducted with the horn at 0° position (E field of the horn is in y -direction) and 90° position (E field of the horn is in x -direction), respectively. If the measurement setup permits several pairs of orthogonal positions, the CP test can be more accurate [92]. Fig. 2-18 shows the measured radiation pattern in the upper half-plane at 57 GHz, 60 GHz, and 64 GHz, compared with the simulated radiation pattern of the proposed antenna. Good agreement is obtained between simulation and measurement for the gain, AR and radiation patterns.

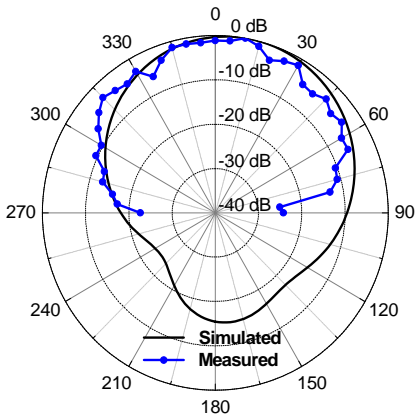


XOZ of 57 GHz

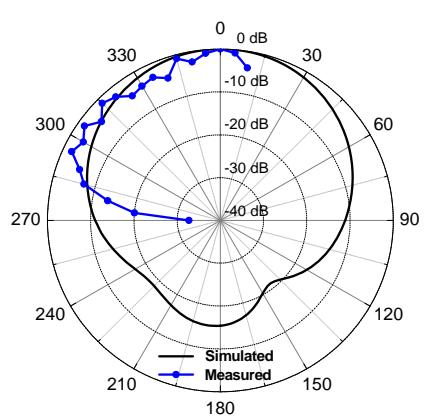


YOZ of 57 GHz

(a)

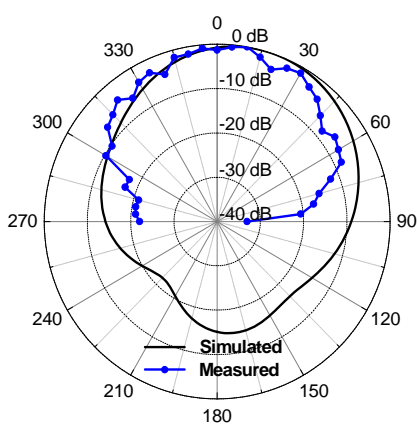


XOZ of 60 GHz

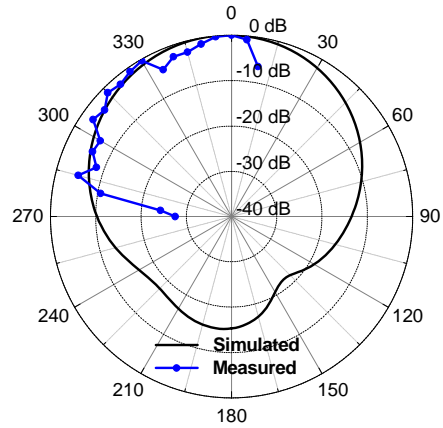


YOZ of 60 GHz

(b)



XOZ of 64 GHz



YOZ of 64 GHz

(c)

Figure 2-18 Measured and simulated XOZ-plane and YOZ-plane radiation patterns at (a) 57 GHz, (b) 60 GHz, (c) 64 GHz

Table 2-2 Comparison with Previously Reported 60-GHz CMOS Antenna Designs

Type of Antenna	Process Technology	Frequency	Gain	Polarization
Quasi-Yagi[20]	Post-back-end-of-line	65 GHz	-12.5 dBi (Measured)	Linearly Polarized
Invert-F[20]	Post-back-end-of-line	61 GHz	-19 dBi (Measured)	Linearly Polarized
Monopole[41]	0.13-um CMOS	60 GHz	-9.4 dBi (Measured)	Linearly Polarized
Yagi [40]	0.18-um CMOS	60 GHz	-10.6 dBi (Measured)	Linearly Polarized
Meander-line Invert-F [79]	0.18-um CMOS	60 GHz	-15.7 dBi (Measured)	Linearly Polarized
Slot [80]	0.09-um CMOS	60 GHz	-2.1 dBi (Simulated)	Linearly Polarized
Dipole [81]	No Fabrication	60 GHz	-7.3 dBi (Simulated)	Linearly Polarized
Yagi [81]	No Fabrication	60 GHz	-3.5 dBi (Simulated)	Linearly Polarized
Our work	0.18-um CMOS	60 GHz	-4.8 dBi (Measured)	Circularly Polarized

Table 2-2 shows the performance comparison between our work and those in reported articles [20], [40], [41], [79]. However, low gain is indeed a common problem of the CMOS on-chip antennas, because its lossy silicon substrate has a conductivity of 10s/m. Our proposed AMC-Based antenna-on-chip is considered to be partly acceptable compared with other conventional chip-level antennas in CMOS process. It can be seen from the table that the measured gain obtained is higher than the best measured gain reported previously, which indicates a significant gain improvement of the proposed antenna-on-chip with an AMC plane on the lossy substrate.

While antennas-on-chip have a common problem of low gain due to the substrate absorption, the integration of antennas on chip offers substantial cost reduction and flexibility in system design for commercial applications, since it removes all connections between circuits and antenna. As for practical applications, we would like to demonstrate the prospective applications in the following aspects:

Firstly, antenna-on-chip may be employed as receiver antenna in short-range (usually less than 1 meter) wireless communication systems, such as rapid upload/download, wireless display, wireless gaming, distribution of high definition TV, wireless file transfer. As discussed in ref [82], in a communication link, assuming that the gain of transmitter antenna and receiver antenna are G_T and G_R respectively, the link budget equation can be expressed as:

$$G_T + G_R = M + \frac{C}{N} + L_I + kT + 10 \log B + NF + PL + 10n \log d + X\sigma - P_t$$

where M is the link margin set to be 10 dB; C/N (the carrier-to-noise ratio) required for demodulation is 10.7 dB for QPSK, which is the minimum value for quasi-error-free reception by the $\frac{3}{4}$ coded OFDM system with guard interval $\frac{1}{4}$ in Rayleigh channels, L_I (the implementation loss of a transceiver) equals 6 dB, B is the bandwidth set as 2.16 GHz, NF (noise figure) considered as 7 dB, PL (the reference path loss) at $d=1m$ equals 68 dB, n the distance factor is 2, $X\sigma$ is 2 dB for a line of sight path in a typical indoor office and P_t (transmitted power) commonly obtains 10 dBm, which is even more than 12 dBm in ref [81]. Here in the calculation, we choose the P_t to be 10 dBm for a more general result. After instituting all the parameters above, the above equation can be simplified as:

$$G_T + G_R = 2 + \frac{C}{N} + 20 \log d$$

The combined antenna gains required for the line-of-sight path can be calculated from the simplified equation. For applications of the low gain antenna, we can take the case of QPSK with the data rate of 2 Gb/s at $d=1m$ for instance, the combined antenna gain required is 13 dBi. If the distance was even nearer, maybe 0.5m, the combined antenna gain requirement would only be 7 dBi. In these cases, our proposed antenna can have a possible application with the corporation of a well performed transceiver antenna. Moreover, with the development in improving the transmitter power, we can assume that antennas-on-chip will be suitable for more CMOS devices.

The employment of antenna-on-chip will be beneficial in highly integrated transceiver designs. In ref [80], an AMC-based wide-slot squared antenna has been integrated onto a 60-GHz OOK receiver using 90-nm CMOS process, whose simulated gain is -2.1 dBi.

Thereafter, antenna-on-chip may be considered to be a promising means of replacing metal interconnects between chips on a PCB, where metal leads become unusable at vast bandwidths and sub-terahertz carrier frequencies.

Ultimately, in further on-chip research, this proposed antenna could also be justified as an element that may be considered in an array, which would achieve higher gain for wider 60-GHz wireless applications.

2.4 Summary

A 60-GHz CP antenna-on-chip, which employs a modified AMC structure to increase the gain, has been designed using the conventional 0.18- μm CMOS process. The fabricated antenna including the modified AMC structure measures only $1.8 \times 1.8 \times 0.3 \text{mm}^3$. The antenna test was conducted to study antenna performance. The wide impedance matching bandwidth, the gain and the CP characteristics have been measured and the measurements confirm its good performance in prospective applications. The peak gain in the 60-GHz band is -4.4 dBi at 65GHz. The AR bandwidth is 30%, from 56GHz to 74GHz. The proposed antenna could be integrated into CMOS circuits for further application in the 60-GHz wireless personal area network. The AMC structure proved to be useful in enhancing antenna gain.

Chapter 3: Circularly Polarized Antennas-in-Package with Modified Soft-Surface Structure

3.1 Literature Review

In the view of wireless access applications, a circularly Polarized (CP) antenna array has been an interesting topic, since it can reduce the sensitivity to the antenna orientation and make an overall system resistant to multipath effects. In [84], and [85], CP antenna arrays have been employed in high speed wireless links at the 60-GHz band. Table 3-1 lists a comparison of several published 60-GHz CP antenna arrays. The challenge for antenna designs is in figuring how to cover the operating bandwidth of 7 GHz for both the return loss and the axial ratio.

Studies have been carried out on different methods to increase the CP bandwidth of an antenna array. Take [86] for an example, a 60 GHz 4×2 CP slot array loaded by ellipse strips achieves a bandwidth of 23% for the AR lower than 3 dB. As noted from the designs in [87]-[89], the sequentially rotated feed technique can be used to enhance the AR bandwidth. Sun *et al.* proposed a 4×4 CP microstrip patch antenna array in LTCC by applying a stripline sequential rotation feed network [90], which presents a wide impedance bandwidth, as well as a perfect axial ratio bandwidth, both over 8 GHz. Similarly with [90], a CP antenna array in [91] also employs the sequential rotation feed network to increase AR bandwidth, where a U-slot patch antenna to enhance the impedance matching bandwidth. In [92], a 60 GHz 4×4 SIW-fed CP antenna array in LTCC has the AR bandwidth widened by adopting a rotated strip because of the additional CP radiation from the strip. A metal-topped via fence has also been used to reduce mutual coupling between elements and thus improve the AR bandwidth. In [93], the flexible via holes distribution is employed to achieve a helical antenna array to obtain excellent CP performance.

Table 3-1 Comparison of 60 GHz CP Antenna Arrays

Architecture of Antenna Array	Impedance Bandwidth Sim. /Mea.(<-10 dB)	AR Bandwidth Sim. /Mea.	Peak Gain (dBi) Sim. /Mea.
Circular Slot 2×4 (LCP) [86]	22.5% / 24.2%	23% / 21%	15.9 / 15.6
Aperture Coupled Patch 4×4 (LTCC) [90]	19% / 11.5%	8% / $>8\%$	16.2 / NA
U-Slot Patch 4×4 (LTCC) [91]	28% / $>16.5\%$	16.6% / 11.5%	16.4 / 16
Helical Antenna 4×4 (LTCC) [93]	14% / 13%	14% / 12%	15 / 15.2

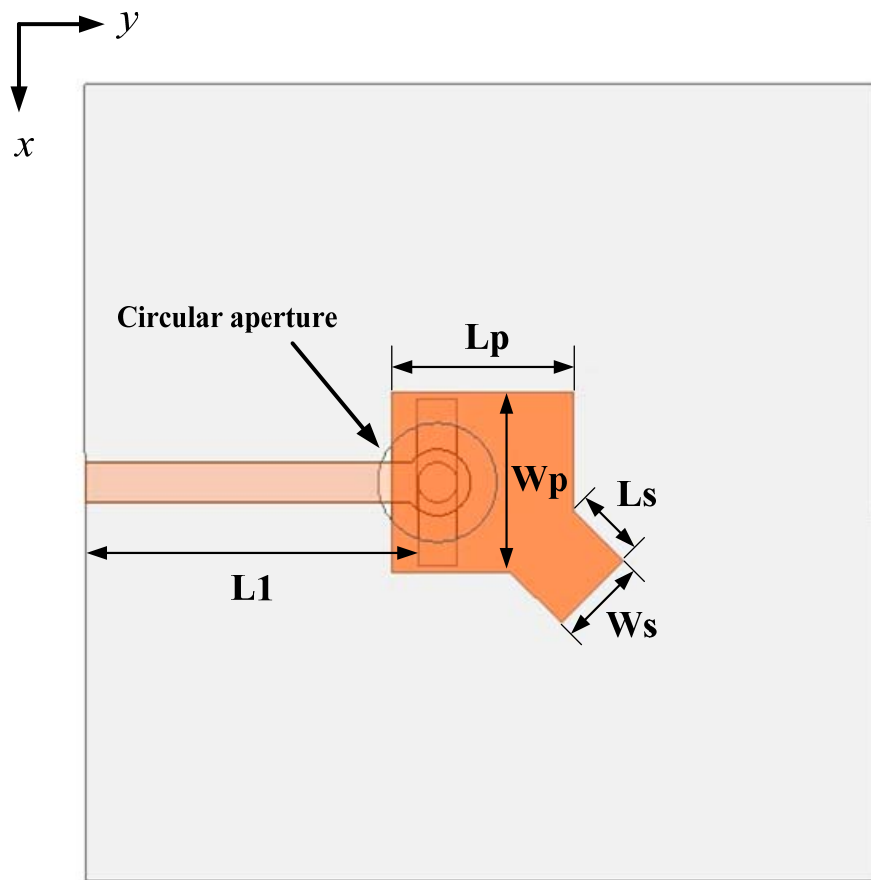
3.2 Circularly Polarized T-probe Fed Antennas

3.2.1 Circularly Polarized T-probe Stubbed Patch Antenna

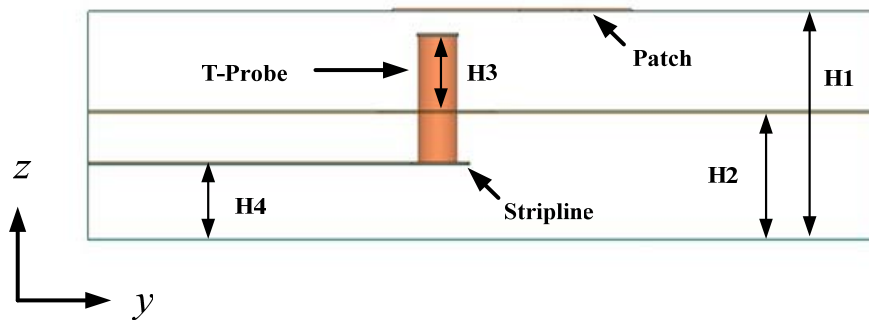
Due to its light weight, conformability and low cost, the patch antenna is one of the most popular antenna configurations in various applications. However, the conventional patch antenna suffers from narrow bandwidth. Among the several popular feeding techniques, aperture coupled feed and L- and T-probe fed thick patch antennas can effectively increase their impedance bandwidth. Here in this section, we employ the T-probe fed structure to form a CP patch antenna element.

The geometry of the single T-probe fed patch antenna element is shown in Fig.3-1. The multilayer LTCC substrate used is Ferro A6-M with dielectric permittivity $\epsilon_r = 5.9$ and loss tangent $\tan\delta = 0.001$. A fired tape thickness is 0.1mm for each layer, while the conductor thickness is 0.01mm. The T-probe consists of a vertical via and a $0.63\text{mm} \times 0.15\text{mm}$ horizontal microstrip line. The proposed antenna element is fed by a stripline to suppress the radiation

from the feeding line. A stub is added to the upper-right corner of the patch to excite two orthogonal modes for CP radiation.



(a)



(b)

Figure 3-1 Geometry of stubbed patch antenna: (a) top view; (b) side view

Table 3-2 Configuration Dimensions of T-probe Patch antenna

Symbol	Value (mm)	symbol	Value (mm)
Lp	0.68	H1	0.9
Wp	0.68	H2	0.5
Ls	0.33	H3	0.3
Ws	0.28	H4	0.3
L1	1.25		

Since the antenna performance deals with the parameters of the patch, T-probe, feed position and substrate thickness, optimization has been processed through the FEM-based 3-D full-wave EM solver, Ansoft HFSS, to present the final design. The detailed dimensions are presented in Table 3-2. The total design contains 9 LTCC layers (0.9mm), including 5 layers as the stripline feeding part and the other 4 layers as the antenna radiating part. Due to the limitations of the LTCC fabrication process, the width w_f of the feed stripline is 0.15 mm, representing a characteristic impedance of 50 Ω . The diameter of the via is also 0.15 mm.

Figs. 3-2 ~ 3-5 exhibit the simulated impedance bandwidth, gain, axial ratio and 3-D radiation pattern of the T-probe stubbed patch antenna. It can be seen that the impedance bandwidth is 30% with $|S_{11}| < -10$ dB between 49 GHz to 67 GHz, while the AR bandwidth is 6.33% with $AR < 3$ dB between 58.2 GHz to 62 GHz, which is within the impedance bandwidth. The simulated peak gain attains 6.02 dBi at 60 GHz. This proposed array element is left-hand circularly polarized (LHCP), and it can be easily adjusted to right-hand circularly polarized (RHCP) operation by changing the stub of the patch to the bottom-right corner.

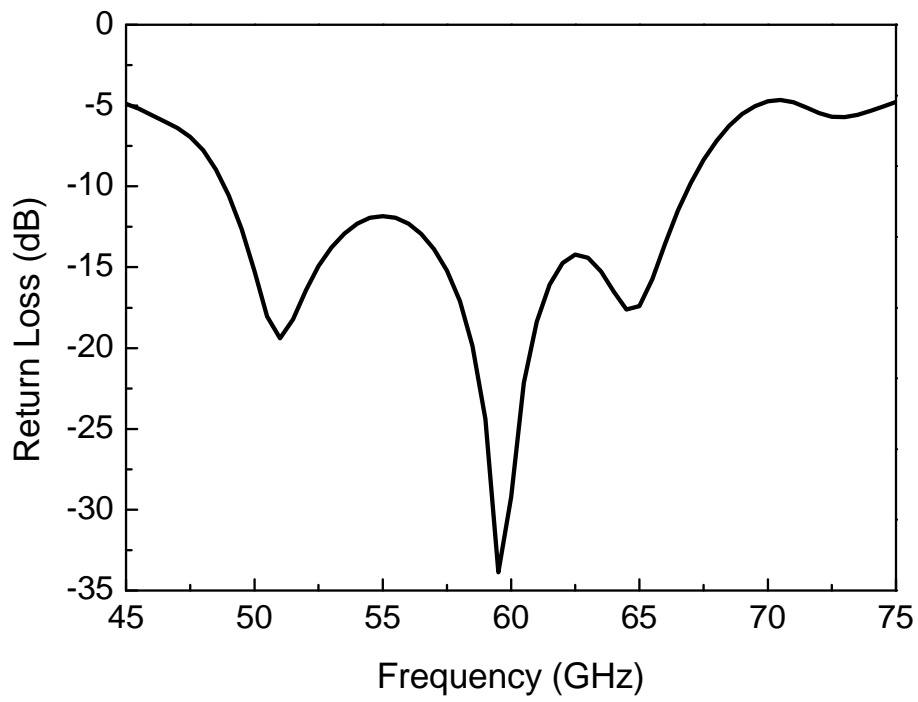


Figure 3-2 Simulated return loss of stubbed patch antenna

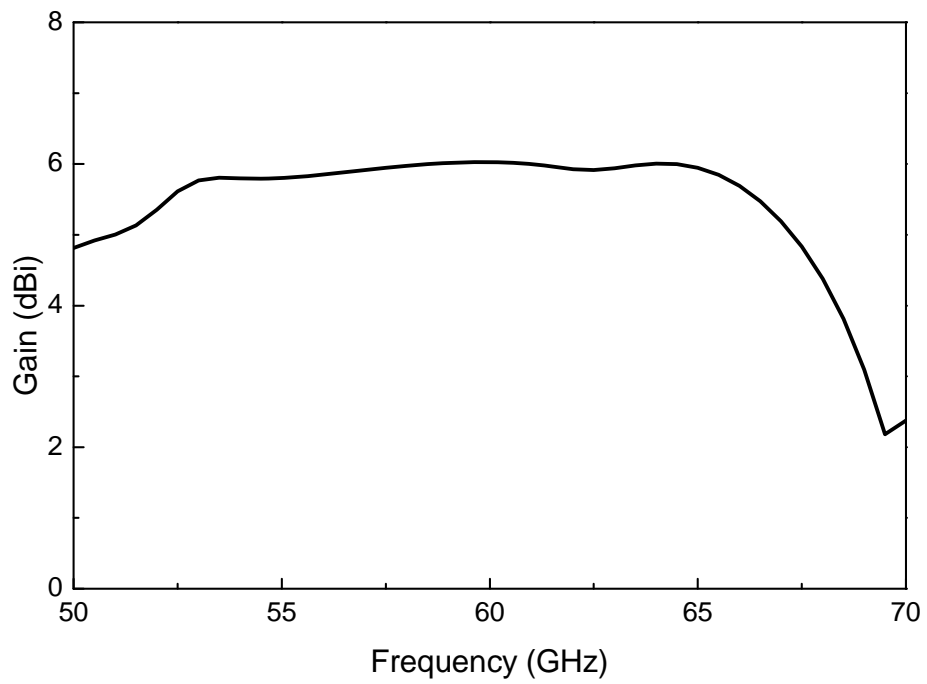


Figure 3-3 Simulated gain performance of stubbed patch antenna

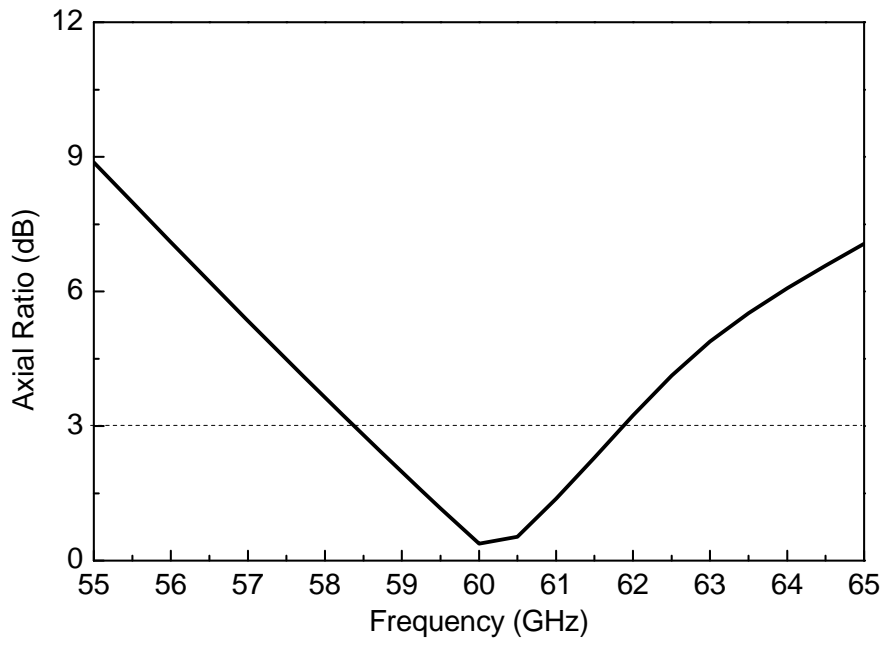


Figure 3-4 Simulated axial ratio of stubbed patch antenna

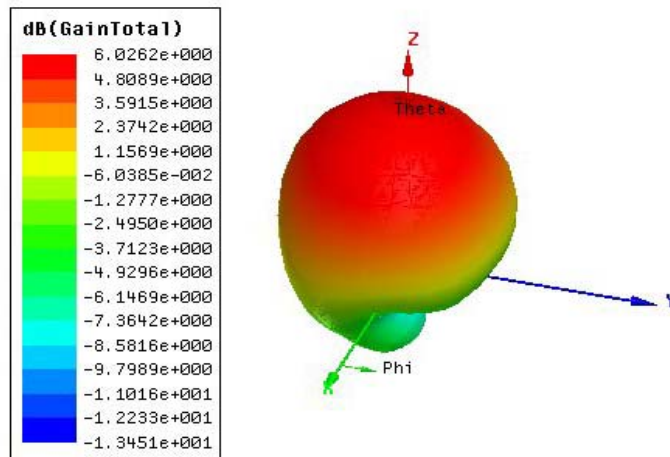


Figure 3-5 3-D radiation pattern at 60 GHz

3.2.2 Circularly Polarized T-probe Slot Patch Antenna

The configuration of a T-probe CP slot antenna is shown in Fig 3-6. A $0.76\text{mm} \times 0.76\text{mm}$ patch metal is printed on the top of the 9 LTCC layers. The T-probe feed structure consists of a $0.51\text{mm} \times 0.15\text{mm}$ horizontal strip placed on the second layer below the patch layer and a vertical via conductor (0.15mm diameter). Same as the former CP patch antenna, the total design contains 9 LTCC layers (0.9mm), including 5 layers as the stripline feeding part and the other 4 layers as the antenna radiating part. Because of the limitation in LTCC fabrication, the width w_f of the feed stripline is 0.15 mm, representing a characteristic impedance of 50Ω .

To obtain the circular polarization, the bottom-left and upper- right corners are cut off, while a 45° slot is etched in the middle of the radiating patch. The parameters of the slot antenna, T-probe, feed position and substrate thickness have been optimized in the FEM-based 3-D full-wave EM solver, Ansoft HFSS, to achieve good performance. Table 3-3 describes the detailed dimensions of this T-probe slot patch antenna. During the optimization, it is found that the dimensions and location of the horizontal strip are crucial for the impedance matching performance. The CP character is sensitive to the length and the shape of the slot.

Table 3-3 Configuration Dimensions of T-probe Slot Antenna

Symbol	Value (mm)	symbol	Value (mm)
Lp	0.76	H1	0.9
Wp	0.76	H2	0.5
Ls	0.25	H3	0.3
Ws	0.39	H4	0.3
L1	1.125	Wc	0.27

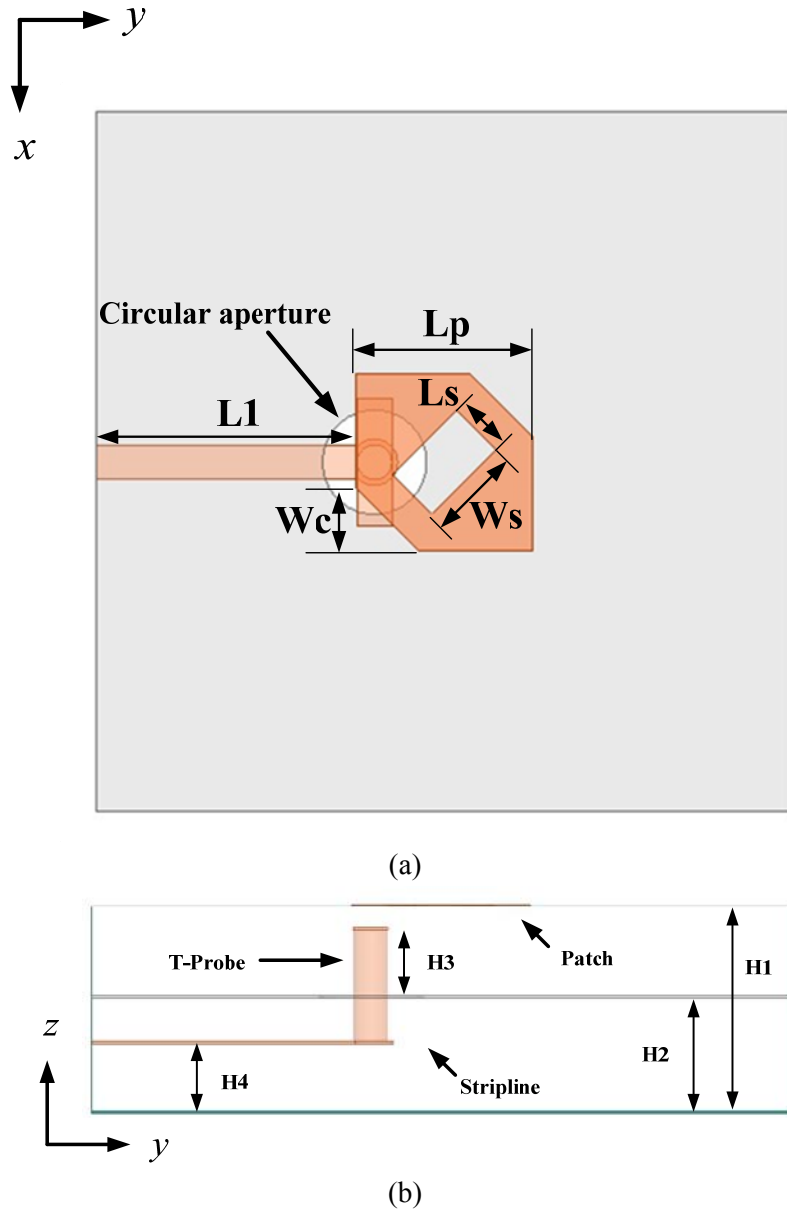


Figure 3-6 Geometry of stubbed patch antenna: (a) top view; (b) side view

The following Fig. 3-7 describes how gain performance varies with the frequency, and we can see that the 3-dB gain bandwidth is quite wide. During the working frequency bandwidth from 57 GHz to 66 GHz, the gain remains above 6 dBi and is flat, from 6 dBi to 6.3 dBi. This kind of stable and high performance gain would be quite useful in practical applications. The matching impedance bandwidth shown in Fig. 3-8 is wide due to the character of T-probe antenna, from 50 GHz to 70 GHz, approximately 33%. As shown in Fig. 3-9, the CP bandwidth covers 3 GHz, from 57.5 GHz to 61.2 GHz. Fig. 3-10 presents the 3-D radiation pattern of the proposed antenna at 60 GHz.

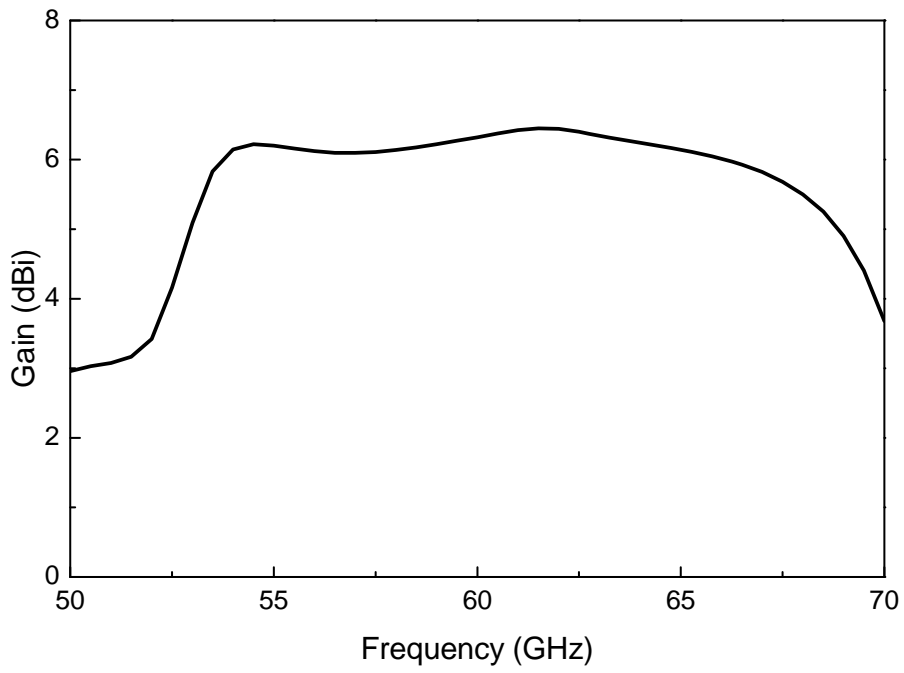


Figure 3-7 Simulated gain performance of slot patch antenna

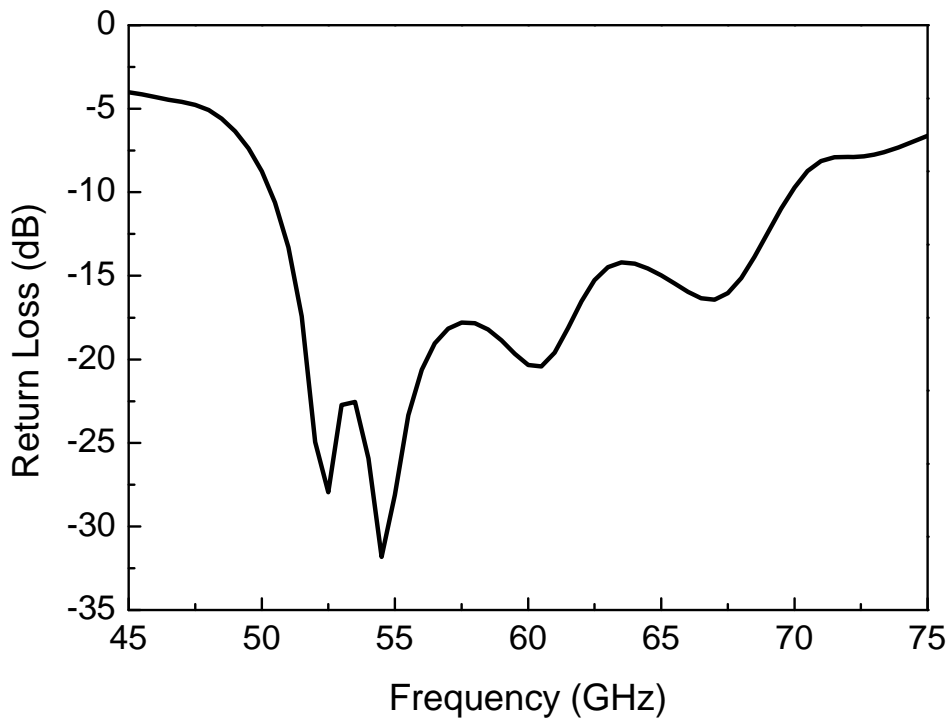


Figure 3-8 Simulated return loss of slot patch antenna

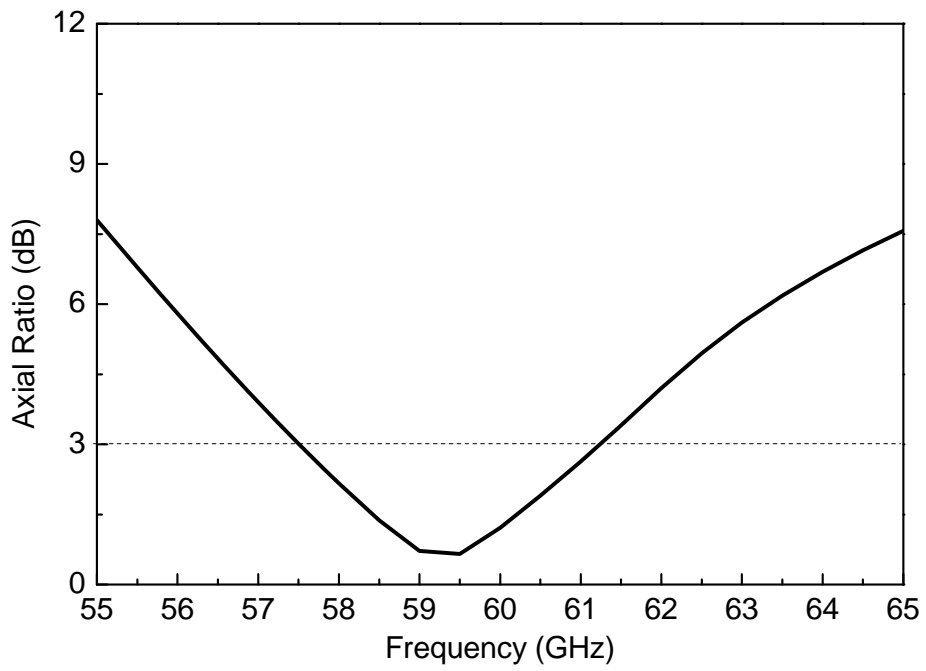


Figure 3-9 Simulated axial ratio of slot patch antenna

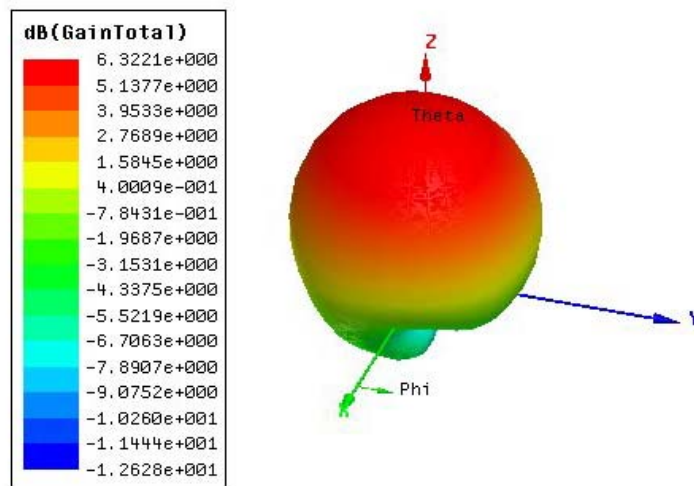


Figure 3-10 3-D radiation pattern at 60 GHz

3.3 Soft-Surface Structure

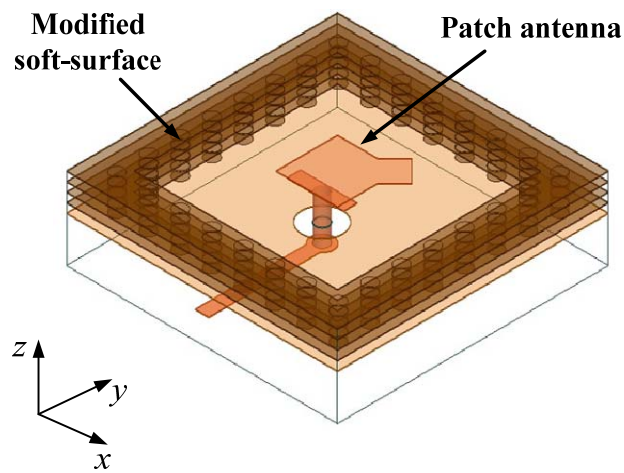
3.3.1 Literature Review

The soft and hard surfaces are defined from the boundary conditions of the E-field by analogy with soft and hard surfaces in acoustics. For antenna designs, the concept of soft and hard surfaces is a practical design tool. The hard-surface will support waves with a maximum value of the E-field at the surface, whereas the soft-surface makes the amplitude of the E-field zero at the surface. The well known soft surface structure, which is realized by corrugations, has been connected with horn antennas. These corrugated horn antennas, which are also called hybrid mode horns, have been existed for several decades [94], [95]. These horns are widely employed as feeds in dual-reflector antennas. The structure of corrugations has also been utilized to prevent the electric current on a conductor from floating in certain directions.

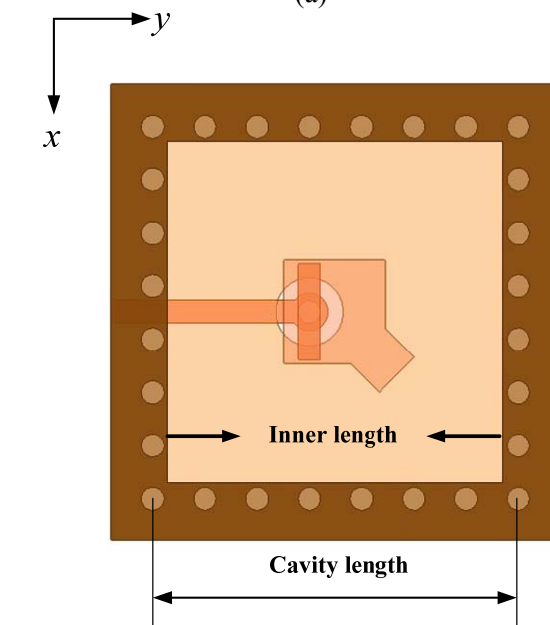
To some degree, the soft-surface can be analyzed similarly with the EBG structure. Both of them are capable to suppress surface wave propagation in a dielectric slab. Classical corrugations can transform the zero impedance from the bottom metal to the high impedance at the surface with the quarter wavelength depth. Compared to conventional EBG structures, some planar soft-surface structures have a smaller unit size, on the order of their resonant frequency. The reason for this reduction is that the soft-surface makes use of strips, while EBG employs patch. In previous studies, several papers have combined soft-surface with antenna designs to improve the overall performance. For example, a planar soft-surface structure has been utilized to reduce radiation backwards and therefore increase the antenna efficiency [96]. A non-planar structure has also been presented in [97] with the same goal. Moreover, a comparison between corrugations and EBG in reducing the radar mutual coupling has been made in [98]. Similarly in [99], a soft-surface structure has been proven to be better than the EBG structure in mutual coupling reduction, for the reason that the soft-surface can decrease both vertical and horizontal polarizations. Later in this section, detailed analysis will be provided to demonstrate soft-surface's function in the reduction of mutual coupling between patch antennas.

3.3.2 Structure of Modified Soft-Surface

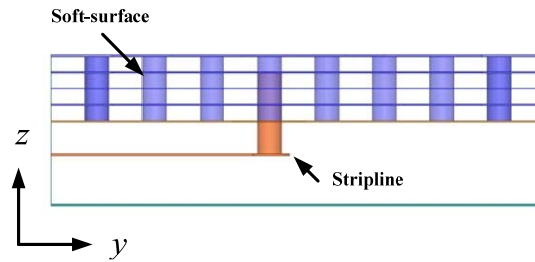
Taking the advantages of multilayer and via structures in LTCC, a modified soft-surface structure consisting of four layers of metal square rings and four sides of via walls short-circuited to the ground plane is proposed in this thesis. This novel soft-surface structure retains a compact size around the patch antenna and improves the antenna gain performance greatly. The 3-D bird view, top view and side view of the geometry for this stubbed patch antenna combined with a modified soft-surface structure are shown respectively in Fig 3-11 (a), (b), (c) . The diameter of vias remains as 0.15 mm, and the distance between two adjacent vias is 0.375mm.



(a)



(b)



(c)

Figure 3-11 Geometry for patch antenna with a modified soft-surface structure:

(a) 3-D bird view; (b) top view and (c) side view

3.3.3 Soft-Surface Structure around Antenna Element

This modified soft-surface can effectively suppress the outward propagation of surface wave around the antenna. The cavity formed by these four sides of vias as side walls is a useful isolation cavity to improve the antenna gain and to reduce the radiation backwards. The size of this cavity determines the operating frequency where peak gain appears. This is because the modified soft-surface structure is also a resonant structure as well as the antenna. Fig. 3-12 presents the 3-D radiation pattern of the stubbed patch antenna with the modified soft-surface structure at 60 GHz. It can be observed that gain performance at 60 GHz has been improved by about 0.65 dBi. This improvement mainly results from the increase of antenna directivity. Antenna efficiency remains almost the same since there is no significant change in the antenna structure. The difference of return loss between antenna with and without the soft-surface structure is not significant to some degree, indicating that the soft-surface does not affect impedance performance very much.

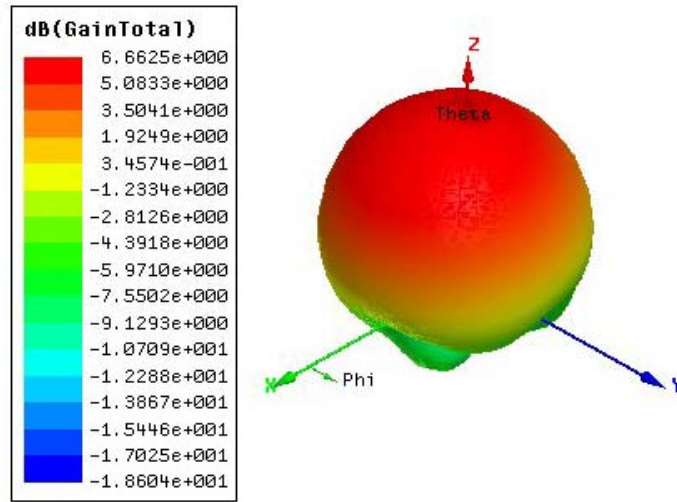


Figure 3-12 3-D radiation pattern at 60 GHz

There exists decrease in the field magnitude outside compared with that without soft-surface structure. That is because the shorted metal strips are approximately a quarter wave length from the radiation edge of the patch antenna. It equivalently acts as an open circuit for the TM mode, which is the main operating mode for patch antennas. The surface current on the inner edge of the metal ring thus cannot flow outwards. Besides the explanation of the surface current, the adding of soft-surface ring effectively increased the radiation aperture size. The fringing field along the inner edge of the soft-surface structure contributes to the radiation pattern improvement, which in fact forms an antenna array with the radiating edges of the patch antenna. Though the magnitude of this fringing field is much lower than the patch antenna, the size of the soft-surface is much larger than the patch. In general, the function of this fringing field in radiation enhancement is probably significant.

During the optimizations, we also found that the inner length of the soft-surface structure affected gain performance greatly, because of the complicated coupling between the soft-surface metal ring and the patch antenna. Fig. 3-13 illustrates comparison of the gain performances with different inner lengths of the soft-surface, while the comparison of axial ratio

performance has been presented in Fig. 3-14. Since the antenna with soft-surface structure will be used to group an array later in next section, we also have to take the distance of two adjacent antenna elements into account, which restricts the large size of inner length. By carefully considering these two factors, an inner length of 2.25mm has been chosen.

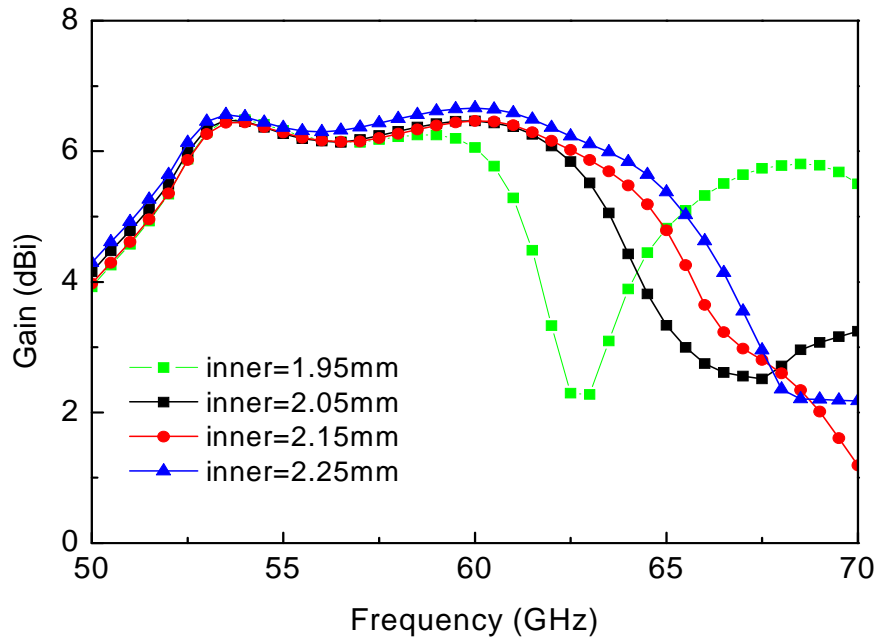


Figure 3-13 Comparison of the gain performances with different inner lengths of the soft-surface

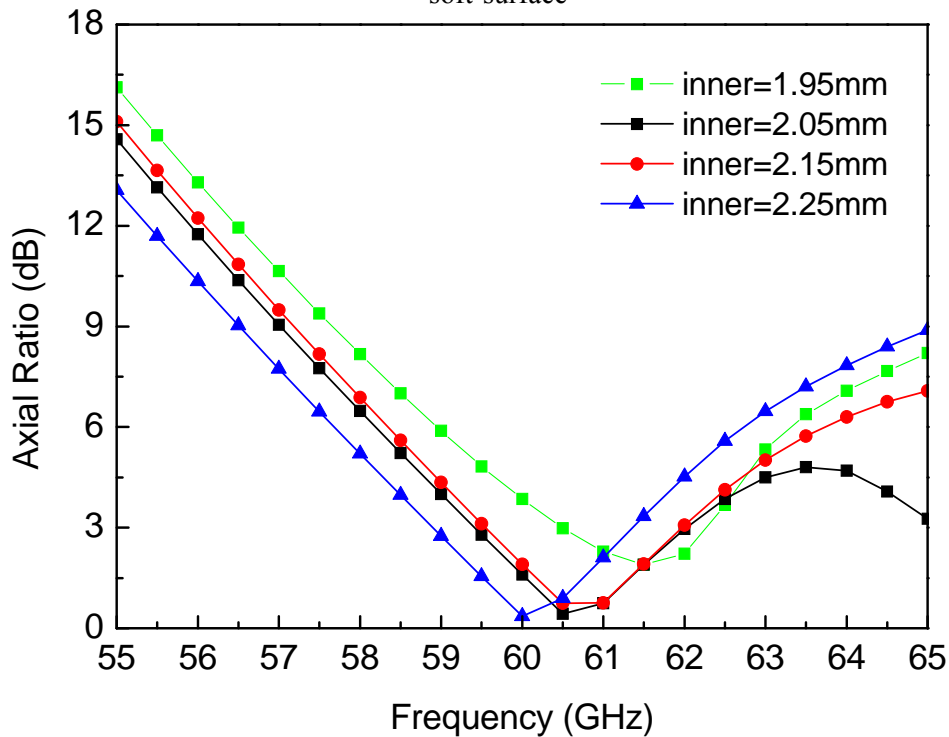


Figure 3-14 Comparison of axial ratio performances with different inner lengths of the soft-surface

3.3.4 Reduction of Mutual Coupling

In designing antenna arrays, mutual coupling is very crucial to the overall performance, which is mainly caused by surface wave between adjacent antenna elements. We first examine the mutual coupling between two patch antennas without the soft-surface structure. Fig. 3-15 presents the array configuration of two proposed patch antennas separated at a distance S .



Figure 3-15 Array configuration of two adjacent stubbed patch antennas

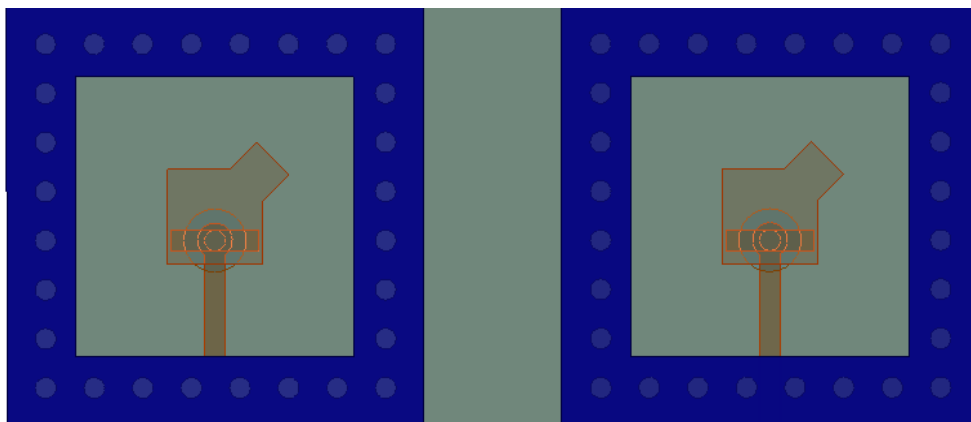


Figure 3-16 Array configuration of two adjacent stubbed patch antennas with soft-surface structure

After introducing the soft-surface structure around the antenna elements, the configuration is shown as follows in Fig. 3-16. We can see that between these two patch antennas, two rows of vias are inserted to block the surface waves. Comparison of the mutual coupling with and without soft-surface structure have been made and presented in Fig. 3-17. The isolation between the two adjacent elements is improved using the soft-surface structure.

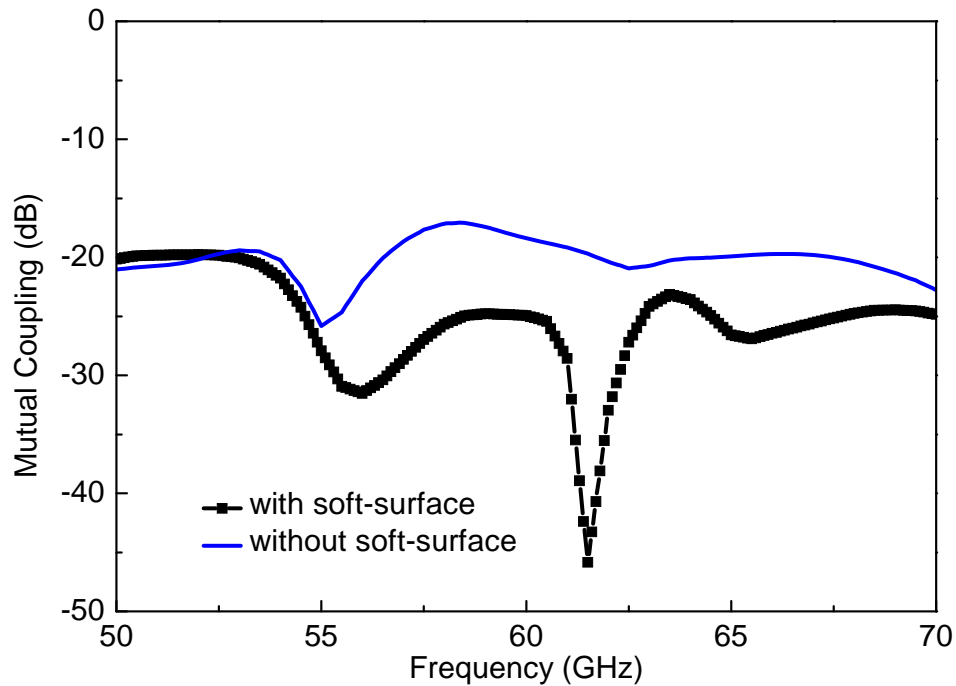


Figure 3-17 Comparison of the mutual coupling with and without soft-surface structure

3.4 Circularly Polarized T-probe Patch Antenna Arrays with Soft-Surface in LTCC

3.4.1 Antenna Array and Transition

Fig. 3-18 shows the geometry of the 4×4 T-probe patch antenna array. The distance between adjacent antennas is 3.3 mm and the size of the entire antenna array package is $15 \times 17 \times 0.9 \text{ mm}^3$. In order to enhance the CP bandwidth, each antenna element is rotated in respect to its adjacent element. A stripline sequential rotation feeding network is utilized to provide each patch antenna with equal amplitude but different phase with respect to their rotation angles. An extension of quarter guided wavelength in the strip line, meaning a delay of 90° in phase, realizes the phase difference in the feeding network.

Since the stripline fed antenna array cannot be tested directly, a GCPW to stripline transition has to be used for the probe station measurement, which is presented in Fig. 3-19. The ground planes are all connected by vias while the

GCPW is connected to the strip line by a signal via. After optimization, Fig. 3-20 shows simulated $|S_{11}| < -18$ dB and $|S_{21}| > -0.3$ dB from 50 to 70 GHz.

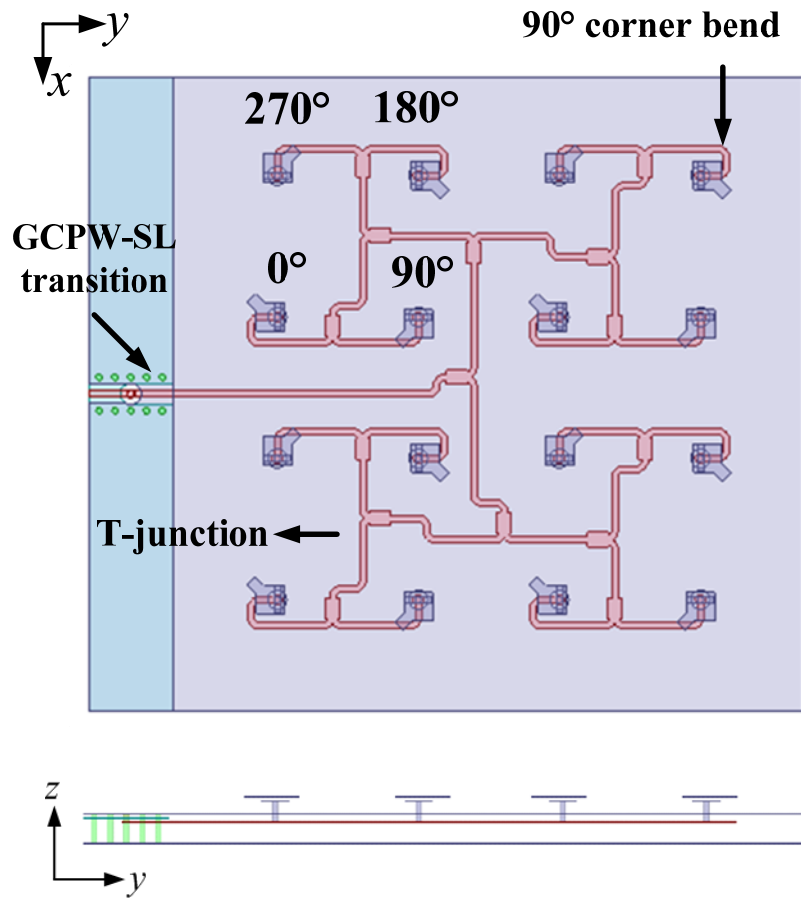


Figure 3-18 Geometry of the 4×4 T-probe stubbed patch antenna array

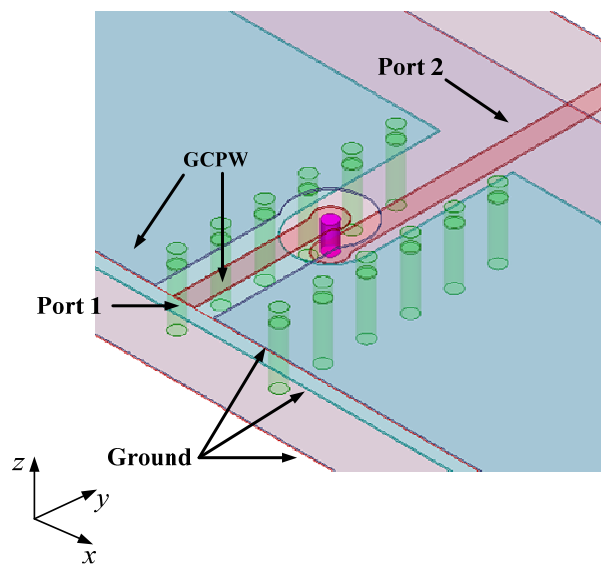


Figure 3-19 Structure of the GCPW structure

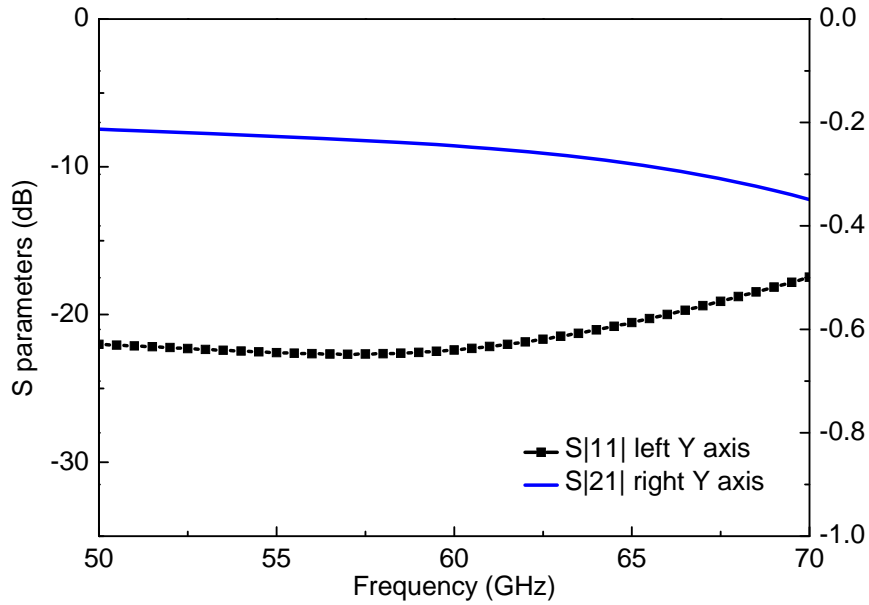
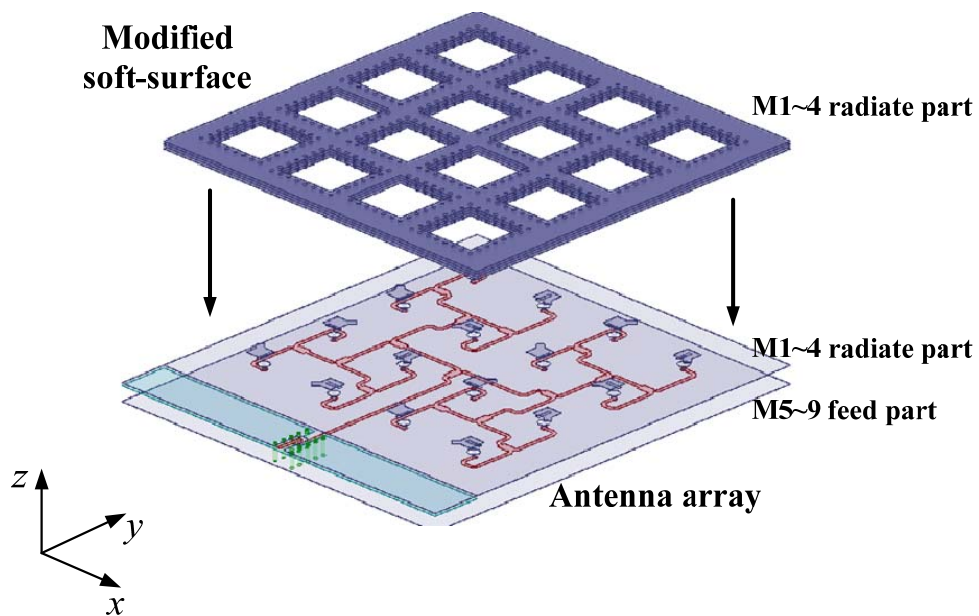


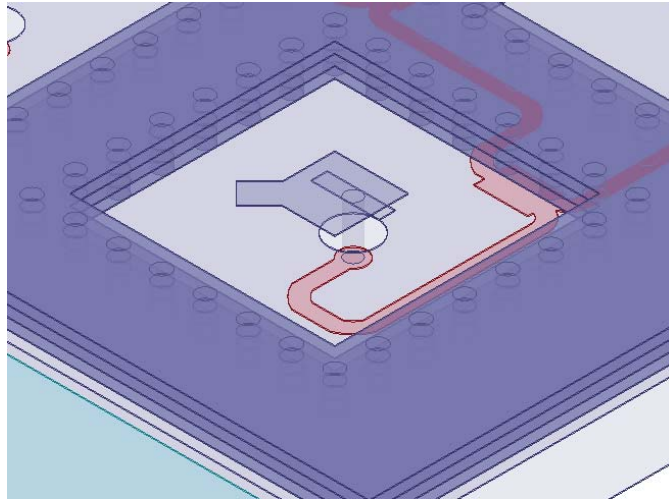
Figure 3-20 Simulated S parameters of GCPW

3.4.2 Integration of Soft-Surface Structure

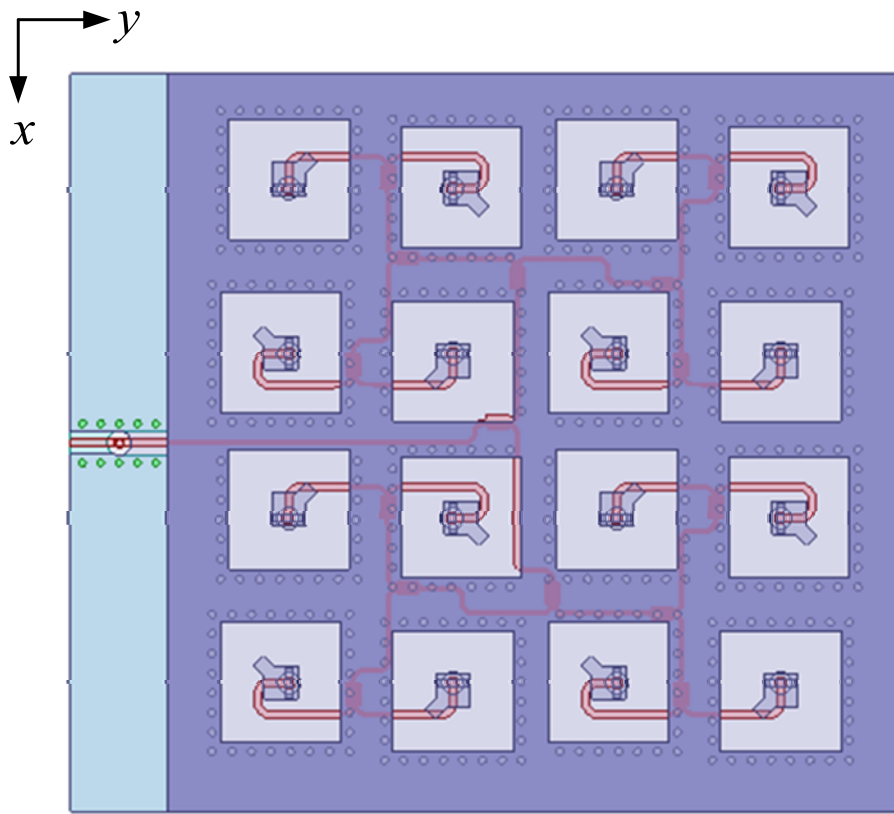
To improve the performance of the proposed antenna array, a modified soft-surface structure has been placed around each antenna element. Fig. 3-21 shows the 3-D bird view, zoomed in view, top view and side view, describing the geometry of the antenna array with the modified soft-surface structure. The function and analysis of the soft-surface structure in antenna array will be demonstrated afterwards in this section.



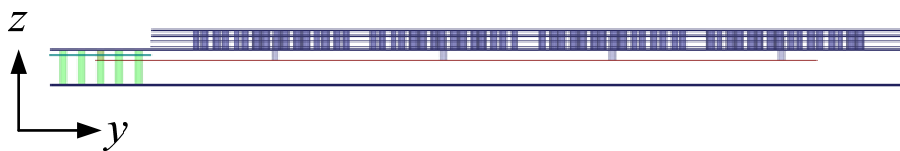
(a)



(b)



(c)



(d)

Figure 3-21 Geometry of antenna array with modified soft-surface structure

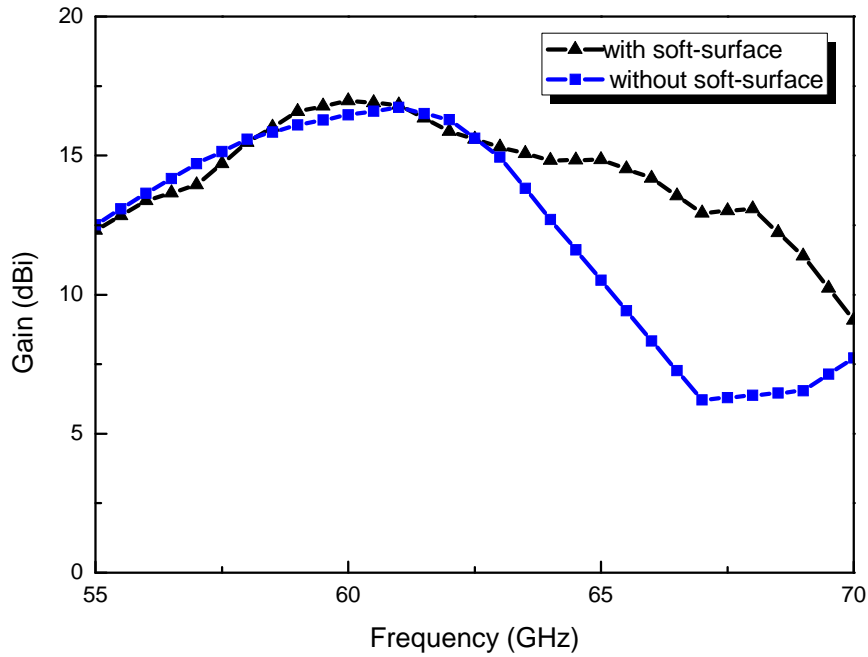


Figure 3-22 Gain comparison of proposed antenna array with and without the modified soft-surface structure

In order to demonstrate the function of the soft-surface structure, a comparison between the antenna arrays with and without the soft-surface has been performed. Despite the limitations of the LTCC fabrication our collaborator provided this time, we theoretically adopted the parameters with more advanced accuracy for better explanation. The minimum width of the metal line is set to be 0.1mm, and the minimum diameter of the via is also 0.1mm. Accordingly, the other parameters of the antenna array have been slightly changed. This comparison is just for the purpose of illustrating soft-surface structure, not for real fabrication. Fig. 3-22 shows the comparison in gain performance between antenna arrays with and without soft-surface structure. The peak gain has been increased by nearly 1 dBi, and there has been the remarkable enhancement in the 3 dB gain bandwidth, covering the whole of the unlicensed spectrum. The significant improvement in the 3 dB gain bandwidth after the introduction of the modified soft-surface structure results from the reduction of the mutual coupling, which has been analyzed in the last section.

Based on the result of gain performance, we analyzed the reduction of mutual coupling between antenna elements in calculations, especially at the higher frequency. Taking the situation at 65 GHz for example, from the gain

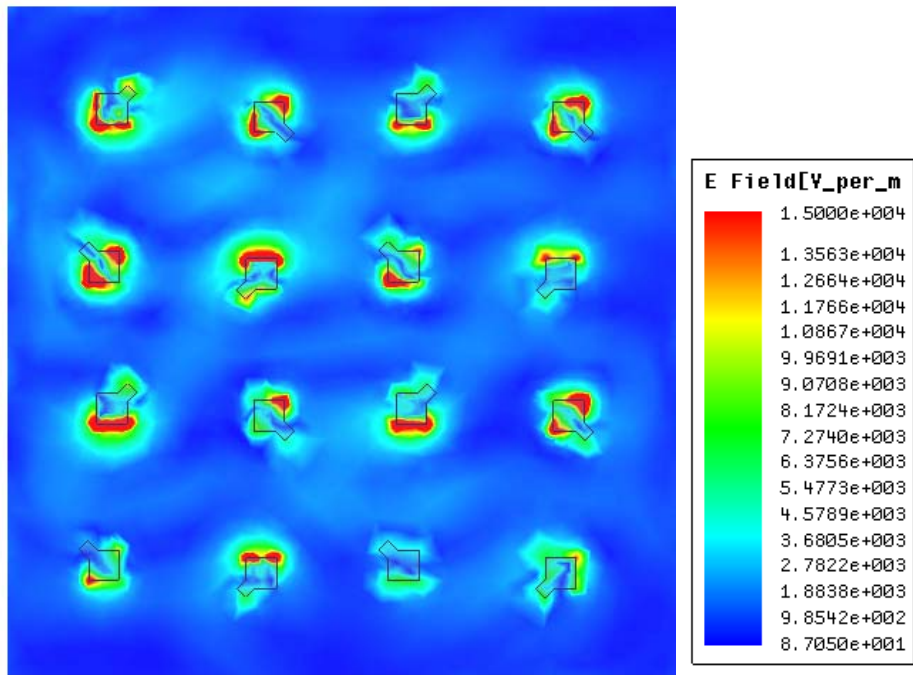
of the antenna element previously, the ideal gain of this proposed antenna array can be derived by:

$$\begin{aligned} Gain_{array} &= Gain_{element} + 10 \times \log_{10} N \\ &= 5.8 + 10 \times \log_{10} 16 = 17.8 \text{dBi} \end{aligned}$$

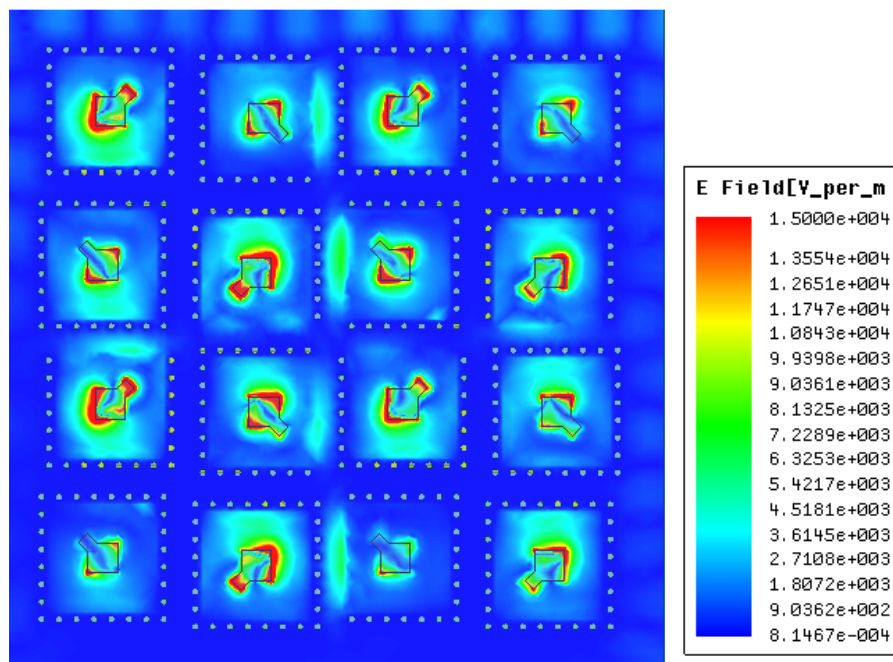
The loss of GCPW-SL is about 0.3 dB, and the loss of 4 T-junctions is about 0.8 dB. The simulated peak gain of this array at 65 GHz is 10.5 dBi. So the loss of mutual coupling in this condition is about:

$$\begin{aligned} Loss_{coupling} &= Gain_{identical} - Gain_{simulated} - Loss_{GCPW-SL} \\ &\quad - 4 \times Loss_{T-junction} \\ &\approx 6.2 \text{ dB} \end{aligned}$$

After embedding the soft-surface around the antenna elements, the simulated gain has been enhanced to 14.8 dBi, meaning the mutual coupling is correspondingly reduced by approximately 4 dB. Compared with previously published antenna arrays, the kind of reduction in mutual coupling is significant as well. For further explanation, we also investigated the electrical field of antenna arrays with and without the soft-surface, as shown in Fig. 3-23, where we can see the electric field is found to be contained inside the metal ring. An obvious decrease of the field magnitude outside compared with that without soft-surface structure can be found. As a result, the mutual coupling between antennas has been reduced greatly after introducing the soft-surface structure. This improvement therefore brings benefits in the 3 dB gain bandwidth for a more stable gain performance.



(a)

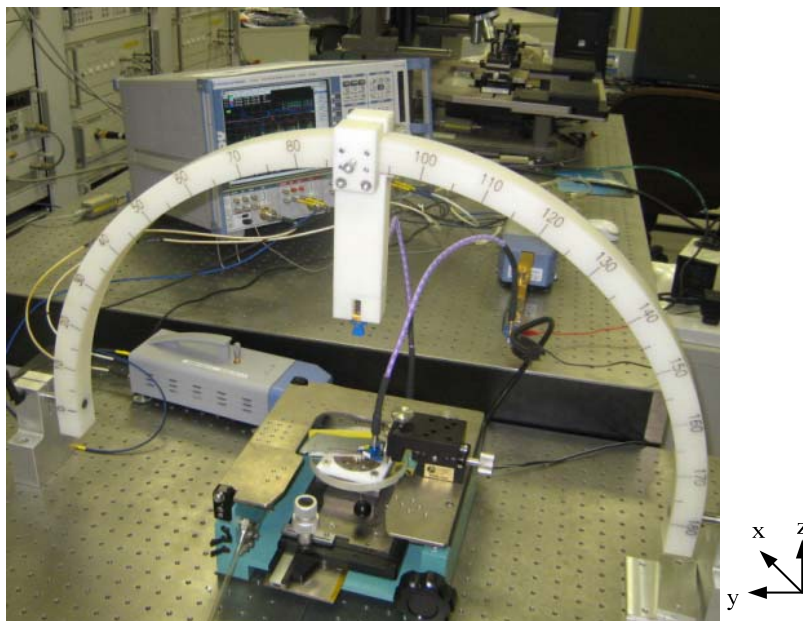


(b)

Figure 3-23 Electric field distributions on the top surface of the substrate of the patch antenna array with (a) and without (b) the soft-surface

3.4.3 Measurement and Results

The S-parameter measurements were carried out by Rohde & Schwarz vector network analyzer (VNA) ZVA75 up to 75 GHz. Fig. 3-24 shows the measurement setup using the probe station. The calibration was accomplished through the short-open-load-thru two-port standard calibration impedance substrate. A ground-signal-ground (GSG) probe with a pitch of 250 μm was touched on the GCPW line of the antenna. Due to the limitation of the VNA in our lab, the measurements were conducted up to 67 GHz.



(a)



(b)

Figure 3-24 Antenna test setup

The input matching for the antenna array is presented in Fig. 3-25. The simulated impedance matching bandwidth covers a range of 56 ~ 68 GHz, meaning a 20% bandwidth. The measured results confirm impedance matching at most zone of the bandwidth, except the measured hump around 57 GHz. This discrepancy could come from several factors, including the permittivity shift of the LTCC substrate, the different touching positions of the GSG probe, LTCC fabrication tolerance and other connection problems in the measurement system. Generally speaking, a reasonable agreement has been achieved between the simulation and measurement.

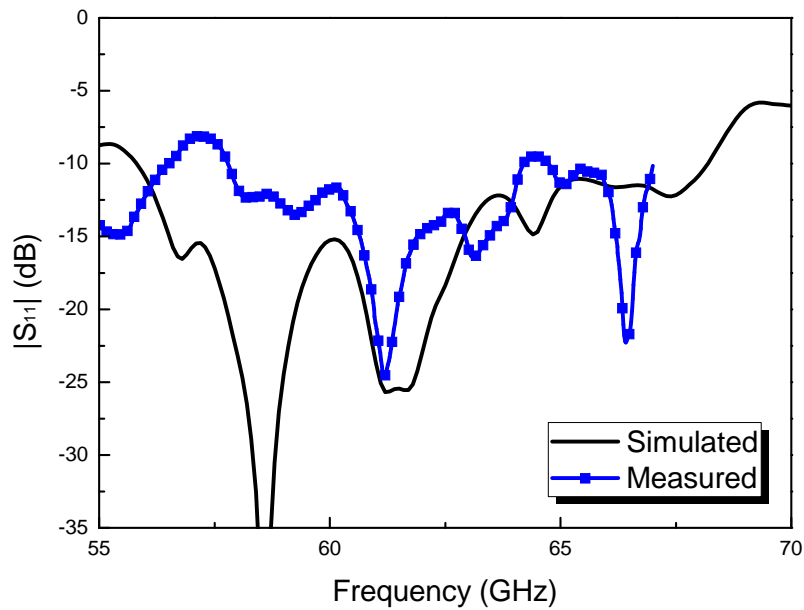


Figure 3-25 Simulated and measured return loss of proposed antenna array

For the far-field measurement setup, first, a pair of high-gain discrete horn antennas is connected to VNA port 1 and 2. The horn-to-horn antenna link is used as a calibration standard. After that, a standard horn antenna connected to port 2 is used as the transmitting antenna and our designed antenna is connected to port 1 as the receiving antenna. The tested antenna gain in the two-step method is extracted by subtracting two measurement datasets. So the designed antenna gain can be calculated as:

$$G_{AUT} = H_2 - H_1 + G_{horn} + \Delta \text{ dB}$$

where H_1 and H_2 are the link transmission gain of horn-to-horn and the link transmission gain of tested antenna to horn, respectively. G_{horn} and G_{AUT}

are the standard horn antenna gain and tested antenna gain, respectively, $\Delta|_{dB}$ is the loss difference between coax/horn and coax/probe transition. In this measurement setup, the loss difference is about 1dB according to the instructions of the probe.

Using a GSG RF probe with a pitch of 250 μm , the tested antenna senses the radiation in the broadside direction from the horn antenna, which is at a 15 cm distance away on the top of the antenna under test and the far-field condition is met. The tests are conducted with the horn at 0° position (E field of the horn is in y -direction) and 90° position (E field of the horn is in x -direction), respectively. The circularly polarized characteristics are observed with both transmission coefficients at 0° and 90° positions having the similar amplitude. So the AR can be calculated by subtracting two measurement datasets:

$$AR = |T_2 - T_1| \text{ dB}$$

where T_2 and T_1 are the measured datasets when the horn is at 0° position and 90° position, respectively. The gain of circularly polarized antenna was measured and calculated using the partial gain method. The partial gain was combined to give the total gain of circularly polarized antennas as follows:

$$G = 10 \log(G_V + G_H)$$

where G_V and G_H are the vertically and horizontally measured gain by horn antennas, which can be calculated based on the formula of G_{AUT} .

Simulated and measured AR values are presented in Fig.3-26. AR performance is less than 3 dB in the frequency range from 53.5 GHz to 68.5 GHz, while measured AR is less than 3 dB in the frequency range from 55.5 GHz to 67 GHz. If the measurement setup permits several pairs of orthogonal positions, the CP test can be more accurate [92]. Fig. 3-27 shows the simulated and measured gain of the antenna array. The 3-dB gain bandwidth is from 56.1 GHz to 64.2 GHz, covering the commonly used unlicensed 60-GHz bandwidth. The measured peak gain at 62 GHz is about 17.2 dBi, as well as the simulated peak gain is 17.11 dBi at 61 GHz. The fabrication tolerance and measurement

system loss coming from the cables or the adapters may result in a small discrepancy between the simulated and measured gain performance. Fig. 3-28 shows the radiation patterns of the proposed T-probe antenna array at frequencies 57 GHz, 60 GHz, and 64 GHz, respectively for yz - and xz -planes. The radiation patterns are stable in the unlicensed 7 GHz frequency bandwidth.

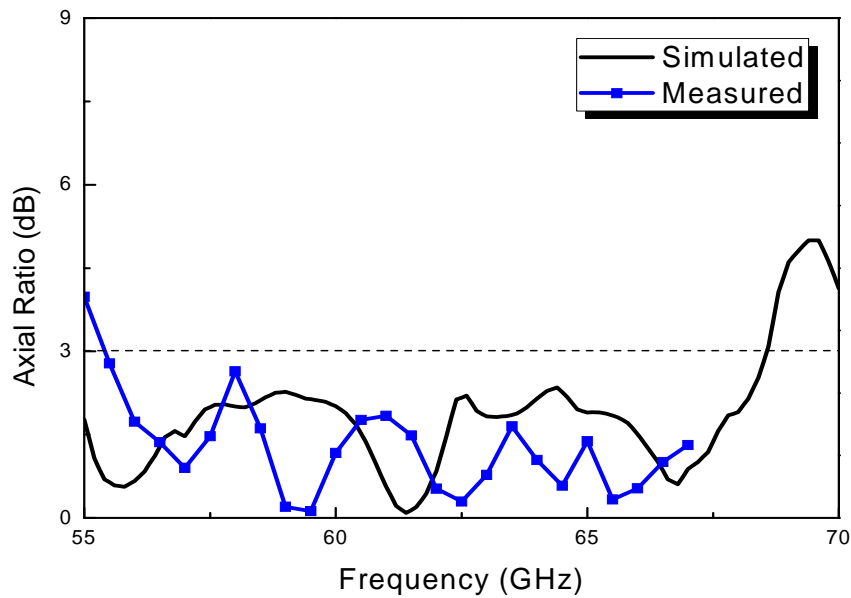


Figure 3-26 Simulated and measured axial ratio of proposed antenna array

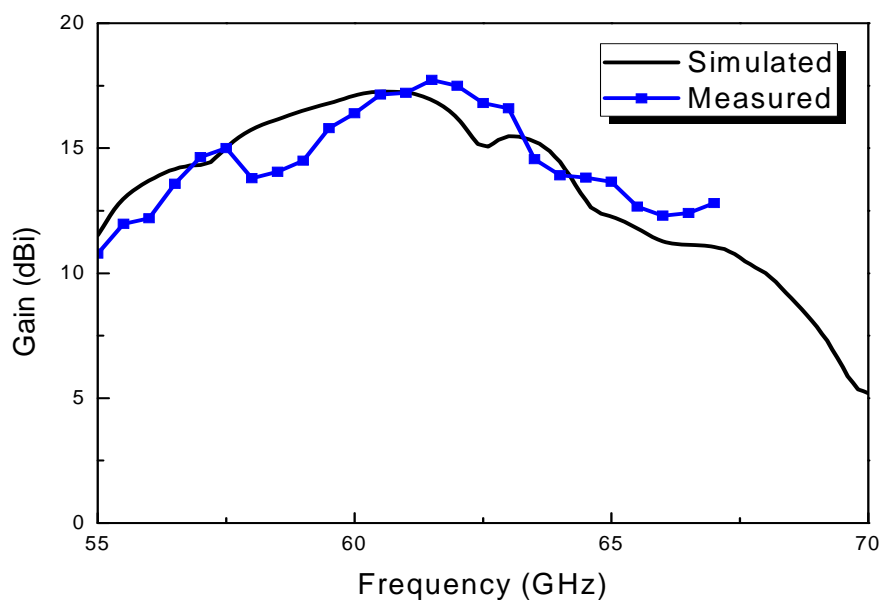
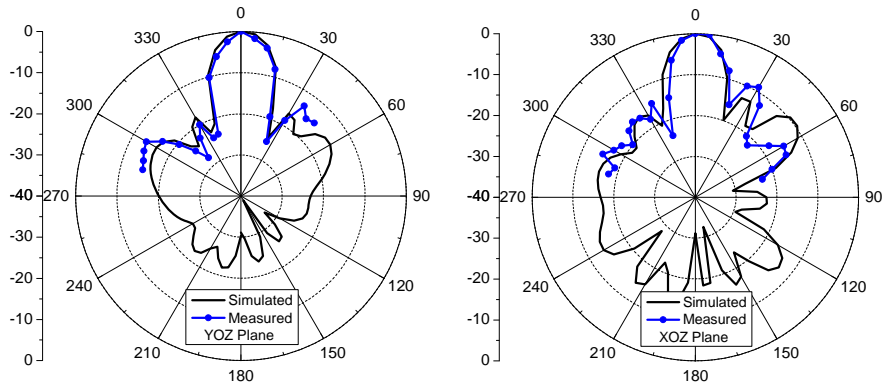
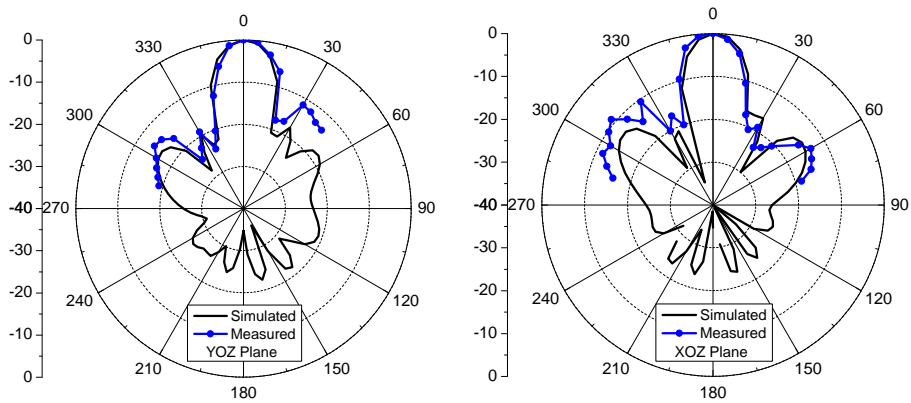


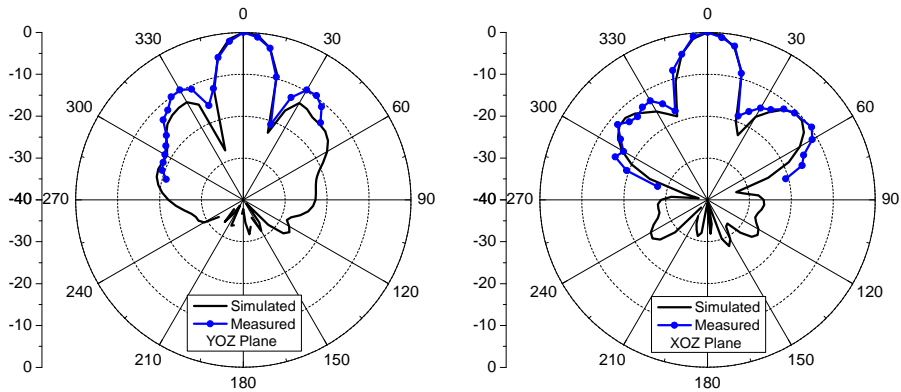
Figure 3-27 Simulated and measured gain of proposed antenna array



(a)



(b)



(c)

Figure 3-28 Measured and simulated radiation patterns at (a) 57GHz, (b) 60GHz, (c) 64GHz

3.5 Circularly Polarized T-probe Slot Antenna Array with Soft-Surface in LTCC

3.5.1 Antenna Array with Soft-Surface Structure

Fig. 3-29 shows the geometry of the 4×4 T-probe slot patch antenna array with the modified soft-surface structure. The distance between adjacent antennas is 3.35 mm and the size of the entire antenna array package is $15 \times 17 \times 0.9$ mm³. As with the previous T-probe stubbed patch antenna, each slot antenna element is rotated with respect to its adjacent element. The quarter-wave T-junction and GCPW transition remain the same as well. To improve the performance of the proposed antenna array, a modified soft-surface structure was placed around each antenna element. Also, the array was fabricated in LTCC technology under the minimum accuracy of 0.15mm.

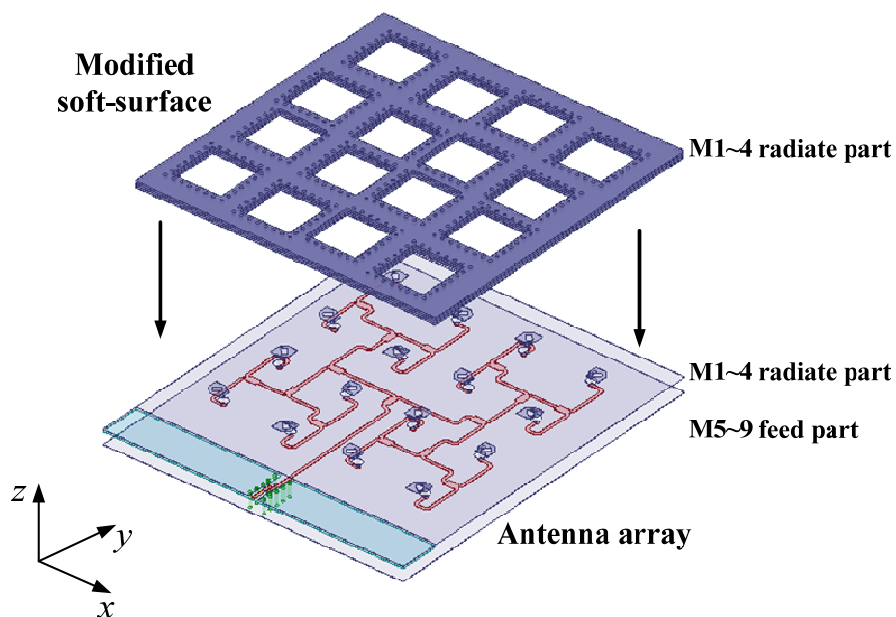


Figure 3-29 Geometry of patch antenna array with the modified soft-surface structure

3.5.2 Measurement and Results

The input matching for the antenna array is presented in Fig. 3-30, from which we can see that the simulated impedance matching bandwidth covers a range of 55 ~ 65.1 GHz, meaning a 17% bandwidth. The measured results confirm impedance matching at most zone from 55 GHz to 64 GHz, except the

hump at 57 GHz. This difference could result from a permittivity shift of the LTCC substrate, the different touching positions of the GSG probe, LTCC fabrication tolerance and other connection problems. AR performance is presented in Fig.3-31, indicating that AR is less than 3 dB in the frequency range from 55 GHz to 68 GHz, while the measured AR agreed with simulation. Fig. 3-32 shows the gain performances of the antenna array from both the simulation and measurement. The simulated peak gain at 62 GHz is about 17.3 dBi, as well as the 3-dB gain bandwidth is from 56 GHz to 64.4 GHz. The measured peak gain at 62 GHz is 16.9 dBi. Fig. 3-33 shows the radiation patterns of the proposed T-probe antenna array at frequencies 57 GHz, 60 GHz, and 64 GHz, respectively for yz- and xz-planes. The radiation patterns are stable in the unlicensed 7 GHz frequency bandwidth.

Table 3-4 lists and compares the performances among published LTCC antenna arrays in 60-GHz. It is seen from the table that the performances obtained are quite competitive with most of the reported designs.

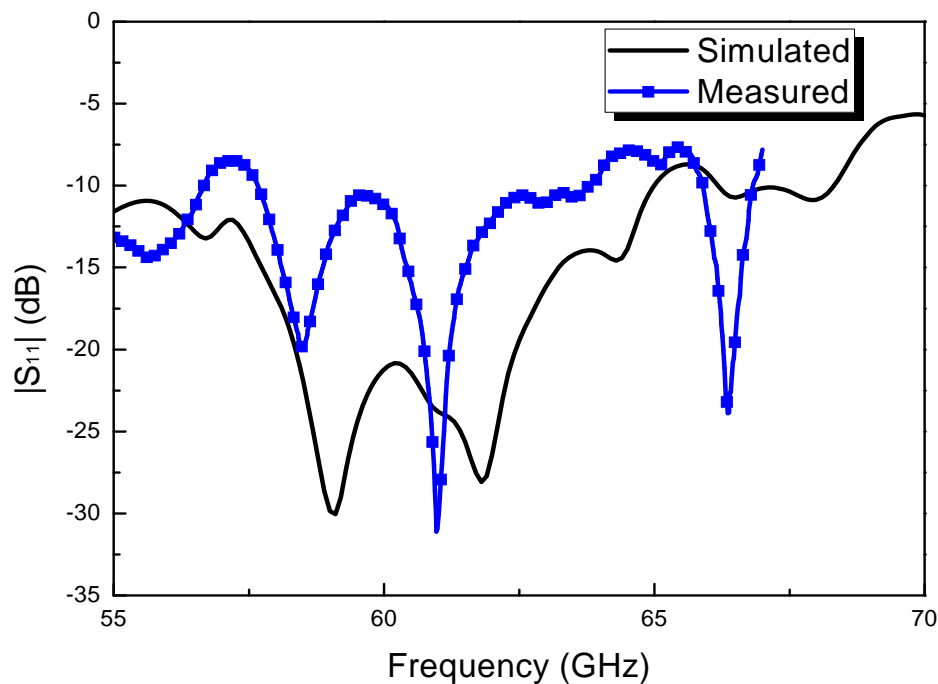


Figure 3-30 Simulated and measured return loss of proposed antenna array

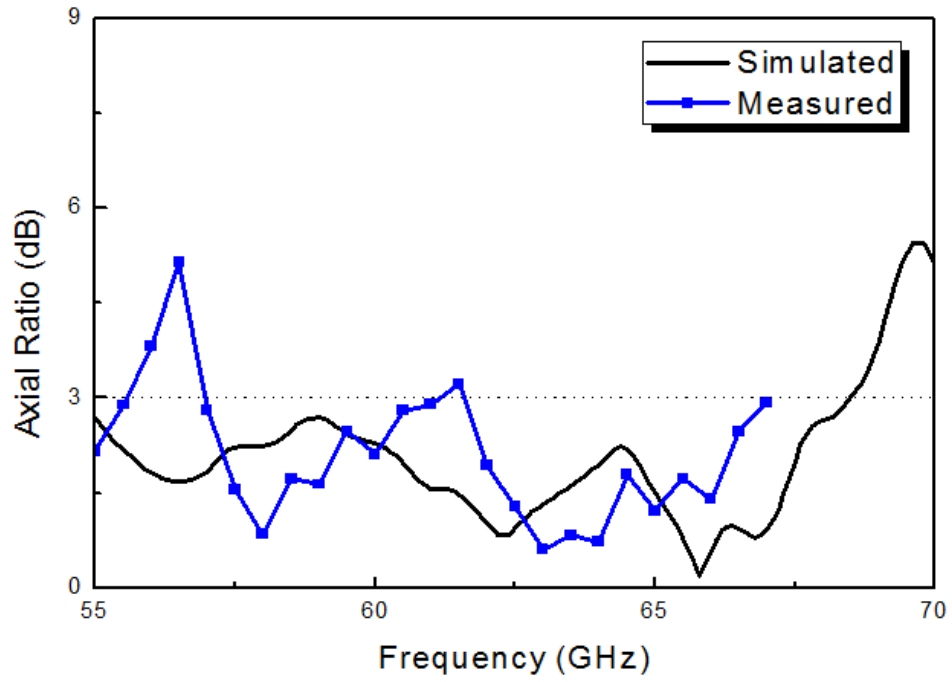


Figure 3-31 Simulated and measured axial ratio of proposed antenna array

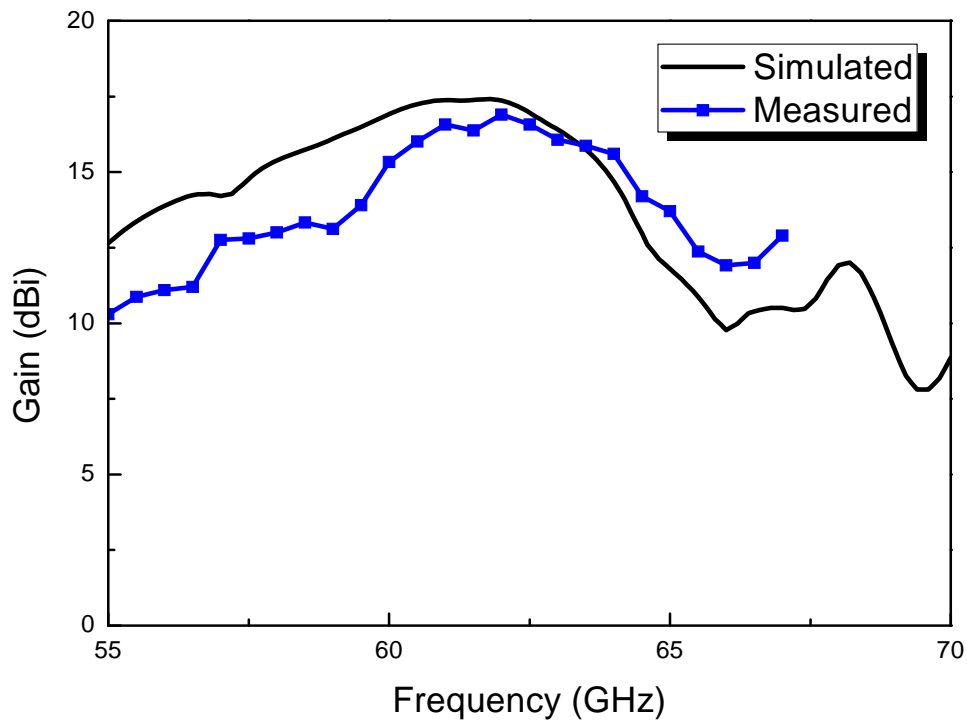
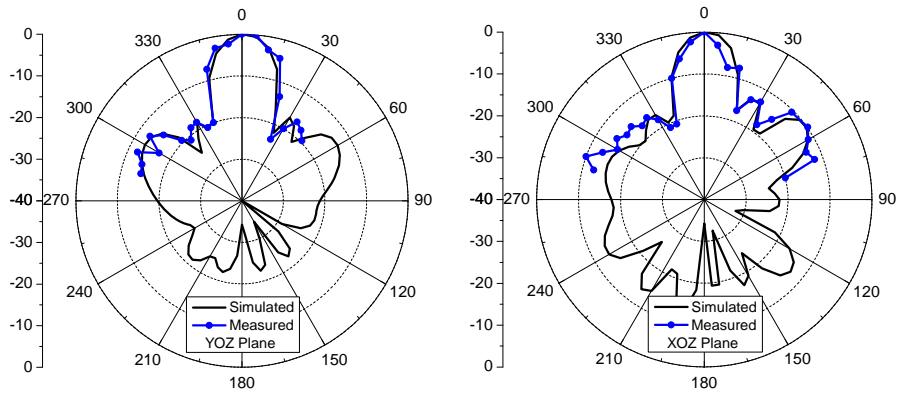
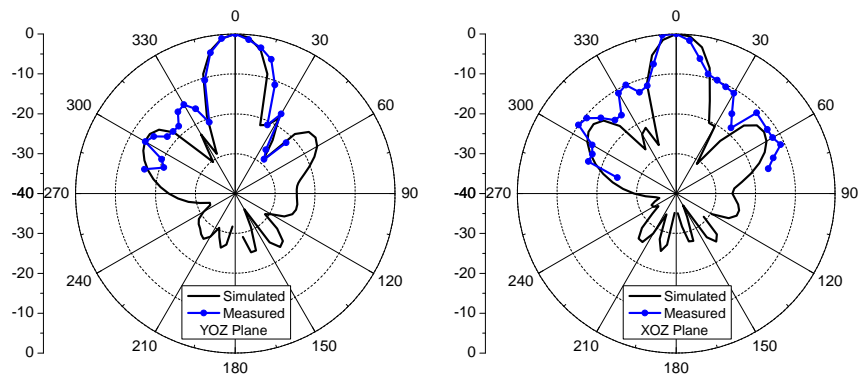


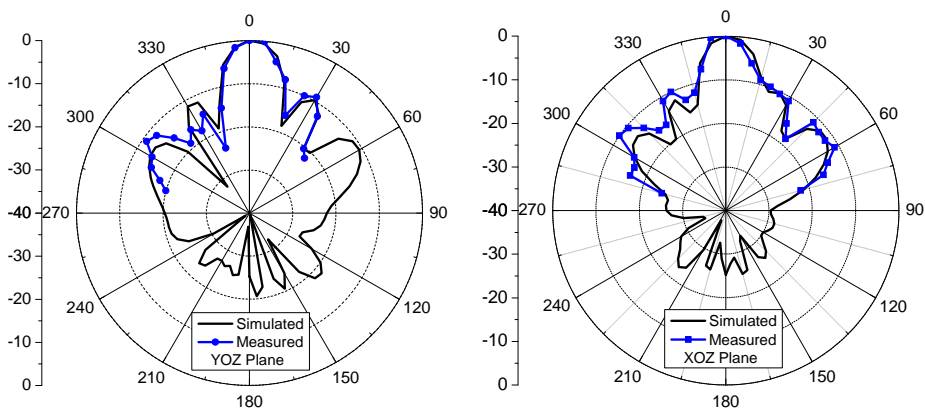
Figure 3-32 Simulated and measured gain of proposed antenna array



(a)



(b)



(c)

Figure 3-33 Measured and simulated radiation patterns at (a) 57GHz, (b) 60GHz, (c) 64GHz

TABLE 3-4 COMPARISON WITH REPORTED 60GHZ LTCC 4×4 ANTENNA ARRAYS

Type of Antenna	BW	Peak Gain	AR Bandwidth	Polarization
Grid Antenna Array [36]	14.3%	14.5 dBi	NA	LP
Patch Antenna Array with UC-EBG [51]	5.4%	18 dBi	NA	LP
Patch Antenna Array with Open Air Cavities [52]	13%	16.5 dBi	NA	LP
Patch Antenna Array with Embedded-cavities [49]	9.5%	18.2 dBi	NA	LP
Patch Antenna Array with Soft-surface [53]	29%	17.5 dBi	NA	LP
Aperture Coupled Patch Array [90]	11.5%	16.2 dBi	8%	CP
U-Slot Patch Array [91]	>16.5%	16 dBi	11.5%	CP
Helical Antenna Array [93]	14%	15.2 dBi	12%	CP
Our T-probe Stubbed Patch Antenna Array	20%	17.1dBi	25%	CP
Our T-probe Slot Patch Antenna Array	23%	16.9 dBi	22%	CP

3.6 Summary

In this chapter, we have proposed two 4× 4 LTCC T-probe CP patch antenna arrays with a modified soft-surface structure for 60 GHz applications. The introduced soft-surface structure has proved to be quite effective in suppressing the surface wave and reducing the mutual coupling. Compared with previous 60 GHz CP antenna arrays, our proposed antenna arrays feature wider impedance bandwidth, higher peak gain, and stable gain bandwidth.

Chapter 4: Multibeam Antenna Arrays with Multiple Polarizations

4.1 Introduction

Multibeam array antennas can be applied to form switched-beam array antennas with a switch circuit in front of the fixed beam forming network (BFN) such as a Rotman lens or a Butler matrix. In this way, steerable antennas benefit the selection of the best signal path for 60-GHz wireless communications [100]-[103].

A 60-GHz switched-beam array antenna employing advanced thin film and flip-chip technology has been illustrated by Lee *et al.* This 4×8 Rotman lens fabricated on a 30 μm thick substrate form four beams in the $\pm 6^\circ$ and $\pm 18^\circ$ directions. In order to reduce the parasitic effects in the 60-GHz radios, they have optimized the flip chip structure for heat dissipation. The fabricated switched-beam array antenna shown in Fig. 4-1 has an effective isotropic radiated power of higher than 17.3 dBm in the $\pm 6^\circ$ and $\pm 18^\circ$ directions [100].

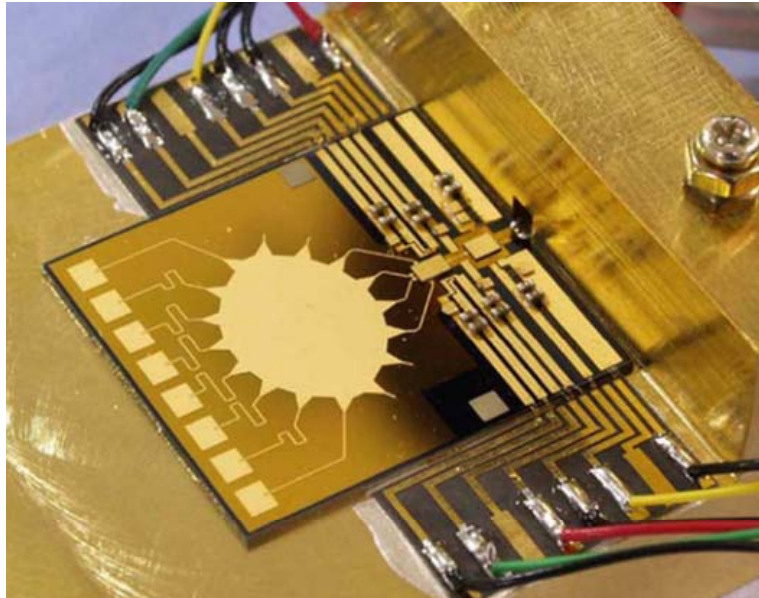


Figure 4-1 Photograph of the beam-steering antenna in package [100]

In [103], Choi *et al.* present a 60-GHz switched-beam array antenna using a single-chip beam-former integrated circuit consisting of an absorptive switch and a 4×4 Butler matrix in 0.13 μm CMOS technology. The isolation has been enhanced by the absorptive switch and thus unwanted degradation of the radiation patterns can be avoided. A two metal layer PCB has been used to feed the microstrip patch array antenna and to carry the CMOS beamformer chip. The whole design can achieve a gain of 4.14 dBi in the ±12° directions and lower in the ±44° directions. This poor gain performance is caused by the lossy substrate in 0.13 μm CMOS technology.

The above two switched-beam array antennas using the Rotman lens or Butter matrix allow scanning only in some predetermined directions on one plane and cause a missing link even in the most important boresight direction since 0° is typically not in the predetermined directions. Moulder *et al.* presented a novel switched-beam network containing two 4×4 Butler matrices and four hybrid couplers [104]. It was printed on an RT Duroid 5880 substrate together with a 2×4 patch array to create eight 2-D beams across the 60-GHz band.

Due to the fabrication limitations of CMOS and PCB, these array antennas encounter a fundamental challenge, namely the circuit size. Their practical use is still limited considering the relative large size. In contrast, multilayer technology is considered to be an effective approach to miniaturize the multibeam antenna arrays. Among several different multilayer fabrication technologies, the LTCC process has been widely used, which is convenient for integrating the feeding network and radiators together. Such technology has presented its superiority in several millimeter-wave applications [90]-[93]. To compensate for the high path loss at millimeter-wave bands, an antenna array with high gain is more preferable. However, the gain enhancement of the antenna array is limited by the loss caused by its feeding network, such as a microstrip-line feeding network. Therefore, the SIW feeding network is widely used at 60-GHz because of its low transmission loss.

As one of the most popular BFNs, Butler matrix has been realized in SIW structures [105]-[109]. The conventional SIW-based Butler matrix consists of four 3dB couplers, two crossings and fixed phase shifters, thus it usually has complicated configuration and occupies a large circuit area. Researchers have attempted to reduce the size of the Butler matrix using the multilayer technology in [110]-[112]. However, it should be noted that the used BFN and the radiator array are placed side by side in a two-dimensional plane leading to a large area. In this situation, it is potential to reduce the total size of the multibeam antenna by employing a three-dimensional approach.

Based on LTCC technology and SIW structure, we design a substrate integrated multibeam array antenna fed by a folded Butler matrix. The total size of the proposed multibeam array antenna is only equal to that of the radiating aperture, which means the feeding Butler matrix is completely hidden underneath the radiators. In this way, the proposed design achieves a remarkable miniaturization. Besides the mentioned advantage in size miniaturization, this design also provides the possibility of combining the multiple-beam and multiple-polarization character together in one same antenna array. In this chapter, we present a $\pm 45^\circ$ dual linear-polarization and a dual circular-polarization substrate integrated multibeam array antenna. The scanning beam possesses an ability to change its polarization state between the 45° and the -45° linear polarization, or between the left-handed circular polarization (LHCP) and the right-handed circular polarization (RHCP), depending on the actual application requirements.

In Section 4.2, a layer-to-layer transition with the constant phase shift over a wide bandwidth has been introduced. It is crucial in the design of a multilayer miniaturized Butler matrix. The design procedure for each sub-component of the proposed multibeam array antenna has also been demonstrated there. In Sections 4.3 and 4.4, two dual linear- and circular-polarization multibeam antennas consisting of 21 stacked ceramic tapes are designed and fabricated through the LTCC process. Measured results are provided to validate the proposed designs.

4.2 Folded Butler Matrix

4.2.1 Interconnection between Layers and Self Compensation

In this design, the proposed SIW multibeam antenna is folded and distributed in different layers. Therefore, layer-to-layer transitions are necessary to connect these SIW sections, which have similar configurations as shown in Fig. 4-2. One structure is a back-forward 1-to-2 transition, transmitting the electromagnetic wave from layer 2 to layer 3. The other is a back-forward 1-to-3 transition, transmitting the electromagnetic wave from layer 1 to layer 3.

The used ceramic material is Ferro A6-M with a relative permittivity of 5.9 and loss tangent of 0.002. The width of the SIW is 1.8 mm, the diameter of the metallic via is 0.1 mm, and the distance between two adjacent vias is 0.25 mm. Each SIW layer is realized by three stacked ceramic tapes. In Fig. 4-2, $t_{s12}=1.6$ mm, $t_{sw2}=0.1$ mm, $t_{s13}=1.52$ mm, and $t_{sw3}=0.15$ mm. The simulated reflection coefficient of the 1-to-2 transition is below -23 dB within the frequency band of 50~70 GHz, while the simulated reflection coefficient of the 1-to-3 transition is below -20 dB within the frequency band of 53~63 GHz.

For a Butler matrix, the 90° phase difference is required between two branches, i.e. branch 21 and branch 43. But the original layer-to-layer structure has a high frequency dispersive phase shift as illustrated in Fig. 4-3, which certainly results in poor bandwidth-related performances. Fig. 4-3 indicates that the phase shift $\varphi_1(f)$ (phase (S43-S21)) of the layer-to-layer transition grows almost linearly with frequency. On the other hand, there exists another type of SIW phase shifter, which has two equal-length branches with two different equivalent widths p_{we1} and p_{we2} ($p_{we1} < p_{we2}$). The phase shift (phase (S43-S21)) of this phase shifter decreases with the frequency. Hence the concept of phase compensation can be employed here, based on the fact that the varying tendencies of the phase shift versus frequency obtained by the layer-to-layer transition and the equal-length unequal-width SIW structure are just opposite. By combining them, a flat relative phase shift covering a wideband can be achieved.

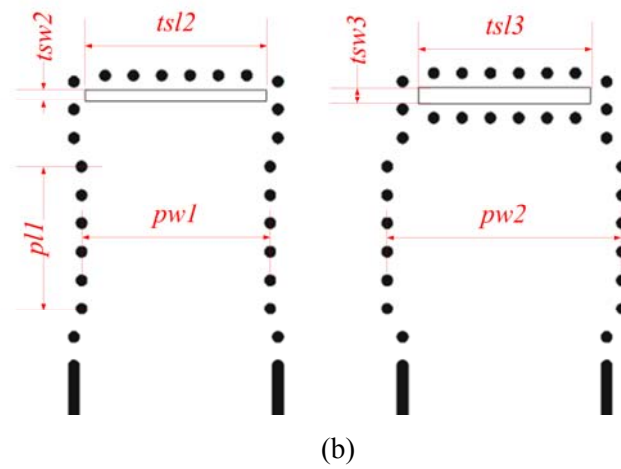
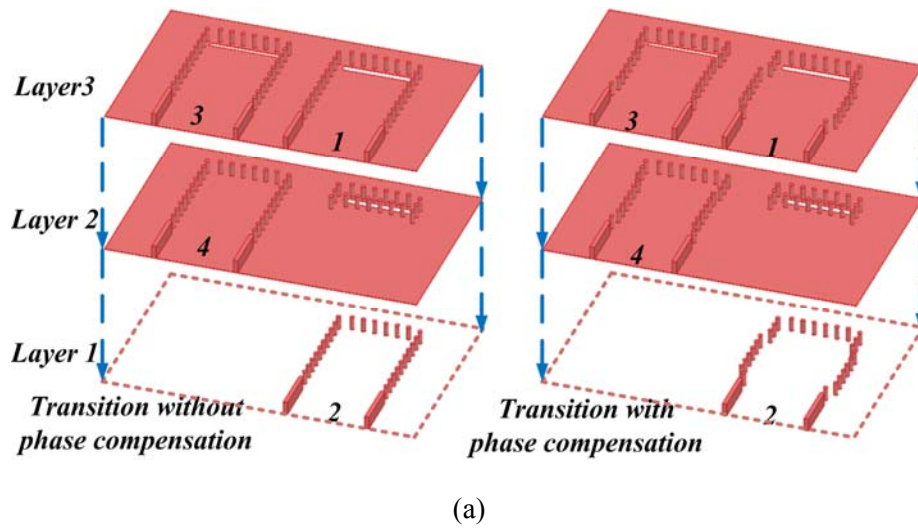


Figure 4-2 Configuration of the proposed interconnection between layers: (a) without phase compensation, (b) with phase compensation, and (c) top view.

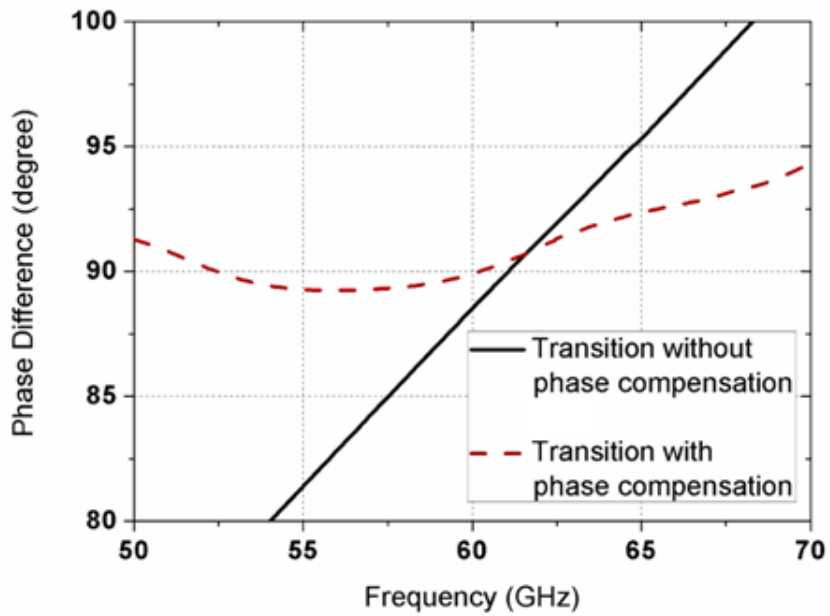


Figure 4-3 Phase characteristics of the proposed interconnection between layers

The design procedure can be summarized as follows. Firstly, the first-order derivative of phase shift $\phi_1(f)$ with respect to f for the layer-to-layer transition before compensation can be fitted from the simulated curve in Fig. 4-3. Secondly, the following equation:

$$\frac{d\phi_1(f)}{df} = \frac{4\pi\varepsilon_r pl_1}{300^2} \times \left(\frac{f}{\sqrt{\left(\frac{2\sqrt{\varepsilon_r}f}{300}\right)^2 - \left(\frac{1}{pw_{e2}}\right)^2}} - \frac{f}{\sqrt{\left(\frac{2\sqrt{\varepsilon_r}f}{300}\right)^2 - \left(\frac{1}{pw_{e1}}\right)^2}} \right) \quad (4-1)$$

can be utilized to determine the pw_{e1} and pw_{e2} with a fixed pl_1 . After modeling and optimization, the phase compensation effects are illustrated in Fig. 2. Here, $pw_1=1.664$ mm, $pw_2=2.072$ mm, and $pl_1=1.25$ mm. The phase difference between the 1-to-2 and 1-to-3 transitions is approximately 90° ($-0.75^\circ \sim 4.3^\circ$) over 50~70 GHz.

4.2.2 Design Procedure of Butler Matrix

A. Configuration

The proposed LTCC substrate integrated multibeam antenna has the configuration as shown in Figs. 4-4 and 4-5.

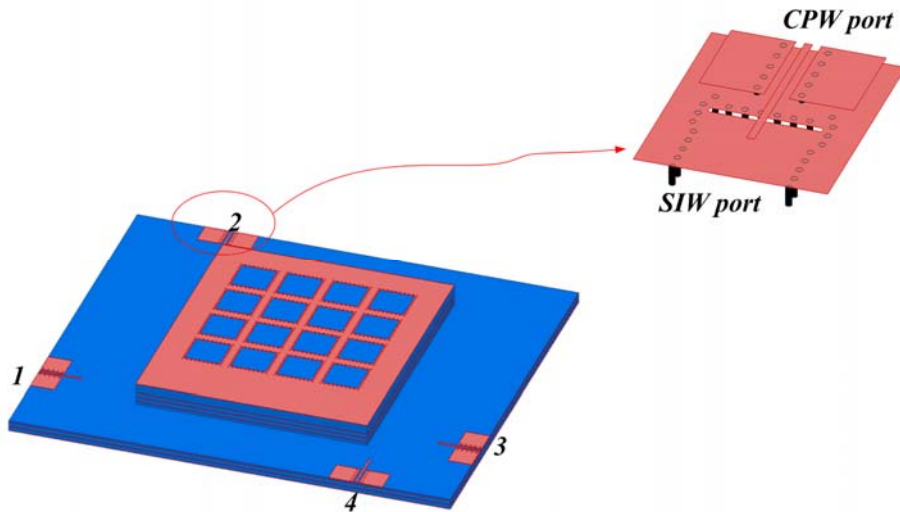


Figure 4-4 Configuration of the proposed integrated multibeam array antenna and the CPW feed structure.

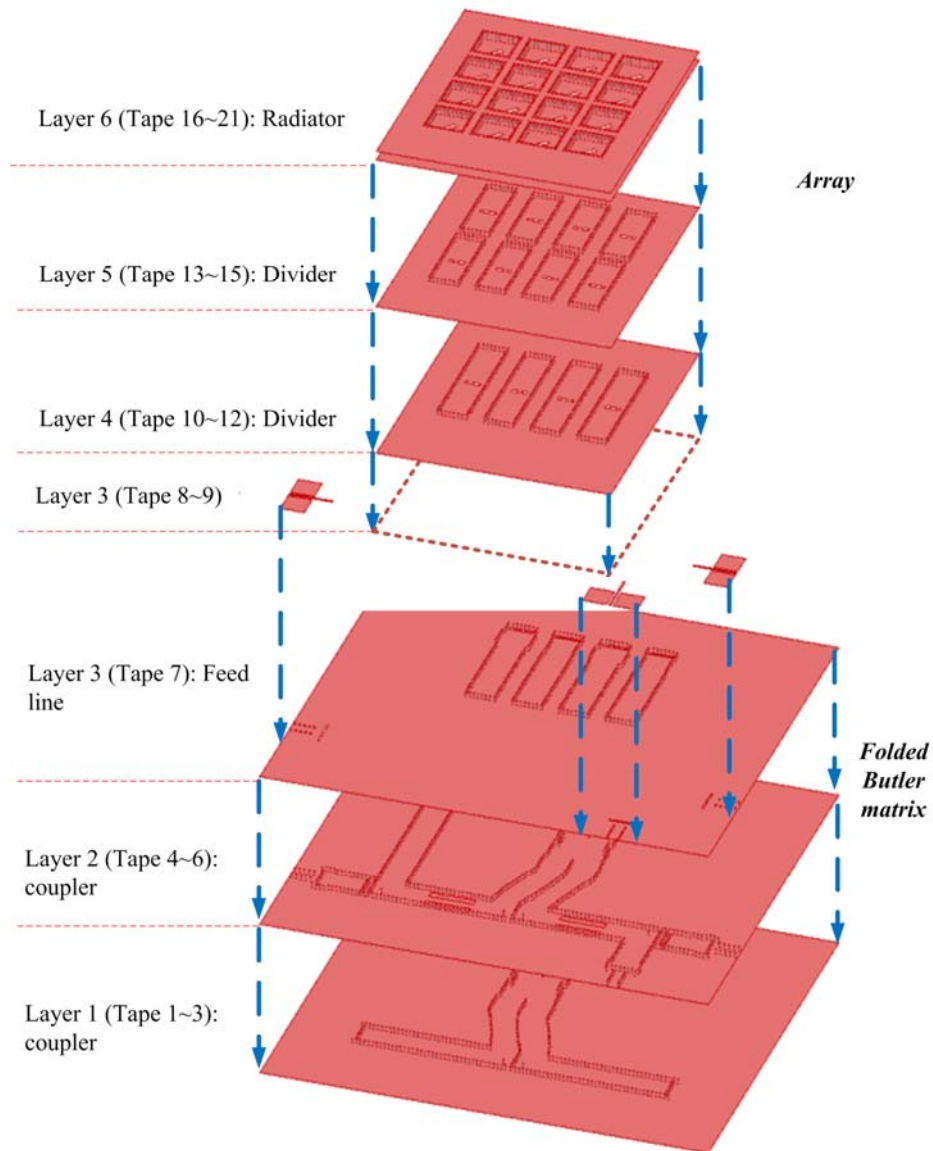
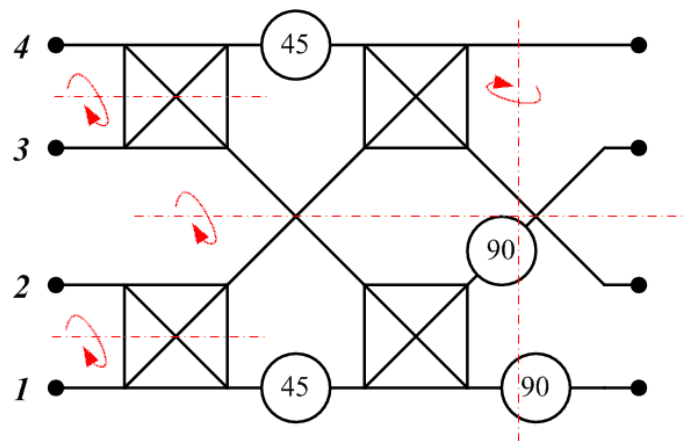


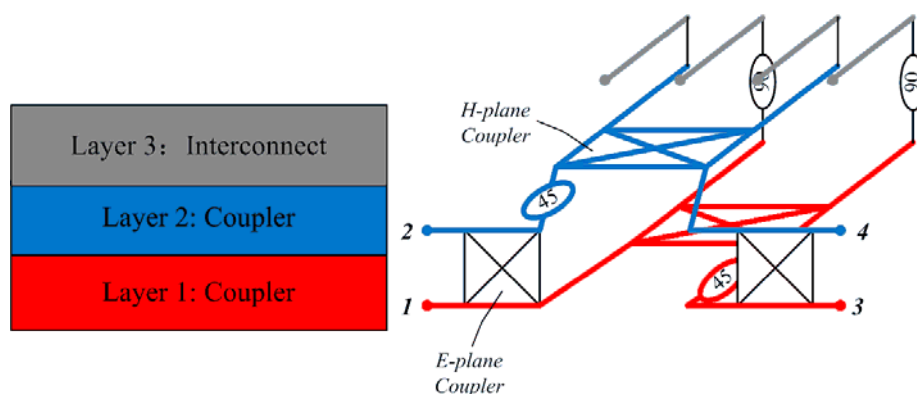
Figure 4-5 Sketch of the integrated multibeam antenna

First of all, a folded 4×4 Butler matrix is developed. An optimized topology can omit some sub-components, such as crossovers, and improve the overall performance. Therefore, the conventional Butler matrix can be folded several times to miniaturize the circuit area. As revealed in Fig. 4-6, the proposed folded Butler matrix consists of H-/E-plane couplers, layer-to-layer transitions and phase shifters. It has nine stacked ceramic tapes and each three tapes are laminated as an SIW guided-wave structure. Four input ports are distributed in layer 1 and 2 respectively. In this design, the first two couplers are E-plane version to connect two ports placed in different layers

conveniently while finish the power dividing function. Then, two H-plane couplers, which connect the output ports of two E-plane couplers respectively, are overlapped at adjacent layers. After that, the outputs of the bottom H-plane coupler are connected to layer 3 through 1-to-3 transitions, while the outputs of the H-plane coupler in layer 2 are connected by 1-to-2 transitions. Here, four output ports are all placed in layer 3. The distance between two adjacent output ports is $0.58 \lambda_0$ at 60 GHz, where λ_0 is 5mm. The fixed phase shifters are positioned properly to achieve the desired phase characteristics. Considering different applications in the following work, two Butler matrices with similar architecture but different output phase characteristics are designed. For an excitation of port 2 as an example, the desired phase difference between adjacent ports are $45^\circ/45^\circ/45^\circ$ and $-45^\circ/135^\circ/-45^\circ$, respectively.



(a)



(a)

(b)

Figure 4-6 Sketch of the folded Butler matrix: (a) 2-D; (b) 3-D.

Then, an integrated multibeam antenna can be realized by the proposed Butler matrix and a 4×4 antenna array consisting of six-layer tapes for radiators and other six-layer tapes for dividers. Ports 1 and 3 are transferred to the same layer of the ports 2 and 4 through forward 1-to-2 transitions, which has the similar configuration of the back-forward version as shown in Fig. 4-2. But the orientations of the input and output ports of the forward transition are opposite.

B. E-plane Coupler with 45° phaser

There are two different types of SIW couplers employed in this design to satisfy the compact and simple layout requirement. One is an E-plane coupler, and the other is an H-plane coupler. A double-slot E-plane coupler integrated with a 45° phase shifter is shown in Fig. 4-7. The desired phase shift comes from a pair of SIWs with different widths [113]. Ports 1 and 2 are located in the same layer, while ports 3 and 4 are in the other layer. Two long slots are cut on the broadside conductor layer near the metallic via wall. The related parameters are: $ec_l=2.8$ mm, $ec_w=0.43$ mm, $eco=0.15$ mm and $ec_p=0.6$ mm. The simulated results of such a structure are shown in Fig. 4-8. The reflection and coupling coefficients are below -20 dB within the frequency band of 55~63.5 GHz. It has well-balanced outputs. The phase difference between output ports, phase ($S_{31}-S_{21}$), is $45^\circ \pm 2^\circ$ within the radio band of 55~65 GHz.

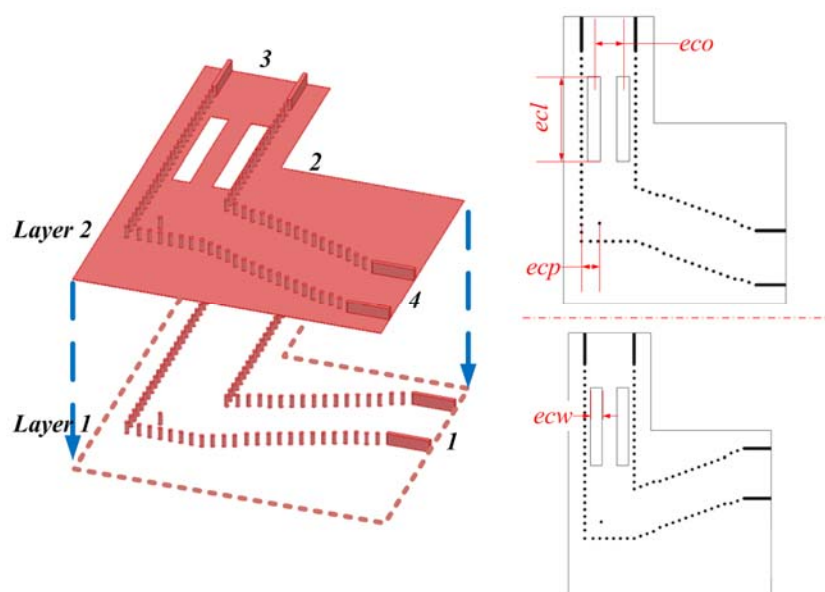


Figure 4-7 Configuration of the E-plane coupler incorporating a 45° phaser: (a) 3-D configuration, and (b) top view

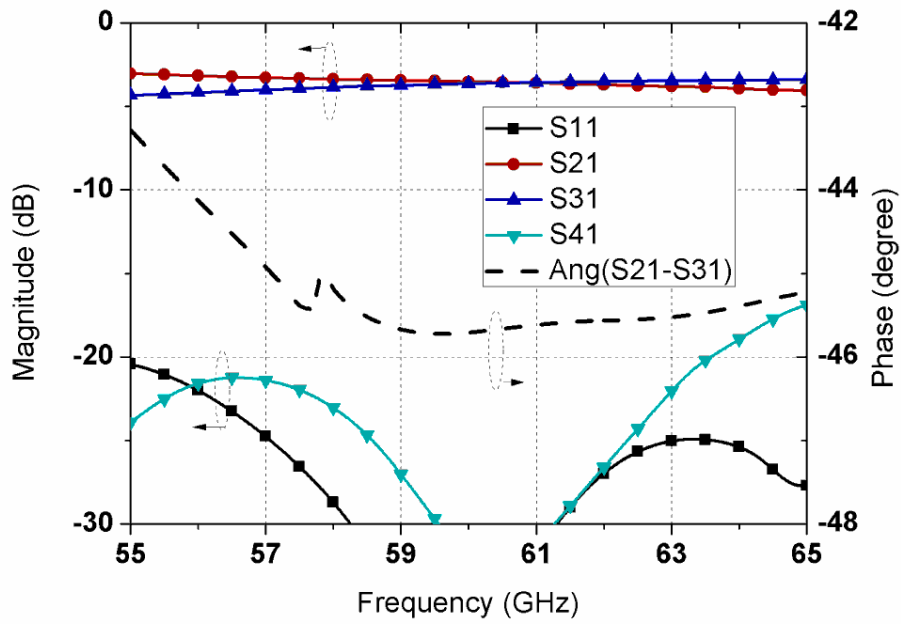


Figure 4-8 Simulated results of the E-plane coupler incorporating a 45° phaser

C. H-plane Coupler with Layer-to-Layer Transition

The employed SIW-based H-plane coupler has a continuous coupling aperture. Waveguide steps are used to achieve good matching. The configuration of two overlapped H-plane couplers with corresponding layer-to-layer transitions is shown in Fig. 4-9 and the simulated results are shown in Figs. 4-10, 4-11. The corresponding parameters are: $h_{cl}=2.05$ mm, $h_{cw}=0.3$ mm, $h_{cg}=1.02$ mm, and $h_{cp}=0.64$ mm. The reflection and coupling coefficients are almost below -20 dB within the frequency band of 56.5~64.5 GHz. The phase difference is $90.5^{\circ}\pm 1^{\circ}$ between output ports of the identical coupler within the frequency band of 57~65 GHz, and $90^{\circ}\pm 5^{\circ}$ between output ports of two couplers within the frequency band of 55~64.2 GHz.

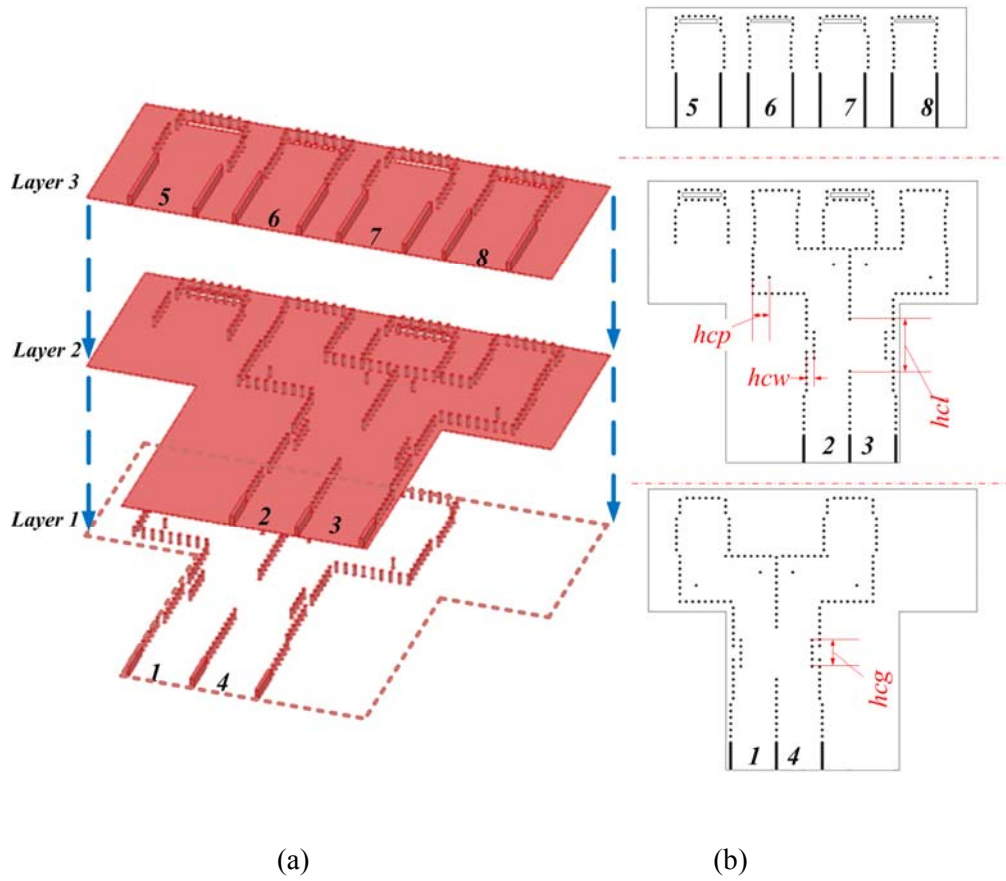


Figure 4-9 Configuration of two overlapped H-plane couplers incorporating layer-to-layer transitions: (a) 3-D configuration, and (b) top view.

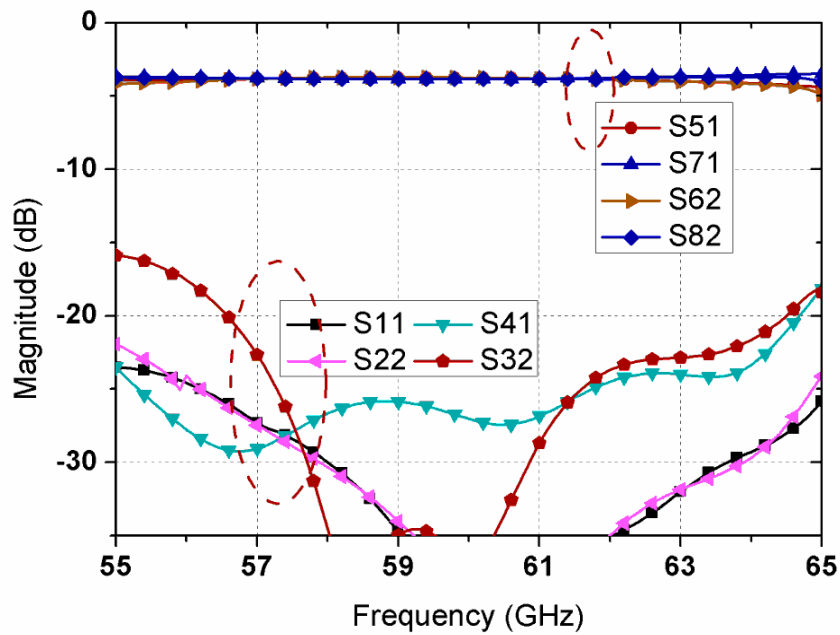


Figure 4-10 Magnitude Characteristic of two overlapped H-plane couplers incorporating layer-to-layer transitions

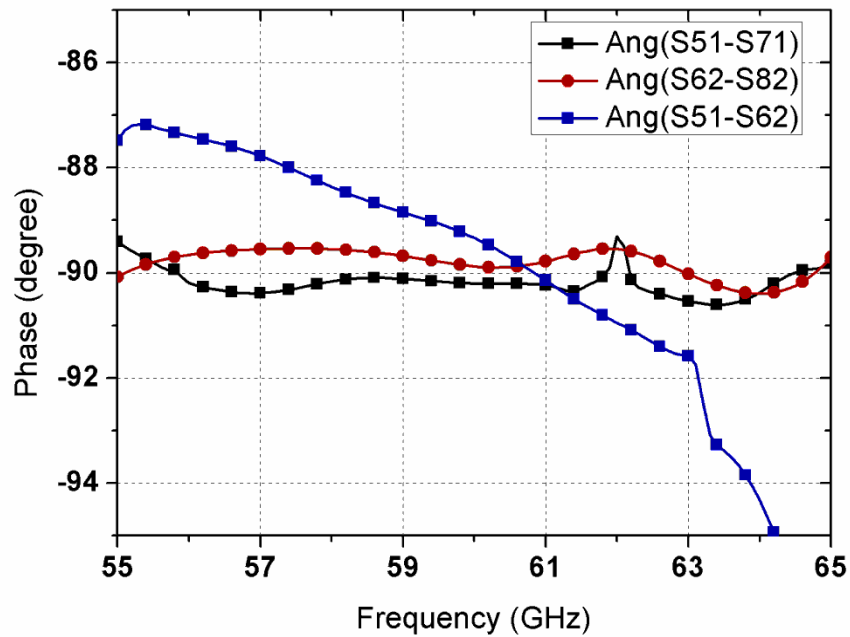


Figure 4-11 Phase characteristics of two overlapped H-plane couplers incorporating layer-to-layer transitions

4.3 Dual Linearly Polarized Substrate Integrated Multibeam Antenna Array

4.3.1 45° Linearly Polarized Antenna Element

In this design, the radiating element is an open-ended square SIW cavity as shown in Fig. 4-12. It has six stacked ceramic tapes and is fed by an SIW structure through a 45° inclined slot located on the bottom conductor plate of the cavity in order to generate a 45° LP beam. A square radiating aperture is cut on the top surface. The optimized dimensions of the element are: $avw=2.4$ mm, $acw=2.24$ mm, $asl=0.88$ mm, and $asw=0.25$ mm.

The mutual couplings between elements versus their distance at different operation frequency are investigated and depicted in Fig. 4-13.

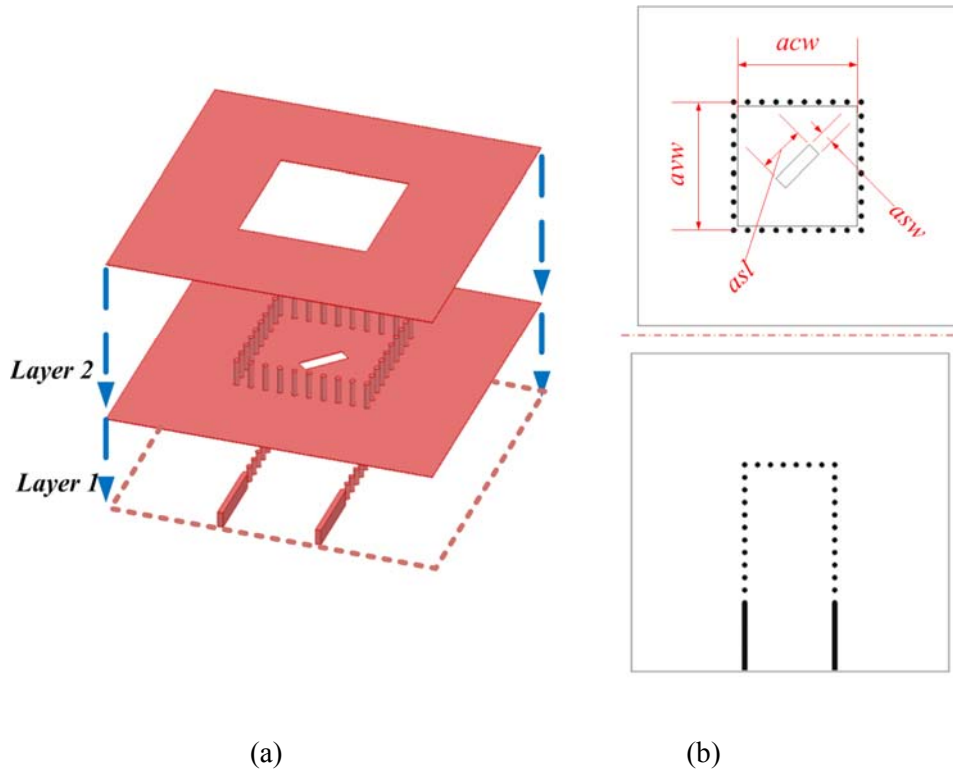


Figure 4-12 Configuration of the proposed 45° linear polarization antenna:
 (a) 3-D configuration, and (b) top view

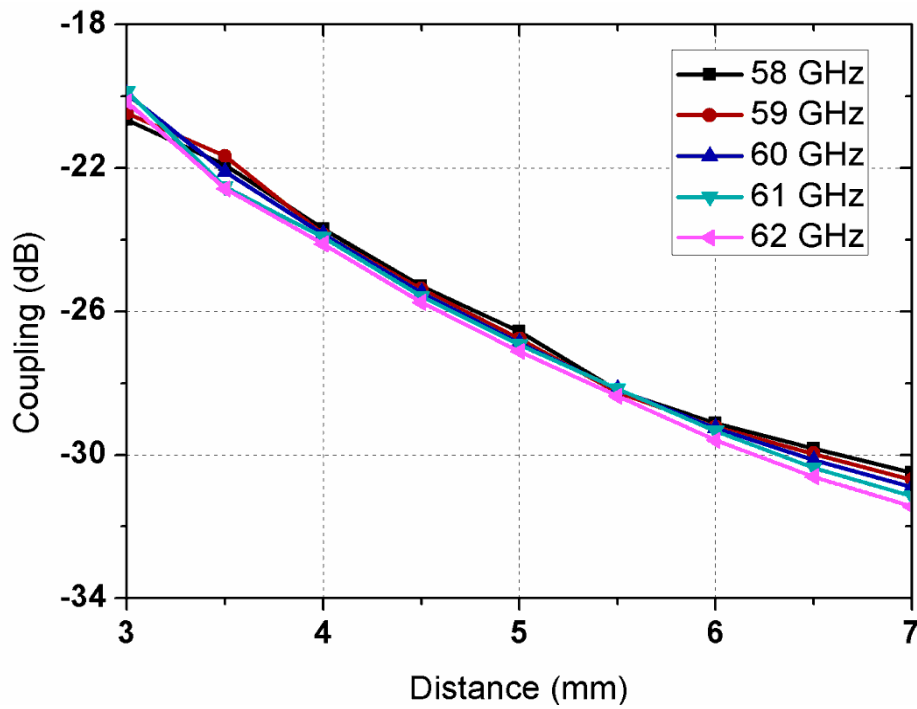


Figure 4-13 Mutual couplings between elements versus their distance at different operating frequencies

4.3.2 Antenna Array

An E-plane divider is employed to vertically feed a four- element linear array in a multilayer configuration as shown in Fig. 4-14. Fig. 4-15 shows that the achieved -10 dB bandwidth is 56.3~64.5 GHz.

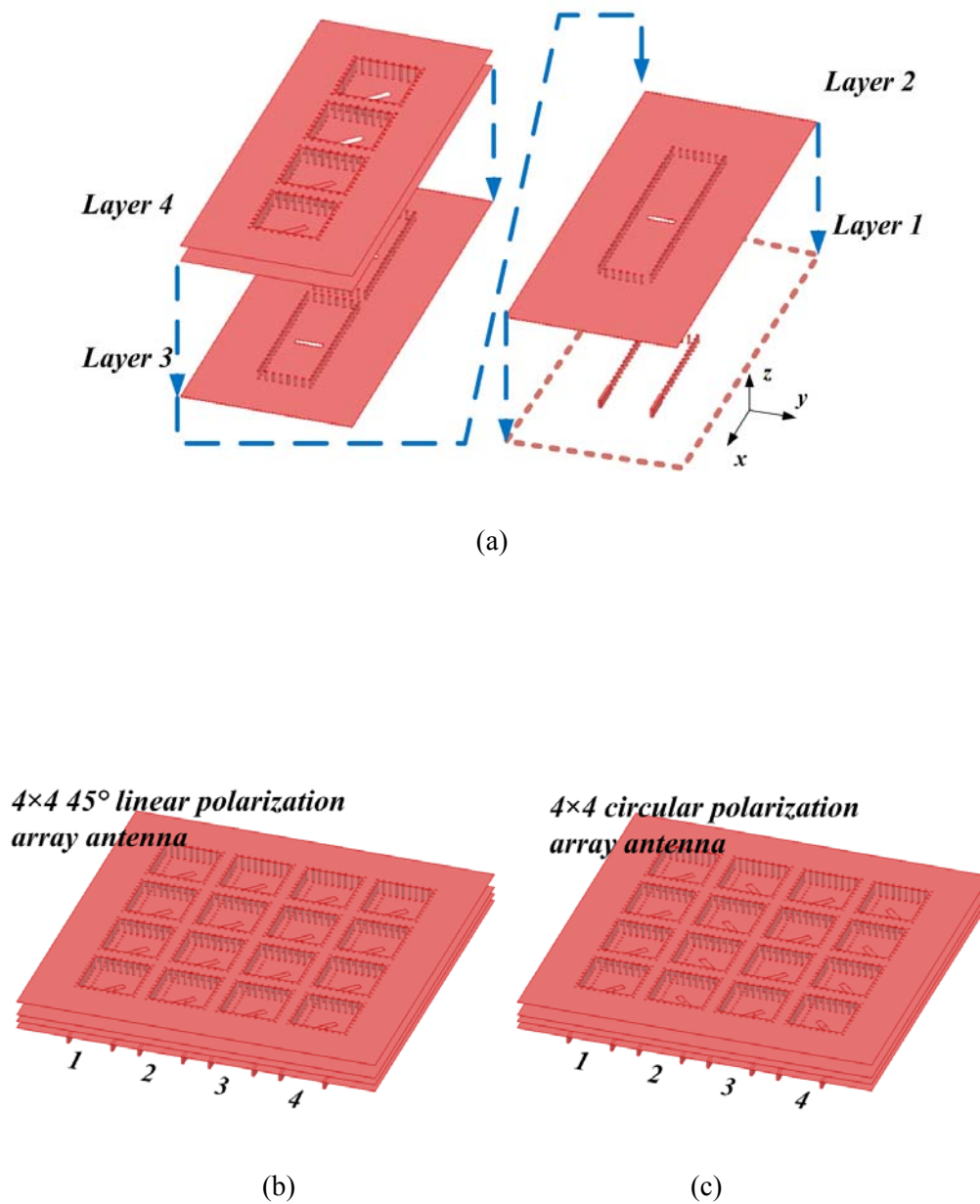


Figure 4-14 Configuration of the proposed cavity antenna array: (a) 1×4 45° LP array, (b) 4×4 45° LP array, and (c) 4×4 CP array.

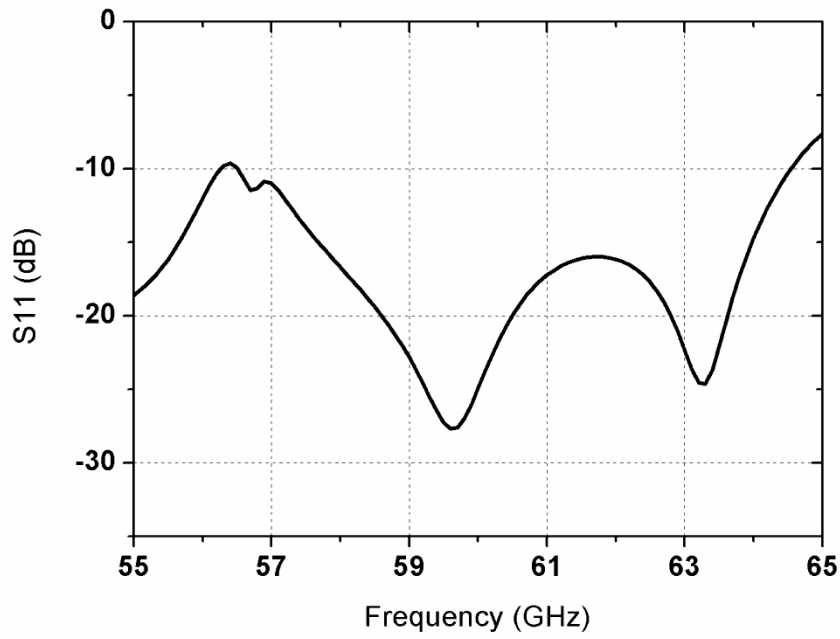


Figure 4-15 Simulated reflection coefficient of the proposed 4-element linear antenna array

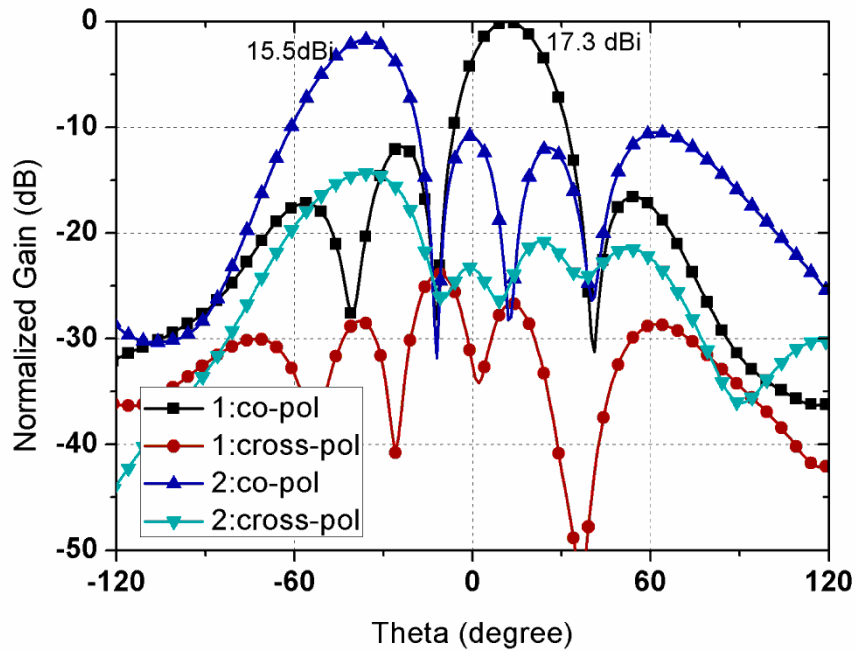


Figure 4-16 Simulated yoz-plane patterns of the proposed 4×4 45° LP array antenna (The phase for ports 1~4: case 1: 0° , 45° , 90° , and 135° ; case 2: 0° , 135° , 270° , and 405°)

Such four linear arrays can be grouped as a 4×4 45° LP array antenna. Fig. 4-16 shows the yoz-plane patterns with different phase shift between neighboring elements in simulation. The 4×4 array antenna keeps 45° LP when the beam is scanned. Thus, such two arrays with orthogonal feed slot, i.e. $\pm 45^\circ$, can be used to construct a dual linear-polarization multibeam array antenna.

Based on the above design, we employed two identical Butler matrices to excite two 4×4 antenna arrays with different polarizations, i.e. $\pm 45^\circ$. The fabricated prototype is shown in Fig. 4-17. It has 21 stacked ceramic tapes and is excited by CPWs. The total circuit area is $32.7 \times 14.6 \text{ mm}^2$ excluding the additional feeding structures. This size is approximately equal to that of two 4×4 antenna arrays.

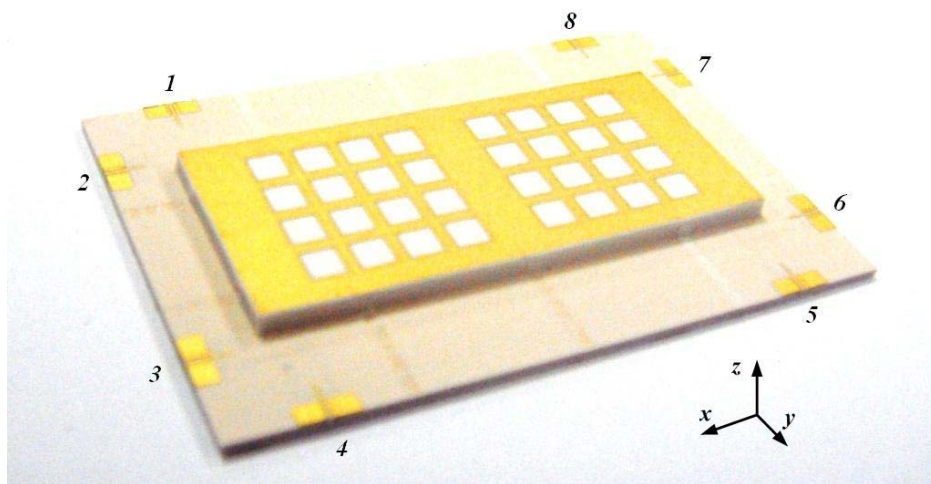


Figure 4-17 Photograph of the fabricated dual linear-polarization substrate integrated multibeam array antenna.

4.3.3 Measurement and Analysis

This multibeam antenna is measured from 55 GHz to 65 GHz by two GSG probes connected to a Rohde & Schwarz vector network analyzer. For ports 1~4, the measured reflection coefficients are shown in Fig. 4-18. A coefficient below -10 dB is achieved for all ports within the whole tested frequency band. For an excitation at port 1, the isolation to the other ports is better than 10 dB within the frequency band of 55~65 GHz as shown in Fig. 4-19. In Fig. 4-20, similar results are observed for an excitation at port 2.

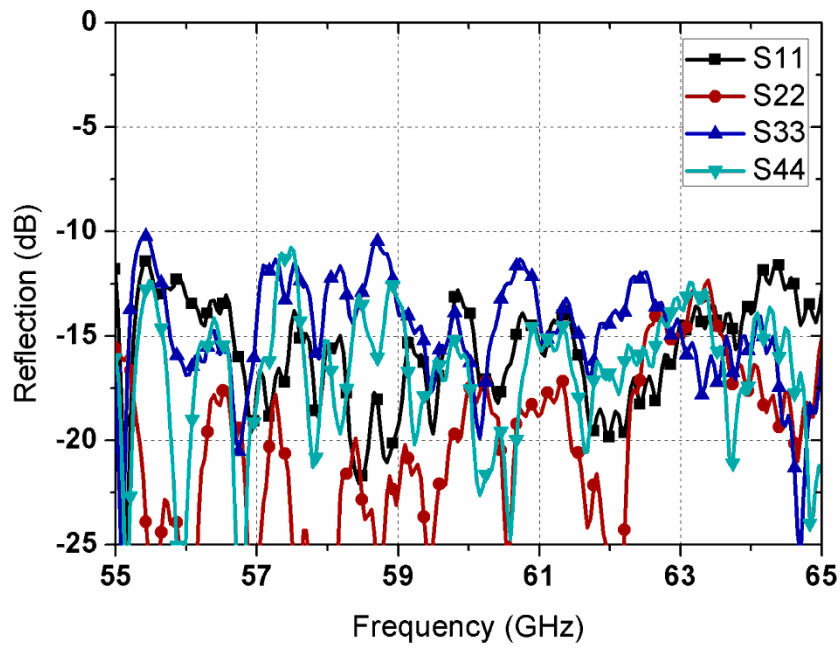


Figure 4-18 Reflection coefficients of the fabricated dual linear-polarization substrate integrated multibeam array antenna excited by ports 1~4.

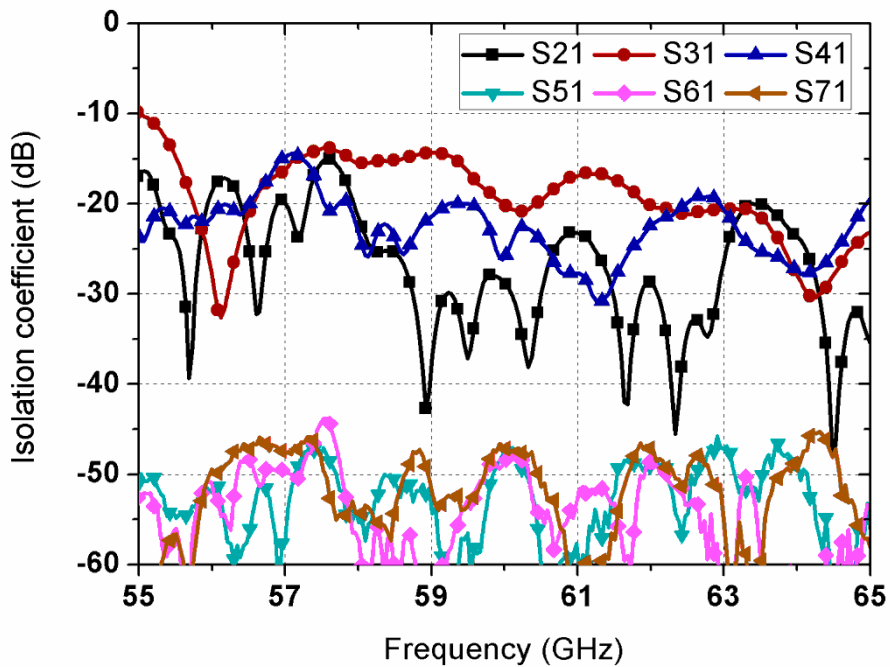


Figure 4-19 Isolation coefficients of the fabricated dual linear-polarization substrate integrated multibeam array antenna excited by port 1.

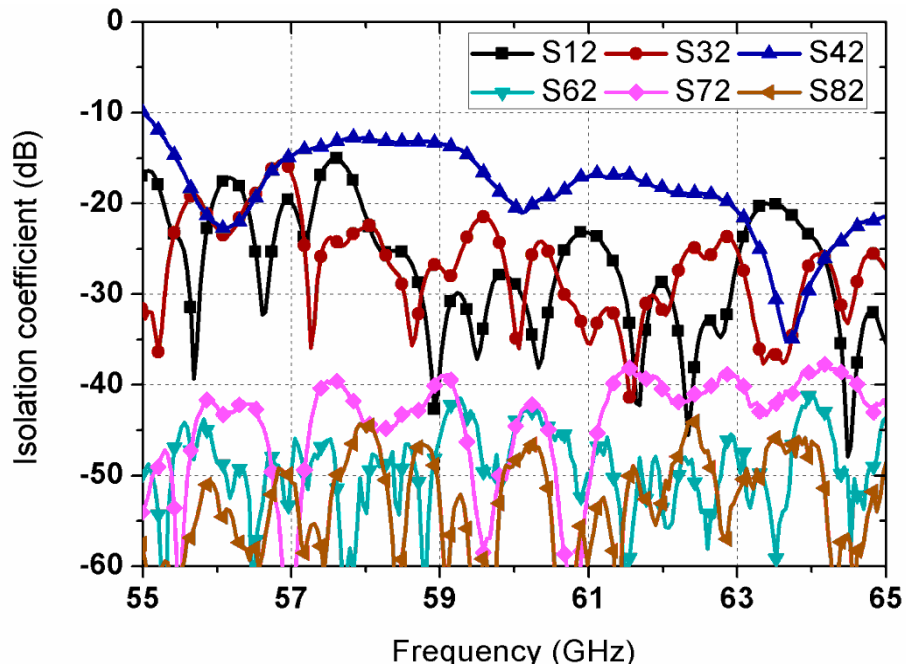


Figure 4-20 Isolation coefficients of the fabricated dual linear-polarization substrate integrated multibeam array antenna excited by port 2.

The radiation patterns of the fabricated antenna are measured by a far-field radiation measurement setup as illustrated in Fig. 4-21. It is able to generate four beams with -45° LP and different beam directions excited at ports 1~4, while four beams with 45° LP and different beam directions excited at ports 5~8. As shown in Figs. 4-22, 4-23, the measured radiation patterns of the array in yoz-plane are in agreement with the simulated results. The measured gains at beam direction are 12.4 dBi, 13.4 dBi, and 13.5 dBi at 58 GHz, 60 GHz and 62 GHz excited at port 1, while 14.9 dBi, 15.3 dBi, and 15.7 dBi at 58 GHz, 60 GHz and 62 GHz excited at port 2.

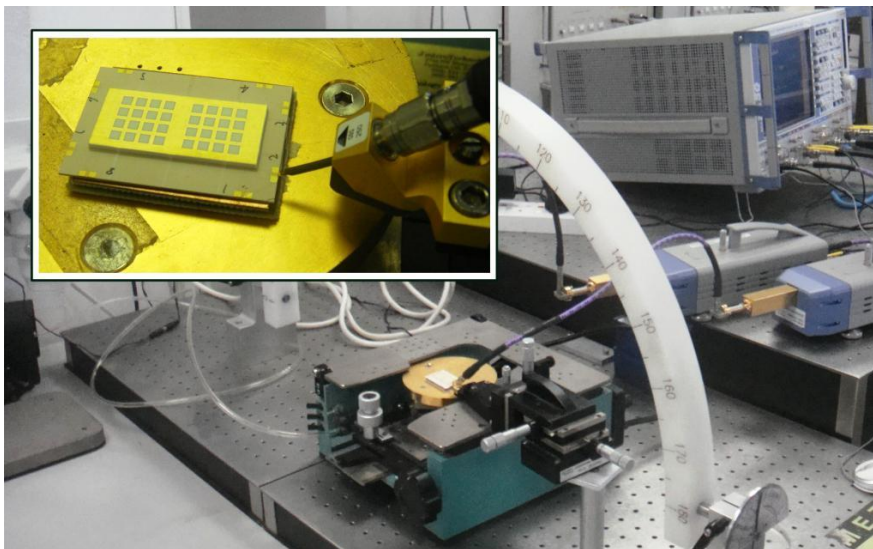


Figure 4-21 Far field measurement setup

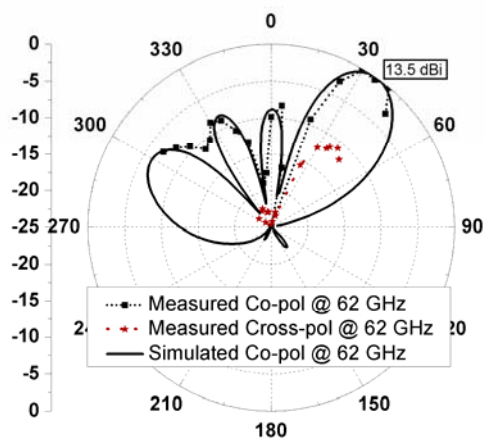
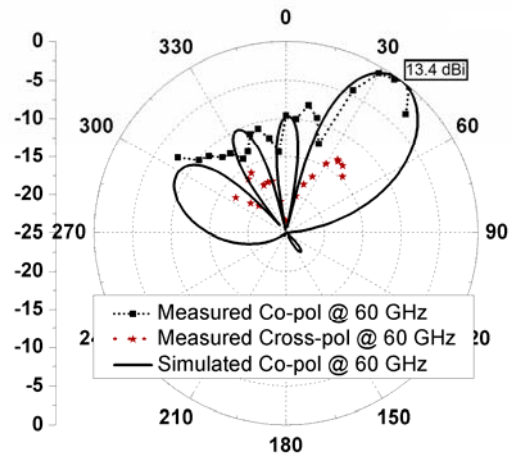
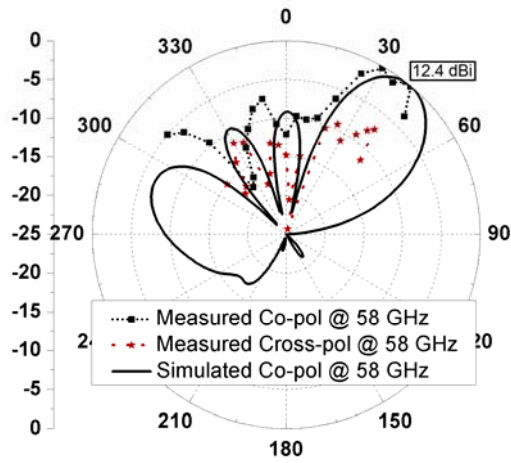


Figure 4-22 Simulated and measured radiation patterns of the fabricated dual linear-polarization multibeam array antenna at different frequency excited at port 1.

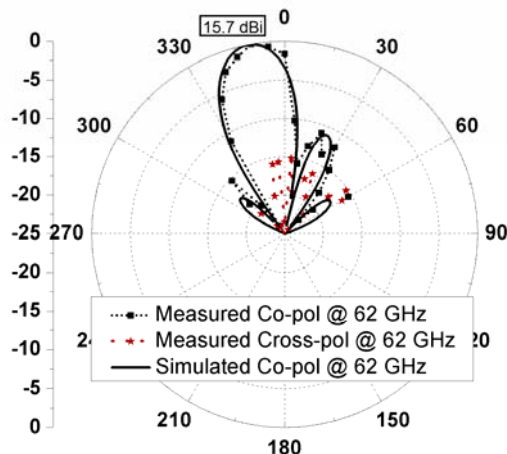
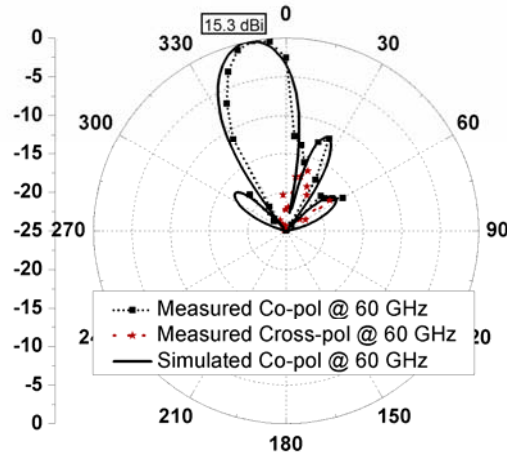
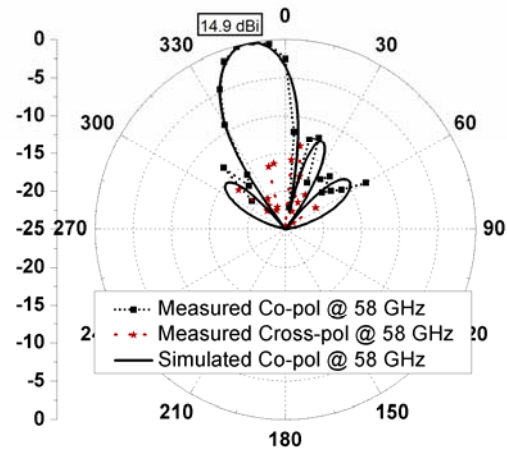


Figure 4-23 Simulated and measured radiation patterns of the fabricated dual linear-polarization multibeam array antenna at different frequency excited at port 2.

4.4 Dual Circularly Polarized Substrate Integrated Multibeam Antenna Array

4.4.1 Dual Circularly Polarized Antenna Array

Four linear arrays can be grouped as a 4×4 CP array antenna as well, in a different arrangement. The CP antenna array can be constructed by two 1×4 45° and two 1×4 -45° LP arrays arranged alternately. Fig. 4-24 shows the yoz-plane patterns with different phase shift between neighboring elements in simulation. As shown, the CP array antenna can generate LHCP and RHCP beams pointing at different directions simultaneously. The good reflection characteristic can be found as well. Therefore, it can be employed in the design of a dual circular-polarization multibeam array antenna.

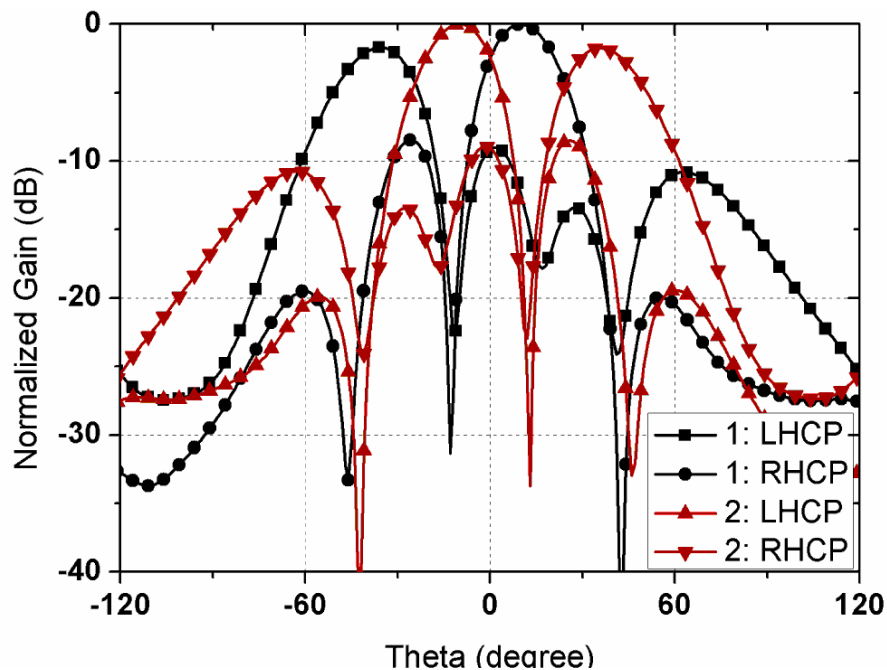


Figure 4-24 Simulated yoz-plane patterns of the proposed 4×4 CP array antenna (The phase for ports 1~4: case 1: 0° , 45° , 270° , and 315° ; case 2: 0° , -45° , 90° , and 45°)

Now, the dual CP operation mechanism will be investigated in details. The model consists of four elements, which are equally spaced in terms of distance d , set up along a straight line. The first and third element have the same polarizations (45° in this paper), while the second and the fourth elements

have the orthogonal polarizations (-45° in this paper). Its array factor can be written as:

$$\begin{aligned}\vec{F}(\theta) = & I_1 \hat{\alpha} + I_2 \hat{\beta} e^{j(\frac{2\pi d}{\lambda} \sin \theta - \varphi_1)} \\ & + I_3 \hat{\alpha} e^{j(\frac{4\pi d}{\lambda} \sin \theta - \varphi_2)} + I_4 \hat{\beta} e^{j(\frac{6\pi d}{\lambda} \sin \theta - \varphi_3)}\end{aligned}\quad (4-2)$$

If $I_1=I_2=I_3=I_4=1$, and $\varphi_1=-\pi/4$, $\varphi_2=\pi/2$, $\varphi_3=\pi/4$ (case 2 in Fig. 4-24),

$$\begin{aligned}\vec{F}(\theta) = & \hat{\alpha} [1 + e^{j(\frac{4\pi d}{\lambda} \sin \theta - \frac{\pi}{2})}] + \hat{\beta} [e^{j(\frac{2\pi d}{\lambda} \sin \theta + \frac{\pi}{4})} + e^{j(\frac{6\pi d}{\lambda} \sin \theta - \frac{\pi}{4})}] \\ = & [1 + e^{j(\frac{4\pi d}{\lambda} \sin \theta - \frac{\pi}{2})}] [\hat{\alpha} + e^{j(\frac{2\pi d}{\lambda} \sin \theta + \frac{\pi}{4})} \hat{\beta}]\end{aligned}\quad (4-3)$$

The beam direction, θ , of this array can be calculated by

$$\frac{4\pi d}{\lambda} \sin \theta - \frac{\pi}{2} = 0 \text{ or } -2\pi$$

In this work, $d=0.58\lambda$. Thus, $\theta=12^\circ$ or -40° . At the beam pointing of 12° , (4-3) becomes:

$$\vec{F}(\theta) = 2[\hat{\alpha} + j\hat{\beta}]$$

It is an LHCP beam. At the beam pointing of -40° , (4-3) becomes:

$$\vec{F}(\theta) = 2[\hat{\alpha} - j\hat{\beta}]$$

It is an RHCP beam. That means this scheme can support two orthogonal CP beams at the same time. They have different beam directions. The theoretical analysis is identical with the simulated results as shown in Fig. 4-24.

In order to feed a 4×4 CP antenna array and also have the switched-beam capacity, the 45° phase shifter within the folded Butler matrix as illustrated in Fig. 4-6 is replaced by a -45° phase shifter. In this situation, the proposed multibeam antenna can generate four beams with different pointing directions and polarizations as described in section 4.3. That means each port supports two operation modes, which have different polarizations and beam directions. When the polarization state is selected, the beam pointing direction for each port is determined.

4.4.2 Measurement and Analysis

The fabricated prototype is shown in Fig. 4-25, which also has 21-layer stacked ceramic tapes and is excited by CPWs. The total circuit area is $16.5 \times 14.6 \text{ mm}^2$ excluding the additional feeding structures. This size is approximately equal to that of a 4×4 array antenna. Fig. 4-26 presents the measured and simulated radiation patterns of the array in yoz-plane excited at port 3. The axial ratio at the beam direction of 60 GHz is 2.3 dB and 2.62 dB for LHCP and RHCP beams, respectively. The similar performance can be found with an excitation of port 1, but the polarization purity will be deteriorated when excited at ports 2 and 4. The main beam pointing direction and the beam direction with the best axial ratio are offset.

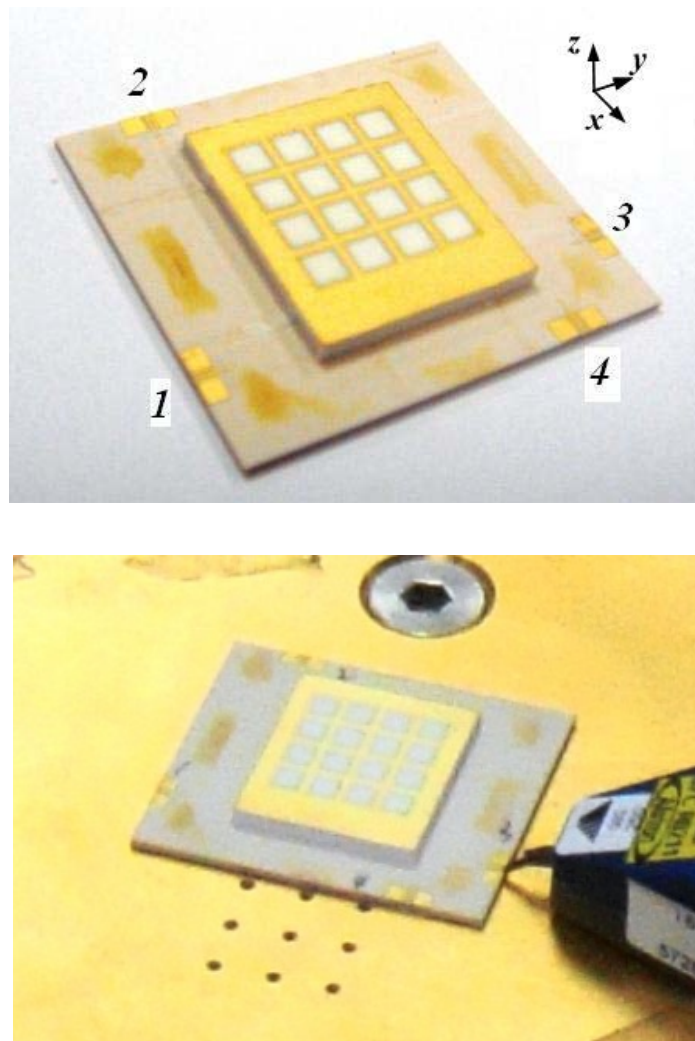
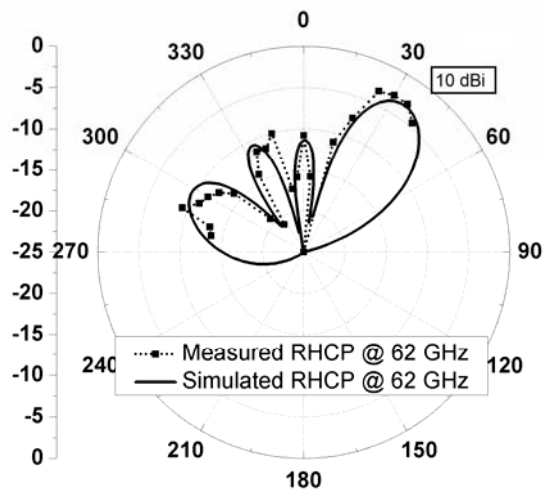
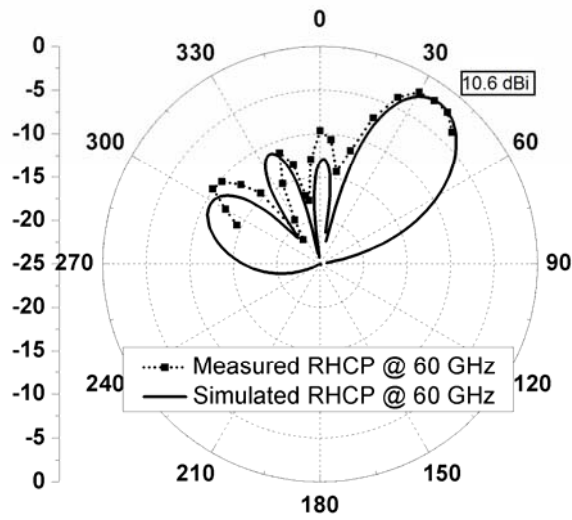
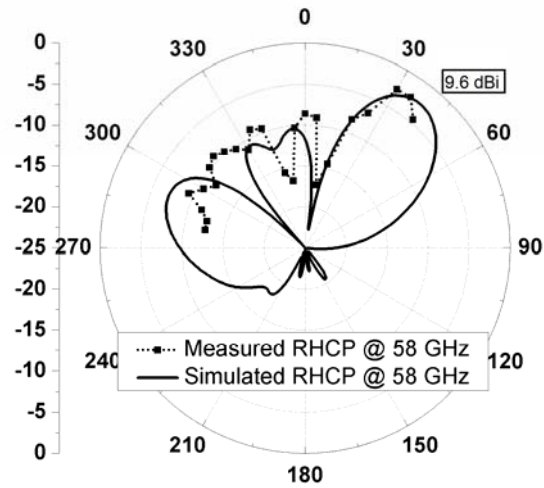


Figure 4-25 Photograph of the fabricated dual circular-polarization substrate integrated multibeam array antenna



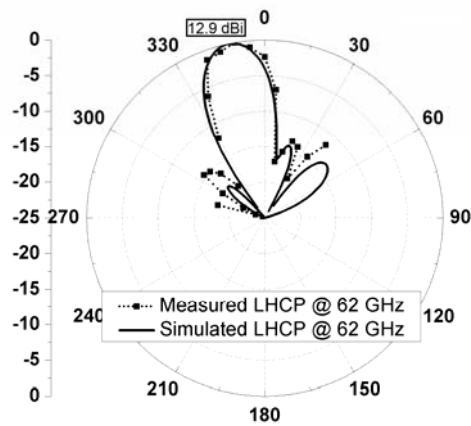
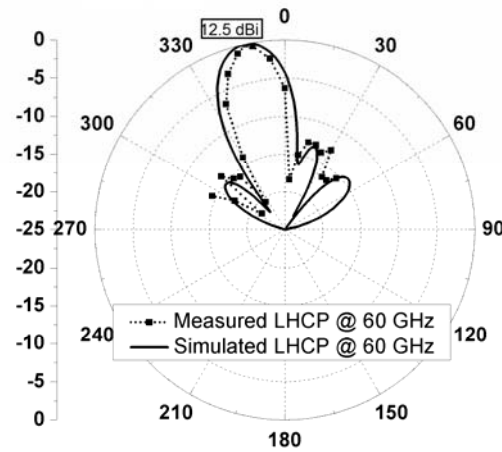
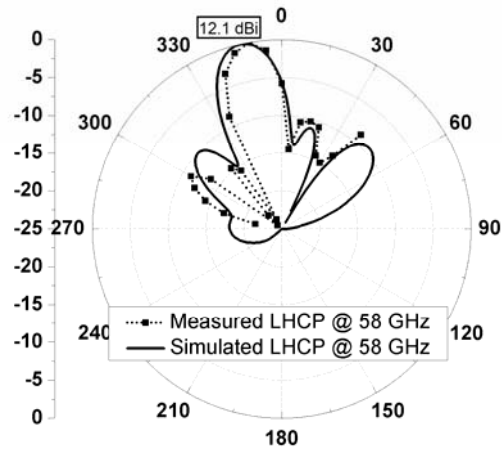


Figure 4-26 Simulated and measured radiation patterns of the fabricated dual circular-polarization multibeam array antenna at different frequencies excited at port3.

Table 4-1 lists comparative results among different SIW multibeam structures, including the operation frequency (f_0), size, port forming, gain at the center frequency and bandwidth (BW).

Table 4-1 Comparison with Different SIW Multibeam Antennas

	f_0 (GHz)	Size (λ_0)	Port forming	Gain (dBi)	BW
[105]	25.6	22×3.1	Coaxial line	23.1	3.7%
[106]	16	17.6×5	Microstrip line	22.7	3.8%
[109]	77	8.1×7.3	Waveguide	12.2	11%
[112]*	24	8.8×2.1	Microstrip line in different layers	12.9	-
Our work**	60	5.6×4	CPW	15.3	7%

* Slot array version

** A single LP multibeam antenna including the CPW-SIW transition

4.5 Summary

Several miniaturized substrate integrated multibeam array antennas with multiple-polarization capacity are developed in this paper. The folded Butler matrix and the SIW radiators are integrated as a whole by employing the LTCC fabrication process. The $\pm 45^\circ$ LP beam scanning and LHCP/RHCP beam scanning can be achieved by two dual-polarization multibeam antennas respectively, which are designed to operate at 60 GHz. Experiment results agree with the simulated performances. These designs represent excellent candidates in the development of millimeter-wave miniaturized multibeam systems.

Chapter 5: Conclusions and Future Works

5.1 Conclusions

The primary objective of this study is to design and analyze novel antennas-on-chip and antennas-in-package suitable for mm-Wave radio frequency wireless communications. By combining the AMC structure, employing modified soft-surface structure, and by folding 3-D Butler Matrix feeding network, a series of high-performance chip-level antenna and package-level antenna arrays, which can be further integrated into 60-GHz wireless systems, have been realized, analyzed, fabricated and measured.

For most current antennas-on-chip, CMOS fabrication process has encountered a critical problem of poor radiation because of the lossy silicon substrate. Typical antennas-on-chip have only 10% efficiency and gain of lower than -10 dBi, and hence cannot be used for practical commercial communications. In chapter 2, we propose one CP antenna-on-chip obtaining a gain improvement of 1~2 dBi by combining a modified AMC plane. This AMC plane makes the lossy silicon substrate equivalently act as a magnetic conductor and thus produces in-phase reflections with the incident wave at 60 GHz. This chip-level antenna can be used in the chip-to-chip wireless communications to replace the metal interconnects between chips, and the low-cost consumer handheld devices for near distance communications with high data rate transmission.

Meanwhile, for antennas-in-package, the surface wave introduces significant loss due to the higher permittivity of LTCC substrate at mm-Wave bands. In chapter 3, we demonstrated a modified soft-surface structure to solve this surface wave loss problem and improve the package-level antenna performance. The soft-surface structure consisting of vias and metal strips around the radiating edges of the patch elements is used to suppress the surface waves. Two such 4×4 in-package CP antenna array designs illustrated in this thesis have achieved much better 3-dB gain bandwidth.

In chapter 4, two miniaturized substrate integrated multibeam array antennas with multiple-polarization capacity are developed. The folded Butler matrix and the SIW radiators are integrated as a whole by employing the LTCC fabrication process. The $\pm 45^\circ$ LP beam scanning and LHCP/RHCP beam scanning can be achieved by two dual-polarization multibeam antennas respectively, which are designed to operate at 60 GHz. Experiment results agree with the simulated performances. These designs represent excellent candidates in the development of millimeter-wave miniaturized multibeam systems.

5.2 Recommendations for Future Work

In view of currently obtained research outcome and the state-of-art of mm-Wave antennas, there is still plenty of room for future extensions. The following items represent some possible future research directions:

- (1) It is possible to further analyze the periodic structures. The equivalent circuit of each specific structure could be simulated and investigated since finding corresponding physical realization of inductance and capacitance will benefit in designing better periodic structures.
- (2) New packaging techniques should be explored to further enhance the gain of antennas-on-chip in silicon based process for practical applications in 60-GHz wireless communication systems, such as high resistivity silicon substrate namely TSV. This kind of processing techniques can significantly improve the efficiency of the chip-level antennas.
- (3) Advanced fabrication techniques are also in great demand to decrease in-package antenna sensitivity to the fabrication tolerance. It has been observed that the width of the transmission line is an important factor leading to impedance matching performance. Moreover, CP antennas are usually quite sensitive to the fabrication precision in CP property.

A more robust fabrication procedure can increase the consistency of the package-level antennas. This procedure is also very critical to the in-package mass production.

- (4) New compact package-level antenna array which can provide higher gain and wider impedance matching bandwidth should be studied to improve the performance of the whole integrated system. Antennas with parasitic structure and stacked antennas may be promising choices to represent better performances for future mm-Wave wireless systems.
- (5) To achieve more practical wireless systems, it is desirable to integrate antennas with active circuits, so that the mismatching will be reduced to minimum. For example, a low noise amplifier or a filter can be combined into the antenna-in-package design. Wire bonding or flip chip methods are available for the connections.

BIBLIOGRAPHY

- [1] D. T. Emerson, "The work of Jagadis Chandra Bose: 100 years of mm-wave research," *IEEE Trans. Microw. Theory Tech.*, vol. 45, no.12, pp. 2267–2273, Dec. 1997.
- [2] J. H. Van Vleck, "The absorption of microwaves by oxygen," *Phys. Rev.*, vol. 71.7, pp. 413–424, 1947.
- [3] A.R. Tharek and J. P. McGeeham, "Outdoor propagation measurements in the millimeter wave band at 60 GHz," *Proc. Military Microwaves*, vol. 88, pp. 43–48, Jul. 1988.
- [4] S. W.Wales and D. C. Rickard, "Wideband propagation measurements of short range millimetric channels," *Electron. Commun. Eng. J.*, vol. 5, no. 4, pp. 249–254, Aug. 1993.
- [5] Regulations for Enforcement of the Radio Law 6-4-2 Specified Low Power Radio Station (11) 59-66 Band. The Ministry of Public Management, Home Affairs, Posts and Telecommunications of Japan, 2000.
- [6] Code of Federal Regulation, Title 47 Telecommunication, Chapter 1, Part 15.255. U.S. Federal Communication Commission (FCC), 2004.
- [7] Radio Standard Specification-210, Issue 6, Low-Power Licensed-Exempt Radio Communication Devices (All Frequency Bands): Category 1 Equipment. Industry Canada Spectrum Management and Telecommunications (IC-SMT), 2005.

- [8] Radio Communications (Low Interference Potential Devices) Class License Variation 2005 (No. 1), The Australia Communications and Media Authority (ACMA), 2005.
- [9] Electromagnetic Compatibility and Radio Spectrum Matters (ERM); System Reference document; Technical Characteristics of Multiple Gigabit Wireless System in the 60 GHz Range. ETSI DTR/ERM-RM-049, 2006.
- [10] A. Sadri, "802.15.3c usage model document," IEEE 802.15-06-0055-14-003c, May 2006.
- [11] S. K. Yong and C. C. Chong, "An overview of multigigabit wireless through millimeter wave technology: potentials and technical challenges," *EURASIP J. Wireless Commun. Networking*, 2007, Article ID: 78907.
- [12] J. G. Kim, H. S. Lee, H. Lee, J. B. Yoon, and S. Hong, "60-GHz CPW-fed post-supported patch antenna using micromachining technology," *IEEE Microw. Wireless Compon. Lett.*, vol. 15, no. 10, pp. 635–637, Oct. 2005.
- [13] H. Uchimura, N. Shino, and K. Miyazato, "Novel circular polarized antenna array substrates for 60 GHz-band," in *IEEE MTT-S Int Microwave Symp. Dig.*, Long Beach, CA, Jun. 12-17, 2005, pp. 1875–1878.
- [14] I. I. Kim, S. Pinel, J. Laskar, and J. G. Yook, "Circularly & linearly polarized fan beam patch antenna arrays on liquid crystal polymer substrate for V-band applications," in *Asia-Pacific Microwave Conf. Proc.*, Suzhou, Jiangsu, China, Dec. 4-7, 2005, vol. 4.
- [15] C. Karnfelt, P. Hallbjorner, H. Zirath, and A. Alping, "High gain active microstrip antenna for 60-GHz WLAN/WPAN applications," *IEEE Trans. Microw. Theory Tech.*, vol. 54, no. 6, pp. 2593–2603, Jun. 2006.
- [16] Online resource, http://www.ihe.kit.edu/diplomarbeiten_2802.php

- [17] B. Razavi, "CMOS transceiver for the 60-GHz band," in *Proc. IEEE RFIC*, San Francisco, CA, Jun. 11-13, 2006, p. 4.
- [18] Mitomo, T., Fujimoto, R., Ono, N., Tachibana, R., Hoshino, H., Yoshihara, Y., Tsutsumi, Y., Seto, I., "A 60-GHz CMOS receiver with frequency synthesizer," in *IEEE Symp. VLSI Dig.*, Kyoto, Japan, Jun. 14-16, 2007, pp. 172–173.
- [19] A. Babakhani, X. Guan, A. Komijani, A. Natarajan, and A. Hajimiri, "A 77-GHz phased-array transceiver with on-chip antennas in silicon: receiver and antennas," *IEEE J. Solid-State Circuits*, vol. 41, no. 12, pp. 2795–2806, Dec. 2006.
- [20] Y. P. Zhang, L. H. Guo, and M. Sun, "On-chip antennas for 60-GHz radios in silicon technology," *IEEE Trans. Electron Devices*, vol. 52, no. 7, pp. 1664–1668, Jul. 2005.
- [21] Chan, K.T., Chin, A., Lin, Y.D., Chang, C.Y., Zhu, C.X., Li, M.F., Kwong, D.L., McAlister, S., Duh, D.S., Lin, W.J., "Integrated antennas on Si with over 100 GHz performance, fabricated using an optimized proton implantation process," *IEEE Microw. Wireless Compon. Lett.*, vol. 13, no. 11, pp. 487–489, Nov. 2003.
- [22] H. R. Chuang, S. W. Kuo, C. C. Lin, and L. C. Kuo, "A 60-GHz millimeter-wave CMOS RFIC-on chip dipole antenna," *Microw. J.*, vol. 50, no. 1, p. 144, Jan. 2007.
- [23] C. S. Wang, J. W. Huang, S. H. Wen, S. H. Yeh, and C. K. Wang, "A CMOS RF front-end with on-chip antenna for V-band broadband wireless communications," in *Proc. ESSCIRC*, Munich, Germany, Sep. 10-14, 2007, pp. 143–146.
- [24] M. A. T. Sanduleanu, "60 GHz integrated circuits and wireless systems," presented at the ESSCIRC, Munich, Germany, Sep. 18-22, 2006.
- [25] H. S. Pisheh, Y. Komijany, M. Shahabadi, S. Mohajerzadeh, and M. Araghchini, "Design, simulation, and fabrication of a novel multi-band

- miniaturized antenna for wireless communication applications,” in *Proc. 30th Int. Conf. Infrared and Millimeter Waves*, Williamsburg, VA, Sep. 19-23, 2005, pp. 551–552.
- [26] O, K.K., Kihong Kim, Floyd, B.A., Mehta, J.L., Hyun Yoon, Chih-Ming Hung, Bravo, D., Dickson, T.O., Xiaoling Guo, Ran Li, Trichy, N., Caserta, J., Bomstad, W.R., II, Branch, J., Dong-Jun Yang, Bohorquez, J., Eunyoung Seok, Li Gao, Sugavanam, A., Lin, J.-J., Jie Chen, Brewer, J.E., “On-chip antennas in silicon ICs and their applications,” *IEEE Trans. Electron Devices*, vol. 52, no. 7, pp. 1312–1323, Jul. 2005.
- [27] M. R. N. Ahmadi, S. N. Safieddin, and L. Zhu, “On-chip antennas for 24, 60, and 77 GHz single package transceivers on low resistivity silicon substrate,” in *Proc. IEEE Antenna Propag. Symp.*, Honolulu, HI, Jun. 10-15, 2007, pp. 5059–5062.
- [28] U. Pfeiffer, J. Grzyp, D. Liu, B. Gaucher, T. Beukema, B. Floyd, and S. Reynolds, “A chip-scale packaging technology for 60-GHz wireless chipsets,” *IEEE Trans. Microw. Theory Tech.*, vol. 54, no. 8, pp. 3387–3397, Aug. 2006.
- [29] U. Pfeiffer, J. Grzyp, D. Liu, B. Gaucher, T. Beukema, B. Floyd, and S. Reynolds, “A 60-GHz radio chipset fully-integrated in a low-cost packaging technology,” in *Proc. 56th Electron. Compon. Technol. Conf.*, San Diego, CA, Jun. 2, 2006, pp. 1343–1346.
- [30] T. Zwick, D. Liu, and B. Gaucher, “Broadband planar superstrate antenna for integrated millimeter-wave transceivers,” *IEEE Trans. Antennas Propag.*, vol. 54, no. 10, pp. 270–2796, Oct. 2006.
- [31] D. Liu and B. Gaucher, “Design consideration for millimetre wave antennas within a chip package,” in *Proc. IEEE Int. Workshop Antenna Technol.*, Xiamen, China, Apr. 21-23, 2007, pp. 13–16.
- [32] Y. Tsutsumi *et al.*, “A triangular loop antenna mounted adjacent to a lossy Si substrate for millimeter-wave wireless PAN,” in *Proc. IEEE*

- Antennas Propag. Symp.*, Honolulu, HI, Jun. 10-15, 2007, pp. 1008–1011.
- [33] T. Seki, K. Nishikawa, I. Toyoda, and K. Tsunekawa, “Millimeterwave high-efficiency multilayer parasitic microstrip antenna array for system-on-package,” *NTT Tech. Rev.*, vol. 3, no. 9, pp. 33–40, Sep. 2005.
- [34] Y. C. Lee, W. Chang, and C. S. Park, “Monolithic LTCC SiP transmitter for 60 GHz wireless communication terminals,” in *IEEE MTT-S Int. Microwave Symp. Dig.*, Long Beach, CA, Jun. 12 17, 2005, pp. 1015–1018.
- [35] L. Desclos, “V-band double slot antenna integration on LTCC substrate using thick film technology,” *Microw. Opt. Technol. Lett.*, vol. 28, no. 5, pp. 354–357, Mar. 2001.
- [36] Y. P. Zhang, M. Sun, K. M. Chua, L. L. Wai, D. Liu, and B. Gaucher, “Antenna-in-package in LTCC for 60-GHz radio,” in *Proc. IEEE Int. Workshop Antenna Technol.*, Cambridge, U.K., Mar. 21-23, 2007, pp. 279–282.
- [37] Hoivic Hoivik, N., Liu, D., Jahnes, C.V., Cotte, J.M., Tsang, C., Patel, C., Pfeiffer, U., Grzyb, J., Knickerbocker, J., “High-efficiency 60 GHz antenna fabricated using low-cost silicon micromachining techniques,” in *Proc. IEEE Antennas Propag. Symp.*, pp. 5043–5046, Honolulu, HI, Jun. 10-15, 2007.
- [38] F. Gutierrez *et al.*, “On-chip integrated antenna structures in CMOS for 60 GHz WPAN systems,” in *IEEE Journal on Selected Areas in Communications*, vol. 27, no. 8, pp. 1367–1379, Oct. 2009.
- [39] Hammad M. Cheema and Atif Shamim, “The last barrier,” in *IEEE Microwave Magazine*, Jan/Feb. 2013.
- [40] S.-S. Hsu, K.-C. Wei, C.-Y. Hsu, and H. Ru-Chuang, “A 60-GHz Millimeter-Wave CPW-Fed Yagi Antenna Fabricated by Using 0.18μ

- m CMOS Technology,” *IEEE Electron Device Lett.*, vol. 29, no. 6, pp. 625–627, June 2008.
- [41] C.-C. Lin, S.-S. Hsu, C.-Y. Hsu, and H.-R. Chuang, “A 60-GHz millimeter-wave CMOS RFIC-on-chip triangular monopole antenna for WPAN applications,” *IEEE Antennas and Propagation Society International Symposium, 2007*, pp. 2522–2525, June 2007.
- [42] F. Gutierrez, S. Agarwal, K. Parrish, and T. S. Rappaport, “On-chip integrated antenna structures in CMOS for 60 GHz WPAN systems,” *IEEE J. Select. Areas Commun.*, vol. 27, no. 8, pp. 1367–1378, Oct. 2009.
- [43] K. T. Chan, A. Chin, Y. P. Chen, Y. D. Lin, T. S. Duh, and W. J. Lin, “Integrated antennas on Si, proton-implanted Si and Si-on-quartz,” in *IEDM Tech. Digest*, Jan. 2001, pp. 903–906.
- [44] Online resource, http://www.ltcc-consulting.com/What_is_the_LTCC.
- [45] S.M. Hu, L. Wang, Y.Z. Xiong, T.G. Lim, B. Zhang, J.L. Shi, X.J. Yuan, “TSV technology for millimeter-wave and Terahertz design and applications”, *IEEE Transaction on Component, Packaging, and Manufacturing Technology*, vol. 1, no.2, pp. 260-267, Feb 2011.
- [46] S. Pan and F. Capolino, “Design of a CMOS on-chip slot antenna with extremely flat cavity at 140 GHz,” *IEEE Antennas Wireless Propagat. Lett.*, vol. 10, pp. 827–830, July 2011.
- [47] J. W. May, R. A. Alhalabi, and G. M. Rebeiz, “A 3 G-Bit/s w-band SiGe ASK receiver with a high-efficiency on-chip electromagnetically-coupled antenna,” in *Proc. IEEE Radio Frequency Integrated Circuits Symp.*, June 2010, pp. 87–90.
- [48] J. Xu, Z. N. Chen, X. Qing, and W. Hong, “Bandwidth enhancement for a 60 GHz substrate integrated waveguide fed cavity array antenna on LTCC,” *IEEE Trans. Antennas Propag.*, vol. 59, no. 3, pp. 826 – 832, Marc. 2011.

- [49] A. Lamminen, J. Säily, and A. Vimpari, “60-GHz patch antennas and arrays on LTCC with embedded-cavity substrates,” *IEEE Trans. Antennas Propag.*, vol. 56, no. 9, pp. 2865 – 2874, Sep. 2008.
- [50] T. Seki, N. Honma, K. Nishikawa, and K. Tsunekawa, “60-GHz multilayer parasitic microstrip array antenna on LTCC substrate for system-on-package,” *IEEE Microw. Wireless Compon. Lett.*, vol. 15, no. 5, pp. 339 – 341, May 2005.
- [51] A. E. I. Lamminen, A. R. Vimpari, and J. Säily, “UC-EBG on LTCC for 60-GHz frequency band antenna applications,” *IEEE Trans. Antennas Propag.*, vol. 57, no. 10, pp. 2904–2912, Oct. 2009.
- [52] S. B. Yeap, Z. N. Chen, and X. Qing, “Gain-enhanced 60-GHz LTCC antenna array with open air cavities,” *IEEE Trans. Antennas Propag.*, vol. 59, no. 9, pp. 3470–3473, Sep. 2011.
- [53] L. Wang, Y.X. Guo, and W.X. Sheng, “Wideband high-gain 60-GHz LTCC L-probe patch antenna array with a soft-surface,” *IEEE Trans. Antennas Propag.*, early access, 2013.
- [54] D. Sievenpiper, “High-impedance electromagnetic surfaces with a forbidden frequency band,” *IEEE Trans. Microw. Theory Tech.*, vol. 47, pp. 2059–2074, Nov. 1999.
- [55] D. Sievenpiper, H.-P. Hsu, J. Schaffner, G. Tangonan, R. Garcia, and S. Ontiveros, “Low-profile, four-sector diversity antenna on high-impedance ground plane,” *Elect. Lett.*, vol. 36, pp. 1343–1345, Aug. 2000.
- [56] D. Sievenpiper, J. Schaffner, R. Loo, G. Tangonan, S. Ontiveros, and R. Harold, “A tunable impedance surface performing as a reconfigurable beam steering reflector,” *IEEE Trans. Antennas Propag.*, vol. 50, no. 3, pp. 384–390, Mar. 2002.
- [57] D. Sievenpiper, J. Schaffner, J.-J. Lee, and S. Livingston, “A steerable leaky-wave antenna using a tunable impedance ground plane,” *IEEE Antennas Wireless Propag. Lett.*, vol. 1, pp. 179–182, 2002.

- [58] F.-R. Yang, K.-P. Ma, Y. Qian, and T. Itoh, "Aperture-coupled patch antenna on uc-pbg substrate," *IEEE Trans. Microw. Theory Tech.*, vol. 47, pp. 2123–2130, Nov. 1999.
- [59] R. Coccioli, F.-R. Yang, K.-P. Ma, and T. Itoh, "A novel tem waveguide using uniplanar compact photonic-bandgap (UC-PBG) structure," *IEEE Trans. Microw. Theory Tech.*, vol. 47, no. 11, pp. 2092–2098, Nov. 1999.
- [60] F.-R. Yang, Y. Qian, and T. Itoh, "Antenna and circuit applications of uc-pbg structures," in *Proc. Int. Symp. Dig. on Antennas and Propagation, ISAP2000*, vol. 2, Fukuoka, Japan, Aug. 21–25, 2000, pp. 775–778.
- [61] C. Caloz and T. Itoh, "A super-compact super-broadband tapered uniplanar pbg structure for microwave and milli-meter wave applications," in *Proc. IEEE MTT-S Int. Microwave Symp. Dig.*, vol. 2, Seattle, WA, Jun. 2–7, 2002, pp. 1369–1372.
- [62] E. D. Isaacs, P. M. Platzman, and J. T. Shen, "Resonant antennas," U.S. Patent 6 879 298, 2005
- [63] F. Qureshi, M. A. Antoniades, and G. V. Eleftheriades, "A compact and low-profile metamaterial ring antenna with vertical polarization," *IEEE Antennas Wireless Propag. Lett.*, vol. 4, pp. 333–336, 2005
- [64] H. Mosallaei and K. Sarabandi, "Magneto-dielectrics in electromagnetics: Concept and applications," *IEEE Trans. Antennas Propag.*, vol. 52, no. 6, pp. 1558–1567, Jun. 2004.
- [65] F. Bilotti, A. Alu, and L. Vegni, "Design of miniaturized metamaterial patch antennas with -negative loading," *IEEE Trans. Antennas Propag.*, vol. 56, no. 6, pp. 1640–1647, Jun. 2008.
- [66] R. W. Ziolkowski and A. Erentok, "Metamaterial-based efficient electrically small antennas," *IEEE Trans. Antennas Propag.*, vol. 54, no. 7, pp. 2113–2130, Jul. 2006.

- [67] A. Erentok and R. W. Ziolkowski, "An efficient metamaterial-inspired electrically-small antenna," *Microw. Opt. Technol. Lett.*, vol. 49, no. 6, pp. 1287–1290, Jun. 2007.
- [68] A. Erentok and R. W. Ziolkowski, "Metamaterial-inspired efficient electrically small antennas," *IEEE Trans. Antennas Propag.*, vol. 56, no. 3, pp. 691–707, Mar. 2008.
- [69] A. Erentok and R. W. Ziolkowski, "Two-dimensional efficient metamaterial-inspired electrically small antenna," *Microw. Opt. Technol. Lett.*, vol. 49, no. 7, pp. 1669–1673, 2007.
- [70] S. Zouhdi, A. Sihvola and A. P. Vinogradov, "Metamaterials and Plasmonics: Fundamentals, Modelling, Applications", *NATO Science for Peace and Security Series*, Springer, 2008.
- [71] F. Yang, Y. R. Samii, "Electromagnetic Band Gap Structures in Antenna Engineering", *Cambridge University Press*, 2009.
- [72] M.K. Taher and W. G. Whittow, "Novel planar AMC for low profile antenna applications," in *Loughborough Antenna & Propagation Conference*, UK, Nov. 16–17, 2009.
- [73] A. Foroozesh and L. Shafai, "Investigation Into the Application of Artificial Magnetic Conductors to Bandwidth Broadening, Gain Enhancement and Beam Shaping of Low Profile and Conventional Monopole Antennas," *IEEE Trans. Antennas Propag.*, vol. 59, no. 1, pp. 4–21, Jan 2011.
- [74] D. Nestic, A. Nestic and V. Brankovic, "Circular polarized printed antenna with broadband axial ratio", *IEEE Antennas and Propagation Society International Symposium*, 2003.
- [75] H. Uchimura, N. Shino, K. Miyazato, "Novel circular polarized antenna array substrates for 60GHz-band," *IEEE MTT-S Int. Microwave Symp. Dig.*, pp. 1875-1878, Long Beach, CA, USA, 12–17 Jun. 2005.

- [76] S. Pinel, II Kwon Kim, K. Yang and J. Laskar, “60 GHz linearly and circularly polarized antenna arrays on liquid crystal polymer substrate”, *Proceedings of the 3rd European Micro-wave Conference*, 2006.
- [77] R.G. Zhou, D.X. Liu, H. Xin, “Design of circularly polarized antenna for 60 GHz wireless communications,” *3rd European Conference on Antennas and Propagation (EuCAP 2009)*, 23–27 Mar. 2009, pp. 3787–3789.
- [78] R.L. Li, G. Dejean, J. Laskar and M.M. Tentzeris, “Investigation of circularly polarized loop antennas with a parasitic element for bandwidth enhancement,” *IEEE Trans. Antennas Propag.*, vol. 53, no. 12, pp. 3930-3939, Dec 2005.
- [79] P.-J. Guo, and H.-R. Chuang, “A 60-GHz Millimeter-wave CMOS RFIC-on-chip Meander-line Planar Inverted-F Antenna for WPAN Applications”, *Antennas and Propagation Society International Symposium*, pp.1-4, July.2008.
- [80] K. Kang, F.J. Lin, D.D. Pham, J. Brinkhoff, C.H. Heng, Y.X. Guo and X.J. Yuan, “A 60-GHz OOK Receiver with an on-chip antenna in 90nm CMOS”, *IEEE Journal of Solid-State Circuits*, Vol. 45, No. 9, pp. 1720-1731, Sep, 2010.
- [81] F. Gutierrez, S. Agarwal, K. Parrish, and T. S. Rappaport, “On-chip integrated antenna structures in CMOS for 60 GHz WPAN systems”. *IEEE J. Sel. Areas Communications*, vol. 27, no. 8, pp. 1367-1368, Oct 2009.
- [82] Y.P. Zhang and D.X. Liu, “Antenna-on-chip and antenna-in-package solutions to highly integrated millimeter-wave devices for wireless communications,” *IEEE Trans. Antenna Propagation*, vol. 57, no. 10, pp. 2830-2841, Oct. 2009.
- [83] B. Pan, Y. Li, G.E.Ponchak, J. Papapolymerou, M.M. Tentzeris, “A 60-GHz CPW-Fed High-Gain and broadband integrated horn Antenna,”

- IEEE Trans. Antennas Propagation.*, vol. 57, no. 4, pp.1050–1056, Apr. 2009.
- [84] R. Zhou, D. Liu, and H. Xin, “Design of circularly polarized antenna for 60 GHz wireless communications,” in *Proc. 3rd Eur. Conf. Antennas Propag.*, 2009, pp. 3787 – 3789.
- [85] S. Pinel, I. K. Kim, K. Yang, and J. Laskar, “60 GHz linearly and circularly polarized antenna arrays on liquid crystal polymer substrate,” in *Proc. 36th Eur. Microw. Conf.*, 2006, pp. 858 – 861.
- [86] A. R. Weily and Y. J. Guo, “Circularly polarized ellipse-loaded circular slot array for millimeter-wave WPAN applications,” *IEEE Trans. Antennas Propag.*, vol. 57, no. 10, pp. 3680 – 3684, Oct. 2009.
- [87] K.-F. Hung and Y.-C. Lin, “Novel broadband circularly polarized cavity-backed aperture antenna with traveling wave excitation,” *IEEE Trans. Antennas Propag.*, vol. 58, no. 1, pp. 35 – 42, Jan. 2010.
- [88] M. Shahabadi, D. Busuioc, A. Borji, and S. Safavi-Naeini, “Low-cost, high-efficiency quasi-planar array of waveguide-fed circularly polarized microstrip antennas,” *IEEE Trans. Antennas Propag.*, vol. 53, no. 6, pp. 2036 – 2043, Jun. 2005.
- [89] J. Huang, “A Ka-band circularly polarized high-gain microstrip array antenna,” *IEEE Trans. Antennas Propag.*, vol. 43, no. 1, pp. 113 – 116, Jan. 1995.
- [90] M. Sun, Y. Q. Zhang, Y. X. Guo, M. F. Karim, O. L. Chuen, and M. S. Leong, “Integration of circular polarized array and LNA in LTCC as a 60-GHz active receiving antenna,” *IEEE Trans. Antennas Propag.*, vol. 59, no. 8, pp. 3083–3089, Aug. 2011.

- [91] H.C. Sun and Y.X. Guo, “60-GHz circularly polarized U-slot patch antenna array on LTCC,” *IEEE Trans. Antennas Propag.*, vol. 56, no. 3, pp. 691–707, April. 2013.
- [92] Y. Li, Z.N. Chen, X.M. Qing, Z.Z. Zhang, J.F. Xu, Z.H. Feng., “Axial ratio bandwidth enhancement of 60 GHz substrate integrated waveguide-fed circularly polarized LTCC antenna array”, *IEEE Trans. Antennas Propag.*, vol. 60, no.10, pp. 4619-4627, Oct, 2012.
- [93] C.R. Liu, Y.X. Guo, X.Y. Bao, S.Q. Xiao, “60-GHz LTCC Integrated Circularly Polarized Helical Antenna Array”, *IEEE Trans. Antennas Propag.*, vol. 60, no.3, pp. 1329-1335, Mar 2012.
- [94] V.H. Rumsey, “Horn antennas with uniform power patterns around their axes”, *IEEE Trans. Antennas Propag.*, vol. AP-14, pp. 656-658, 1966.
- [95] R.E. Lawrie and L. Peters, “Modifications of horn antennas for low sidelobe levels”, *IEEE Trans. Antennas Propag.*, vol. AP-14, pp. 605-610, 1966.
- [96] R.L. Li, G. DeJean, M. Tentzeris, J. Papapolymerou, and J. Laskar, “Radiation-pattern improvement of patch antennas on a large-size substrate using a compact soft-surface structure and its realization on LTCC multilayer technology,” *IEEE Trans. Antennas Propag.*, vol. 53, pp. 200–208, Jan. 2005.
- [97] Z. Ying and P.-S. Kildal, “Improvements of dipole, helix, spiral, microstrip patch and aperture antennas with ground planes by using corrugated soft surfaces,” *IEE Proc. Microw. Antennas Propag.*, vol. 143, pp. 244–248, Jun. 1996.
- [98] T. Bertuch, “Comparative investigation of coupling reduction by EBG surfaces for quasi-static RCS measurement systems,” *IEEE Antennas Wireless Propag. Lett.*, vol. 5, pp. 231–234, 2006.

- [99] P.-S. Kildal and A. Kishk, "EM modeling of surfaces with STOP or GO characteristics. Artificial magnetic conductors and soft and hard surfaces," *Appl. Comput. Electromagn. Society J.*, vol. 18, no. 1, 2003.
- [100] S. Lee, S. Song, Y. Kim, J. Lee, C.-Y. Cheon, K.-S. Seo, and Y. Kwon, "A V-band beam-steering antenna on a thin-film substrate with a flip-chip interconnection", *IEEE Microw. Wireless Compon. Lett.*, vol. 18, no. 4, pp. 287–289, Apr. 2008.
- [101] C. H. Tseng, C. J. Chen, and T. H. Chu, "A low-cost 60-GHz switched-beam patch antenna array with Butler matrix network", *IEEE Antennas Wireless Propag. Lett.*, vol. 7, pp. 432–435, 2008.
- [102] W. Lee, J. Kim, C. S. Cho, and Y. J. Yoon, "Beamforming lens antenna on a high resistivity silicon wafer for 60 GHz WLAN", *IEEE Trans. Antennas Propag.*, vol. 58, no. 3, pp. 706–713, Mar. 2010.
- [103] W. Choi, K. Park, Y. Kim, K. Kim, and Y. Kwon, "A V-band switched beam-forming antenna module using absorptive switch integrated with 4×4 Butler matrix 0.13- μm CMOS", *IEEE Trans. Microw. Theory Tech.*, vol. 58, no. 12, pp. 4052–4059, Dec. 2010.
- [104] W. F. Moulder, W. Khalil, and J. L. Volakis, "60-GHz two-dimensionally scanning array employing wideband planar switched beam network", *IEEE Antennas Wireless Propag. Lett.*, vol. 9, pp. 818–821, 2010.
- [105] S. Yamamoto, J. Hirokawa, and M. Ando, "A beam switching slot array with a 4-way Butler matrix installed in a single layer post-wall waveguide", in *Proc. IEEE AP-S Int. Symp.*, June 2002, vol. 1, pp. 138-141.
- [106] P. Chen, W. Hong, Z. Q. Kuai, and H. M. Wang, "A multibeam antenna based on substrate integrated waveguide technology for MIMO wireless communications," *IEEE Trans. Antennas Propag.*, vol. 57, no. 6, pp. 1813-1821, Jun. 2009.

- [107] Y. J. Cheng, W. Hong, and K. Wu, "Millimeter-wave multibeam antenna based on eight-port hybrid," *IEEE Microw. Wireless Compon. Lett.*, vol. 19, no. 4, pp. 212-214, Apr. 2009.
- [108] F. F. He, K. Wu, W. Hong, L. Han, and X. P. Chen, "Low-cost 60-GHz smart antenna receiver subsystem based on substrate integrated waveguide technology," *IEEE Trans. Microw. Theory Tech.*, vol. 60, no. 4, pp. 1156-1164, Apr. 2012.
- [109] T. Djerafi, and K. Wu, "A low-cost wideband 77-GHz planar Butler matrix in SIW technology," *IEEE Trans. Antennas Propag.*, vol. 60, no. 10, pp. 4949-4954, Oct. 2012.
- [110] A. A. M. Ali, N. J. G. Fonseca, F. Coccetti, and H. Aubert, "Design and implementation of two-layer compact wideband Butler matrices in SIW technology for Ku-band applications," *IEEE Trans. Antennas Propag.*, vol. 59, no. 2, pp. 503-512, Feb. 2011.
- [111] Y. J. Cheng, C. A. Zhang, and Y. Fan, "Miniaturized multilayer folded substrate integrated waveguide butler matrix," *Prog. Electromagn. Res. C*, vol. 21, pp. 45-58, 2011.
- [112] T. Djerafi, and K. Wu, "Multilayered substrate integrated waveguide 4×4 Butler matrix," *Int. J. RF Microw. Comput.-Aid En.*, vol. 22, no. 3, pp. 336-344, May 2012.
- [113] Y. J. Cheng, W. Hong, and K. Wu, "Broadband self-compensating phase shifter combining delay line and equal-length unequal-width phaser," *IEEE Trans. Microw. Theory Tech.*, vol. 58, no. 1, pp. 203-210, Jan. 2010.